THE FIRST THREE YEARS OF *IBEX* OBSERVATIONS AND OUR EVOLVING HELIOSPHERE

D. J. McComas[1,2], M. A. Dayeh[1], F. Allegrini[1,2], M. Bzowski[3], R. DeMajistre[4], K. Fujiki[5], H. O. Funsten[6],
S. A. Fuselier[1], M. Gruntman[7], P. H. Janzen[8], M. A. Kubiak[3], H. Kucharek[9], G. Livadiotis[1], E. Möbius[9,10],
D. B. Reisenfeld[8], M. Reno[1,11], N. A. Schwadron[1,9], J. M. Sokół[3], AND M. Tokumaru[5]

[1] Southwest Research Institute, P.O. Drawer 28510, San Antonio, TX 78228, USA; dmccomas@swri.org
[2] Department of Physics and Astronomy, University of Texas at San Antonio, San Antonio, TX 78249, USA
[3] Space Research Centre of the Polish Academy of Sciences, Bartycka 18A, 00-716, Warsaw, Poland
[4] Applied Physics Laboratory, Johns Hopkins University, 11100 Johns Hopkins Road, Laurel, MD 20723, USA
[5] Solar-Terrestrial Environment Laboratory, Nagoya University, Nagoya 464-8601, Japan
[6] Los Alamos National Laboratory, Intelligence and Space Research Division, P.O. Box 1663, Los Alamos, NM 87545, USA
[7] Department of Astronautical Engineering, Viterbi School of Engineering, University of Southern California, Los Angeles, CA 90089-1192, USA
[8] Department of Physics and Astronomy, University of Montana, 32 Campus Drive, Missoula, MT, USA
[9] Space Science Center, University of New Hampshire, Morse Hall Rm 407, Durham, NH 03824, USA
[10] Los Alamos National Laboratory, Los Alamos, NM, USA
[11] Austin Mission Consulting, 4301 W William Cannon, Austin, TX 78749, USA

ABSTRACT

This study provides, for the first time, complete and validated observations from the first three years (2009–2011) of the *Interstellar Boundary Explorer* (*IBEX*) mission. Energetic neutral atom (ENA) fluxes are corrected for both the time-variable cosmic ray background and for orbit-by-orbit variations in their probability of surviving en route from the outer heliosphere in to 1 AU where *IBEX* observes them. In addition to showing all six six-month maps, we introduce new annual ram and anti-ram maps, which can be produced without the need for algorithm-dependent Compton–Getting corrections. Together, the ENA maps, data, and supporting documentation presented here support the full release of these data to the broader scientific community and provide the citable reference for them. In addition, we show that heliospheric ENA emissions have been decreasing over the epoch from 2009 to 2011 with the *IBEX* Ribbon decreasing by the largest fraction and only the heliotail (which is offset from the down wind direction by the interstellar magnetic field) showing essentially no reduction and actually some increase. Finally, we show how the much more complete observations provided here strongly indicate a quite direct and latitude-dependent solar wind source of the Ribbon.

Key words: ISM: general – ISM: magnetic fields – plasmas – solar wind – Sun: heliosphere – stars: atmospheres

Online-only material: color figures

1. INTRODUCTION

IBEX—the *Interstellar Boundary Explorer* (see McComas et al. 2009a and other papers in the *IBEX* Special Issue of *Space Science Reviews*)—has been returning energetic neutral atom (ENA) observations of the heliosphere's interstellar interaction since 2008 December 25. *IBEX* provided the first global observations of this interaction, based on energy-resolved, all-sky ENA images. These observations include ENAs over the energy range from ∼0.1 to 6 keV and showed both globally distributed fluxes and a completely unexpected "Ribbon" of significantly enhanced ENA emissions. These and other initial discoveries from *IBEX*, including the direct observation of the flow distribution of interstellar H, He, and O neutral atoms at 1 AU, were published in a special issue of *Science* (McComas et al. 2009b; Fuselier et al. 2009a; Funsten et al. 2009b; Schwadron et al. 2009; Möbius et al. 2009).

The original *Science* papers showed the existence of a narrow Ribbon of enhanced ENA fluxes up to ∼2–3 times larger than the surrounding globally distributed fluxes (McComas et al. 2009b). The Ribbon is ∼20° wide over a broad energy range from 0.7 to 2.7 keV (Fuselier et al. 2009a) and contains fine structure that is at most a few degrees across (McComas et al. 2009b). The Ribbon also contains a bright "knot" around 60° N ecliptic latitude, with a different spectral shape than the rest of the Ribbon, being enhanced at higher energies (McComas

et al. 2009b); this spectral shape is similar to other near-pole energy spectra from the surrounding globally distributed flux (Funsten et al. 2009b). Perhaps the most remarkable aspect of the *IBEX* Ribbon is that it appears to be ordered by the most likely direction of the draped interstellar magnetic field outside the heliopause such that the field is perpendicular to *IBEX*'s essentially radially outward viewing (McComas et al. 2009b; Schwadron et al. 2009).

Over the past couple of years, since the initial *Science* papers, there have been dozens of papers written on various aspects of the *IBEX* observations as well as numerous theoretical and model-based studies, many of which have tried to address the source of the Ribbon. For example, one study that addresses many of the global aspects of the *IBEX* ENA observations separated globally distributed ENA fluxes from the Ribbon (Schwadron et al. 2011) and found both a different spectral signature for the Ribbon and a clearly identifiable heliotail in the globally distributed flux in a direction roughly halfway between the downwind flow and magnetic field directions. Such an offset heliotail reinforces the central importance that the external magnetic field plays in the global heliospheric interaction (McComas et al. 2009b). A very recent review by McComas et al. (2011b) summarizes the numerous *IBEX* studies, so we will not repeat a broad summary here.

One of the most critical questions related to the source of the Ribbon and other aspects of the interstellar interaction is that

of time variations in the ENA fluxes. McComas et al. (2010) first examined this issue; these authors compared the first two maps (the only data taken at that time) and looked for temporal changes over the six months between the two views of each portion of the sky. They found that the large-scale structure was generally stable between the two sets of maps, but that there were some small variations indicating that the heliosphere is evolving even over this short timescale. In particular, they found in the second map compared to the first: (1) slightly lower ENA fluxes overall, (2) significantly lower (~10%–15%) fluxes from the north and south poles, and (3) that the "knot" emissions in the northern region of the Ribbon diminished and appeared to spread out along the Ribbon.

Only two other studies so far have looked for time variations in the *IBEX* observations, and both focused on the polar ENA fluxes. Reisenfeld et al. (2012) used the fact that *IBEX* continuously observes the heliospheric poles to look for time variations in these regions on timescales even shorter than six months. This study found that both the north and south polar ENA flux had been steadily decreasing for the two-year period from 2008 December–2011 February. They further found that the decrease was energy-dependent, being largest at ~1 keV and smaller at both lower and higher energies. Both this paper and the prior McComas et al. (2010) study generally found that decreasing ENA fluxes were consistent with the steady decline in solar wind dynamic pressure associated with the most recent, prolonged, and deep solar minimum (McComas et al. 2008) as it takes several years for solar wind ions to propagate from the Sun to the inner heliosheath and once neutralized travel back as ENAs. This calculation produced termination shock (heliopause) distances of 110 (165) AU and 134 (216) AU at the south and north ecliptic poles, respectively. The other study (Allegrini et al. 2012) also examined polar ENAs and constructed spectra including the effect that for contemporaneous observations, slower ENAs must have left the source at an earlier time than faster ones. Assuming a time-invariant ENA survival rate, these authors applied time lag corrections to constructed source spectra (spectra of ENAs that left the source at roughly the same time). This analysis also showed statistically significant changes in the spectral shape of ENA emissions at the poles over time.

IBEX results, together with in situ observations from the *Voyager 1* and *2* spacecraft currently in the inner heliosheath, other supporting observations from several spacecraft, and a broad theory and modeling effort are producing a revolutionary new understanding of the outer heliosphere and its interactions with the local interstellar medium. In this study, we provide new ENA observations from *IBEX*, covering its second and third years of science operations, and extend the work of McComas et al. (2010) by quantifying the full-sky ENA emissions and their temporal variations over all three years of observations.

This release of six ENA maps spanning three years incorporates rigorous validation of the data selection and of the processing of this data into maps. Therefore, this also represents a re-release of the first year of observations in addition to years two and three as part of this study. We review the methodology for data selection. Appendix A, which focuses on the *IBEX-Hi* detector subsystem, examines the *IBEX-Hi* detection efficiency over three years as well as identification and removal of the time-variable cosmic ray background. Appendix B describes ENA transport from the outer heliosphere to their measurement by *IBEX* at 1 AU, specifically, we quantify the time-dependent survival probabilities of various energy ENAs in order to cal-
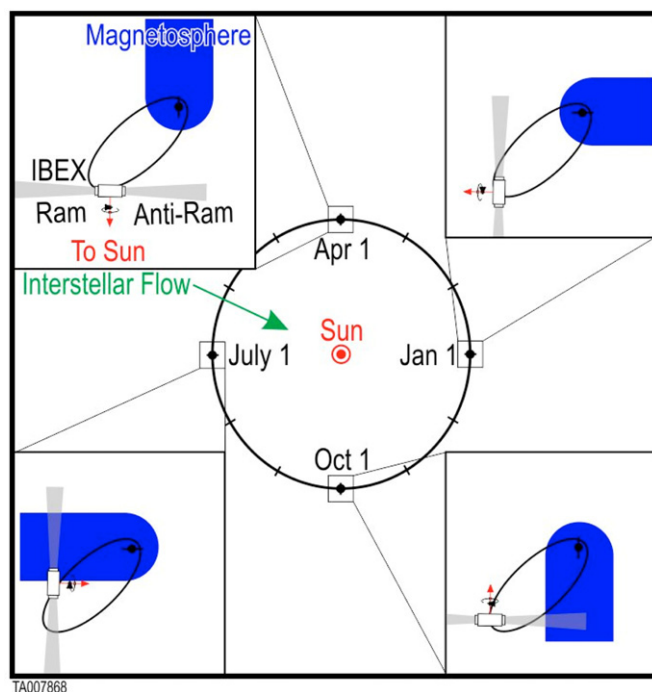

Figure 1. Schematic diagram of *IBEX* orbit with respect to the Sun and magnetosphere (blue) at the start of annual quarters. The *IBEX* spacecraft is repointed once or twice per orbit and views perpendicular to its Sun-pointing spin axis. The first and other odd-numbered maps are taken when *IBEX*'s apogee is on the sunward side of the Earth, which provides more unobstructed viewing of the heliosphere and lower backgrounds, while even-numbered maps have higher backgrounds and poorer counting statistics. Adapted from McComas et al. (2010).

(A color version of this figure is available in the online journal.)

culate the ENA fluxes in the outer heliosphere, much closer to their sources. Thus, going forward, this study should be used as the citable reference for the first three years of *IBEX* data and the various corrections to these data; data are available from the general *IBEX* Web site[12] in the data release section[13] as well as through the National Space Science Data Center.

2. THREE FULL YEARS OF *IBEX* OBSERVATIONS

IBEX is a Sun-pointed spinning spacecraft (~4 rpm) in a highly elliptical Earth orbit, with apogee out at ~50 R_E (McComas et al. 2009a). The *IBEX-Hi* (Funsten et al. 2009a) and *IBEX-Lo* (Fuselier et al. 2009b) single-pixel ENA sensors view perpendicular to the spin axis, so over each spin of the spacecraft, they image ENAs arriving from a fixed (great circle) band around the sky. For the first two and a half years of science operations (through Orbit 127), *IBEX*'s orbital period was ~7.5 days and the spin axis was repointed once each orbit (around perigee), leading to bands of sky viewing centered ~7°.5 apart. In 2011 June, over Orbits 128 and 129, *IBEX* was maneuvered into a previously unknown, long-term stable lunar synchronous orbit with apogee still ~50 R_E (McComas et al. 2011a). Since then, *IBEX*'s orbital period has been ~9.1 days (one-third of the lunar sidereal period of 27.3 days, which we refer to as *IBEX*'s "P/3" orbit).

Starting with Orbit 130, we have also changed operations to repoint the spacecraft both near perigee and apogee, producing complete bands (or orbit arcs) of ENA observations centered

---

[12] http://ibex.swri.edu/
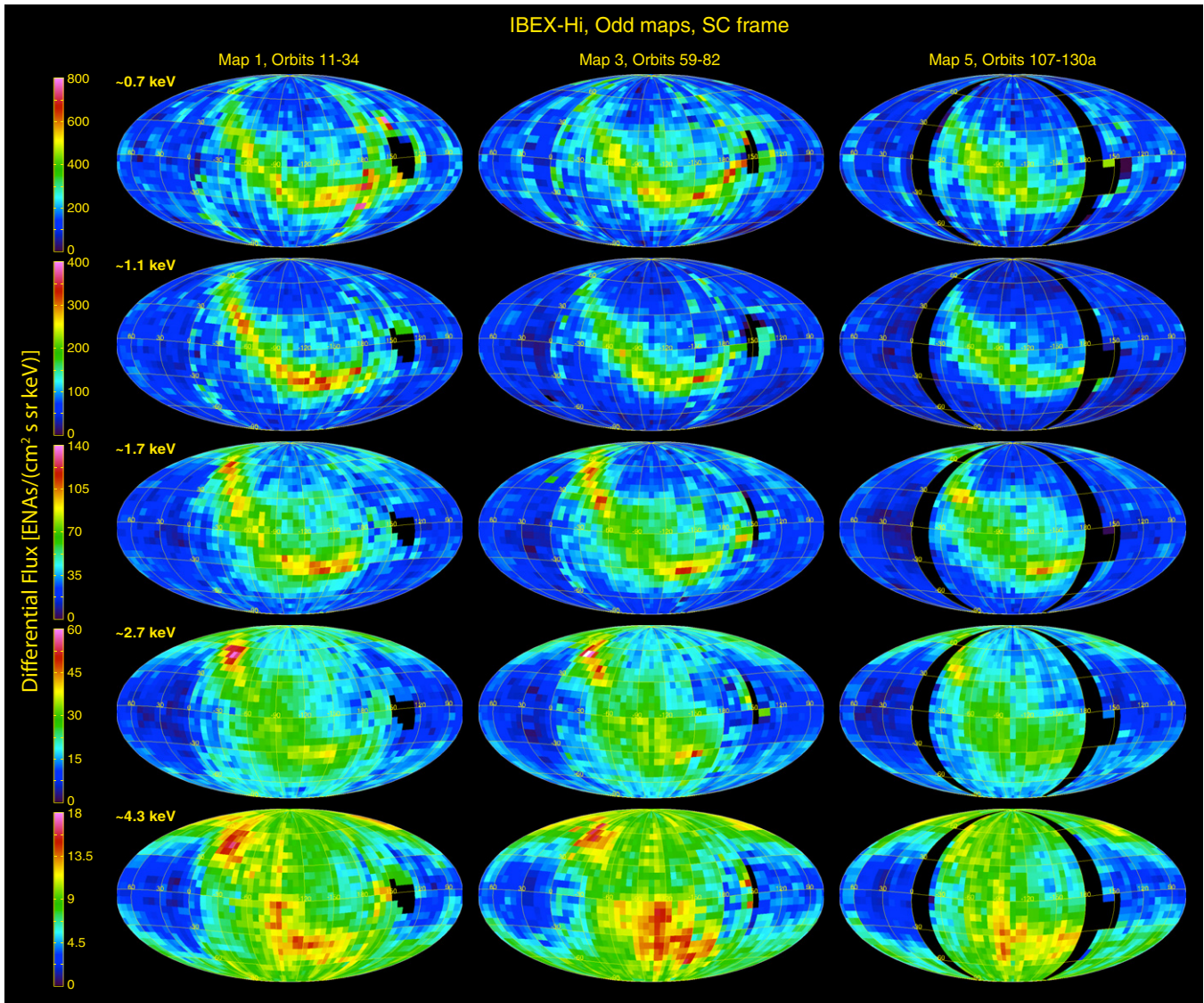[13] http://ibex.swri.edu/researchers/publicdata.shtml

Figure 2. Mollweide projections of ENA fluxes for Maps 1, 3, and 5 (columns 1, 2, and 3, respectively) for the five *IBEX-Hi* energy steps, which collectively cover energies from ∼0.5 to 6 keV FWHM.

(A color version of this figure is available in the online journal.)

∼4°.5 apart. The ascending (perigee to apogee) and descending (apogee to perigee) orbit arcs are denoted as arc "a" and arc "b", respectively. Repointing twice during each orbit provides a directional oversampling in ecliptic longitude since the intrinsic full angular resolution of the *IBEX* ENA instruments is ∼7° FWHM; this oversampling can be used for enhanced angular resolution or summed on the ground to increase counting statistics. Over the course of each six months, regular repointing of the spacecraft rotates the band of observations through 180° and *IBEX* captures a complete map of the sky in both *IBEX*'s original and its current P/3 lunar synchronous orbits.

Figure 1 shows the geometry of *IBEX*'s orbit over the year. Because the magnetosphere extends anti-sunward from the Earth, it rotates through *IBEX*'s inertially fixed orbit over the course of each year. During seasons when *IBEX*'s orbit is largely in and/or viewing through the magnetosphere and magnetosheath, opportunities for unobscured and low background heliospheric observations are vastly reduced, producing considerably poorer counting statistics. In order to fulfill minimum mission success as soon after launch as possible, the initial *IBEX* orbit was cho-

sen such that the first six-month sky map would be produced from data with *IBEX*'s apogee on the sunward side of Earth, maximizing the time *IBEX* was outside Earth's bow shock and in the solar wind. Thus, Map 1 and subsequent odd-numbered six-month maps have significantly lower backgrounds and better statistics for heliospheric observations than the even number maps.

Table 1 gives the relationship between orbit numbers (Orbit 11 was the first post-turn-on science orbit after sensor commissioning), dates of the orbits (and orbital arcs once we achieved the P/3 lunar synchronous orbit with repointing started twice per orbit), and map numbers. Note that the dates and orbits defining Maps 1 and 2 are very slightly revised from earlier publications of *IBEX* data in order to ensure that equivalent ranges of pointing are included in all maps; our data update and release concurrent with this study and future *IBEX* work will use the new map definitions provided here.

Initial ENA observations from *IBEX*'s first six months of science operations, released in the special *IBEX* issue of *Science* magazine, were selected for times of minimal backgrounds, but
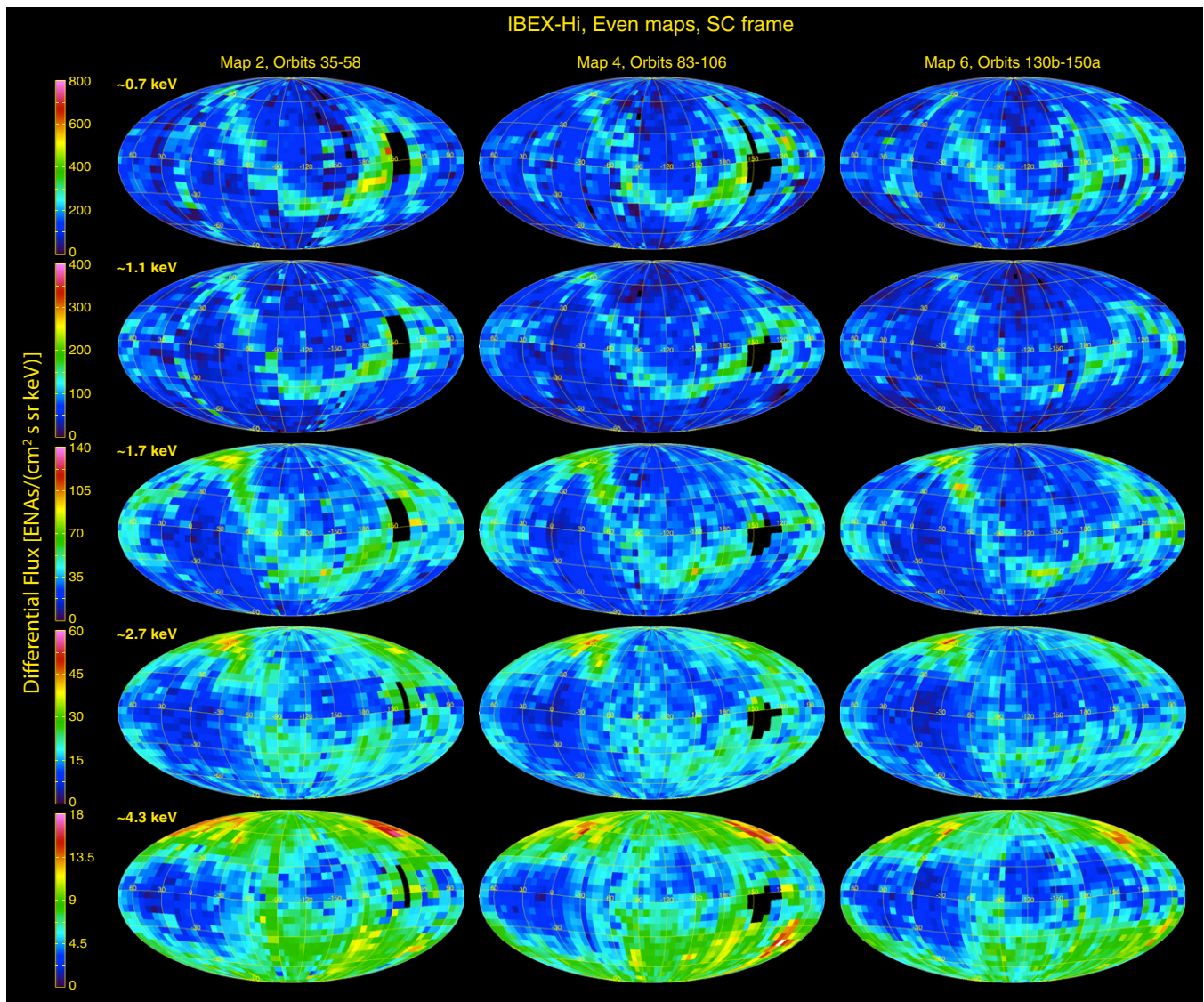
Figure 3. Same as Figure 2, but for Maps 2, 4, and 6.
(A color version of this figure is available in the online journal.)

Table 1
IBEX Orbits and Dates Used to Construct Annual and Six-Month Maps

Year (Annual Maps)	Six-month Maps	Orbit/Arc Numbers	Acquisition Dates (Start/End of Orbits or Arcs)
Year 1 (2009 Map)	1	11–34	2008 Dec 25–2009 Jun 26
	2	35–58	2009 Jun 26–2009 Dec 26
Year 2 (2010 Map)	3	59–82	2009 Dec 26–2010 Jun 26
	4	83–106	2010 Jun 26–2010 Dec 26
Year 3 (2011 Map)	5	107–130a	2010 Dec 26–2011 Jun 25
	6	130b–150a	2011 Jun 25–2011 Dec 24

were (1) largely uncorrected for systematic residual background and (2) shown in the spacecraft frame of reference. Those observations, taken during the anomalously low minimum of the present solar cycle (McComas et al. 2008), were fully adequate for *IBEX*'s initial discoveries such as the Ribbon and globally distributed ENA fluxes. Since this time, the additional five maps as well as several instrument optimization tests have provided key information to further refine our data selection process and develop, validate, and incorporate several correction factors

that improve the accuracy and quality of the data and allow observations from multiple maps to be combined in various physically meaningful ways. Since this study documents the new *IBEX* data release of Maps 3–6 and re-release of Maps 1–2, we summarize the current state of *IBEX* data processing here.

2.1 IBEX-Hi Map Production

IBEX-Hi ENA observations reported in this study are taken at five separate energy steps or channels, representing energy
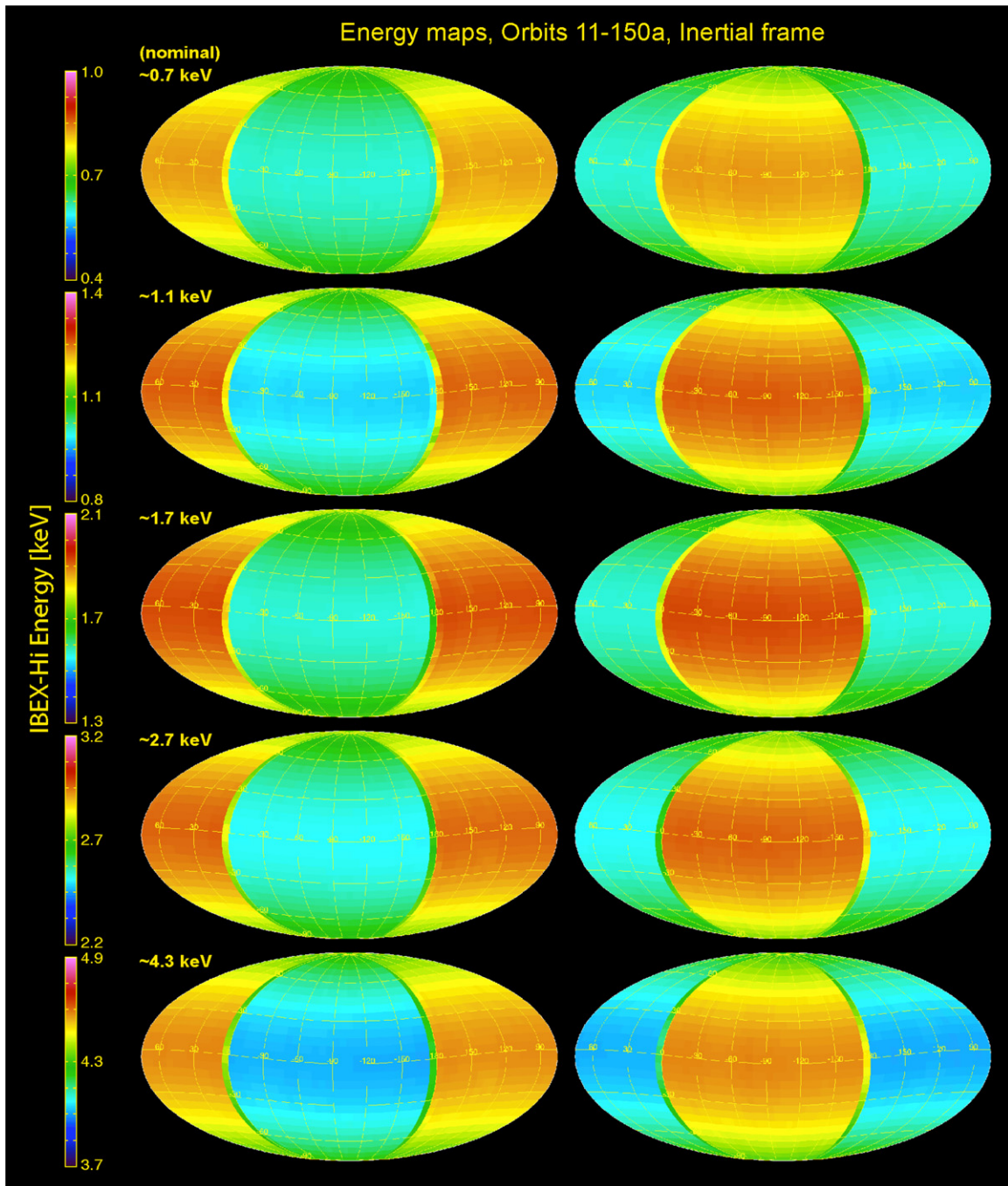
Figure 4. Nominal ENA energies in the heliospheric frame measured for each *IBEX-Hi* energy range for Maps 1 and 2 (other odd and even maps are very similar to Maps 1 and 2, respectively). The C-G effect produces the largest differences at the lowest energies and latitudes, while there is a discontinuous reversal between the ram and anti-ram halves of each map. The intermediate colored stripe in each panel occurs because orbit boundaries do not fall precisely on the sky map grid boundaries. Because the ram vs. anti-ram boundary falls between grid cells, this stripe indicates some intermediate energy values. However, the energies used in analysis are evaluated individually in the ram and anti-ram directions, leaving no ambiguity.

(A color version of this figure is available in the online journal.)

passbands 2–6 of its electrostatic analyzer (ESA; Funsten et al. 2009a) (note that we have omitted the lowest *IBEX-Hi* energy step, which has a higher noise floor). Table 2 provides the best current nominal values and FWHM range for these five energy channels; note that the current values are slightly updated for those provided by McComas et al. (2010) and Funsten et al. (2009a).

IBEX-Hi produces many types of data (see Funsten et al. 2009a), but for this study we analyze only the most certain ENA event detections; these events each register coincident triggers of all three channel electron multiplier detectors within a 96 ns time window. From Orbits 11 to 127, *IBEX-Hi* data were selected on a per orbit basis, while data have been selected on a per orbital arc basis since Orbit 130. Data are culled (removed) when any of the following is present: (1) high count rates in the IBEX Background Monitor (Allegrini et al. 2009), (2) broad spin-phase count enhancements at ESA steps 1–3, (3) a foreground obstruction or ENA source (Earth, magnetosphere, and moon) in the field of view, or (4) a solar energetic particle (SEP) event or "burst" in the counts is identified. The remaining data are
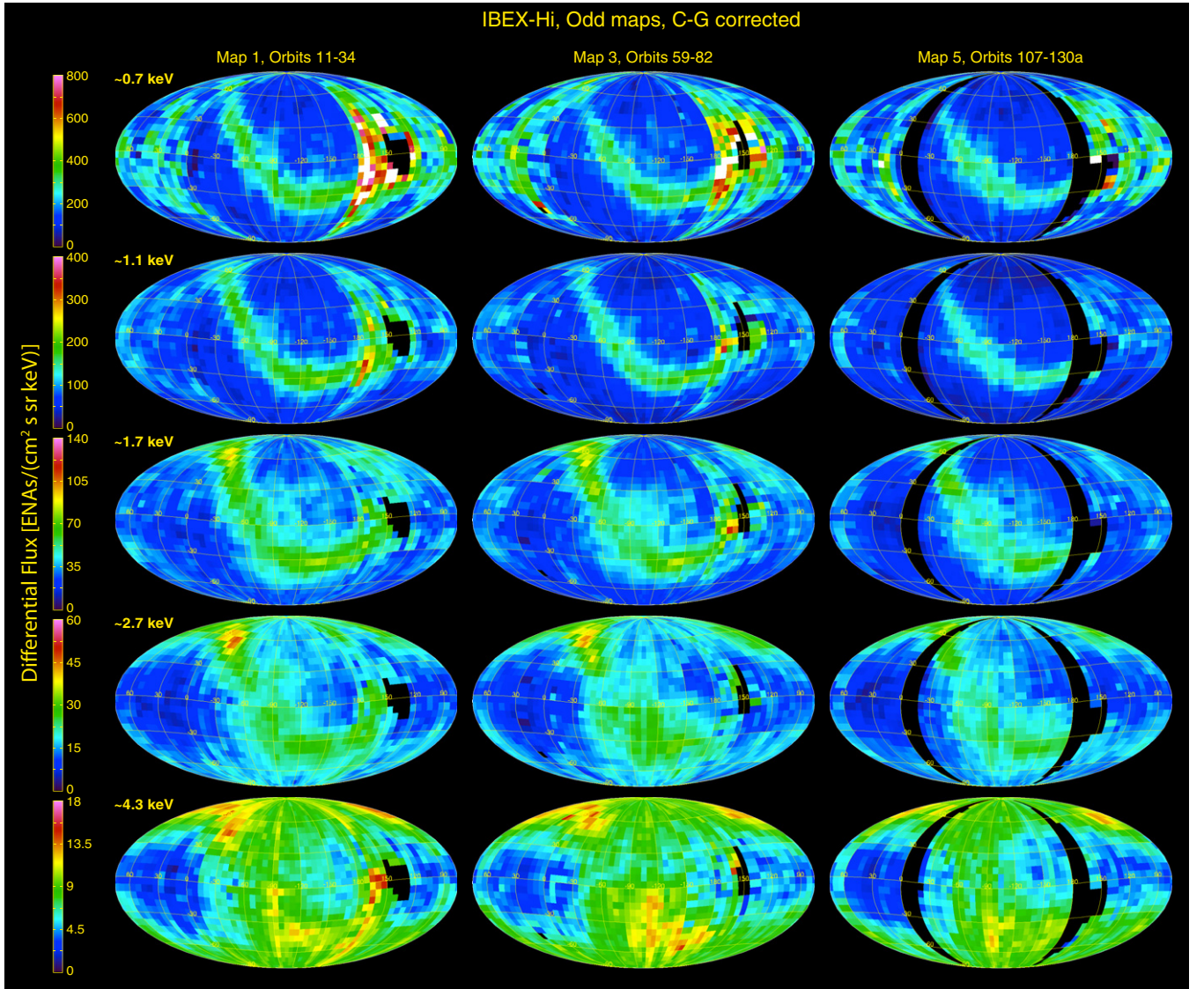
Figure 5. Same as Figure 2, but converted into the heliospheric reference frame using a C-G correction. C-G correction of statistically noisy data around the "hole" on the right side (especially at the lower energies) produces unphysically high fluxes which should be ignored.

(A color version of this figure is available in the online journal.)

Table 2
Energy Passbands for *IBEX-Hi* (Qualified Triple-Coincidence Detections).

E Step	E_{-HM} (keV)	E_{nom} (keV)	E_{+HM} (keV)	$\Delta E/E$
2	0.52	0.71	0.95	0.60
3	0.84	1.11	1.55	0.63
4	1.36	1.74	2.50	0.66
5	1.99	2.73	3.75	0.64
6	3.13	4.29	6.00	0.67

summed by energy step over all angles and histogrammed to quantify the background level; data having a consistently low background level in consecutive ESA settings are retained for scientific analysis.

Using this method and the three years of observations, we have discovered that the primary isotropic background in our data results from counts induced by penetrating radiation from cosmic rays (Reisenfeld at al. 2012), which is found to closely track space- and ground-based neutron monitors (see Appendix A). In contrast to heliospheric ENAs, which preferentially stimulate the detectors in the order in which the ENA transits the sensor (i.e., detector A, then B, and finally C), these cosmic rays generate counts uniformly, often producing coincident events that start with detector C, which is extremely rare with ENAs. Because *IBEX-Hi* reports the rates of these events associated with penetrating radiation, we can correlate the background with independent cosmic ray monitors and accurately subtract these events that masquerade as an isotropic source of heliospheric ENAs (Appendix A).

Using the above method, we have also observed periods within some orbits having a small additional highly isotropic background. We include these times after subtracting the small additional isotropic background only for orbits where statistics are low. This procedure improves the statistical accuracy of the measurement for orbits containing a significant fraction of unusable data due to high backgrounds. We have tested this process within individual maps and between maps, and have demonstrated that intervals with this small, isotropic
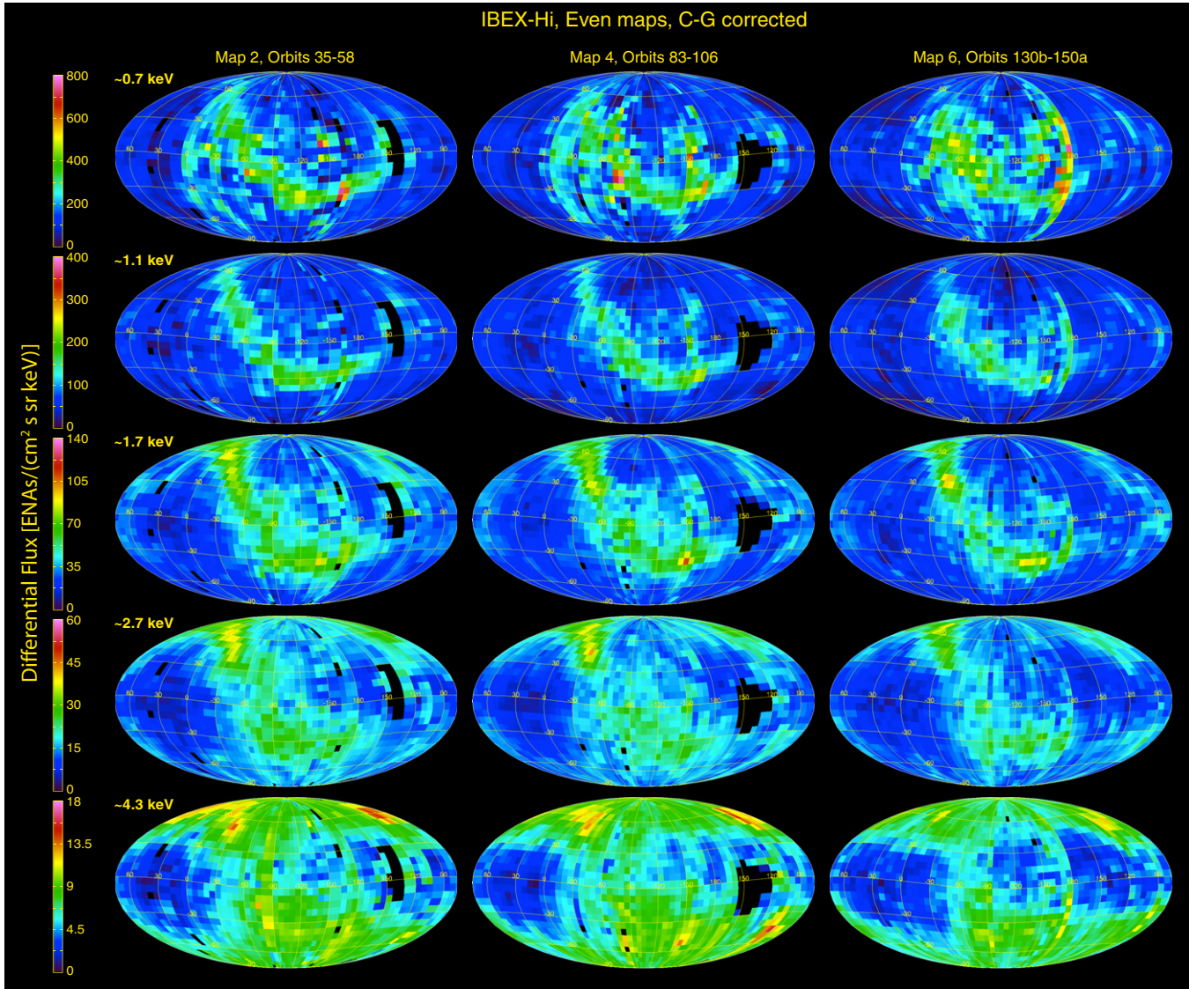
Figure 6. Same as Figure 3, but converted into the heliospheric reference frame using a C-G correction as in Figure 5.
(A color version of this figure is available in the online journal.)

Table 3
Energy Passbands for *IBEX-Lo* (Golden Triple-Coincidence H Detections)

E Step	E_{-HM} (keV)	$E_{Nominal}$ (keV)	E_{+HM} (keV)	$\Delta E/E$ FWHM
5	0.15	0.21	0.30	0.7
6	0.30	0.44	0.61	0.7
7	0.61	0.87	1.22	0.7
8	1.35	1.82	2.62	0.7

background are robust against minor changes to the selection criteria and correction algorithm.

2.2 IBEX-Lo Map Production

IBEX-Lo ENA observations reported in this study are taken at four energy steps or channels, representing the top four energy passbands (5–8) of *IBEX-Lo*'s ESA (Fuselier et al. 2009b) (note that we have omitted *IBEX-Lo*'s lower energy steps, which have higher noise floors and are used primarily for observing very low energy interstellar neutrals). Table 3 provides the nominal values

and FWHM ranges for these four energy channels, updated from Fuselier et al. (2009b).

IBEX-Lo also produces many types of data, but for this study we analyze only hydrogen "golden" triple-coincidence events. A golden triple has a total of four valid times-of-flight (TOFs) from the *IBEX-Lo* TOF system and the sum of the long TOF plus the delay line signal (which determines the detector quadrant) is equal to the sum of the two shorter TOFs (Fuselier et al. 2009b). The culling procedure for *IBEX-Lo* is similar to that of *IBEX-Hi*, but it is not exactly the same because there are different backgrounds in the two sensors. For *IBEX-Lo*, data are culled out whenever (1) the spacecraft is downstream of Earth's bow shock, or (2) there is a foreground object (Earth, magnetosphere, and moon) in the field of view. For the highest two energy channels, remaining data are summed by energy and separately over two spin angle ranges from 0° to 180° and from 180° to 360°. A second empirically derived culling removes any 64 spin interval (∼960 s) where the golden triple count rate exceeds 3 counts in any 180° angle range for the combined highest two energy channels. The maximum count rate for this culling process was determined by comparing *IBEX-Lo* and background
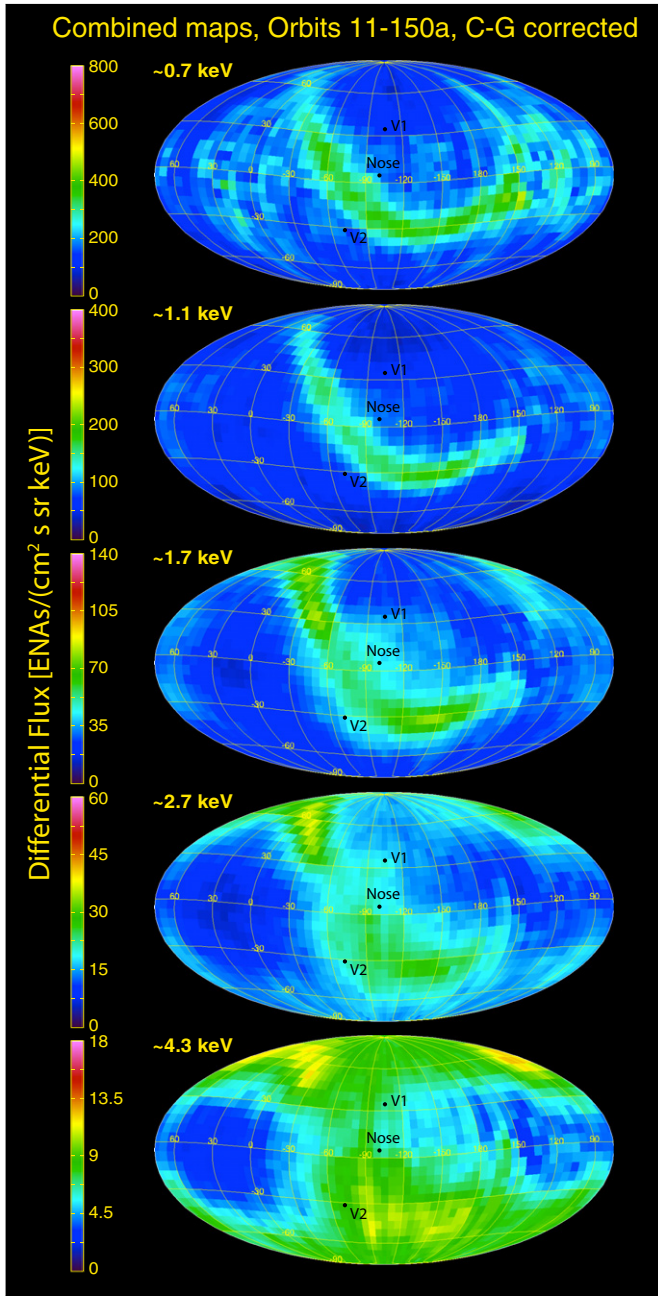
Figure 7. Combined Maps 1–6 of ENAs in the heliospheric reference frame observed at 1 AU, based on C-G corrected and statistically combined ENA observations over the first three years of *IBEX* measurements. Same format as columns in Figures 2–6. The three points indicate the locations in the sky maps of Voyagers 1 and 2 (V1 and V2) and the slightly revised direction of the Sun's motion with respect to the interstellar medium from *IBEX-Lo* observations (McComas et al. 2012, and references therein).

(A color version of this figure is available in the online journal.)

monitor count rates over the first year of *IBEX* operations. This removes intervals with energetic ion background from, for example, Earth's foreshock region upstream of the bow shock. The remaining *IBEX-Lo* data are retained for analysis. Details of the *IBEX-Lo* map processing is described in Fuselier et al. (2012).

2.3 Yearly IBEX-Hi Maps in the Spacecraft Frame

Figures 2 and 3 present in our usual Mollweide projection, ENA fluxes observed in the *IBEX-Hi* odd (1, 3, 5) and even

(2, 4, 6) maps, respectively. These "raw" flux maps are in the spacecraft frame of reference and have only been corrected for the time-variable cosmic ray background and, in orbits with few low background data, additional data have been included after removal of a small, intermittent isotropic background as described above. Each column represents observations from one of the six maps while the rows show ENA fluxes from *IBEX-Hi* at energy steps 2–6. We use the same color bars for each energy passband on all figures throughout this study. Black regions indicate no data; the small holes on the right sides of the plots near the equator are regions where the magnetosphere blocks *IBEX*'s viewing of the outer heliosphere; pixels adjacent to this blockage tend to have very low counting statistics and additional backgrounds that are hard to remove, so these regions need to be interpreted very carefully. The missing swath in Map 5 (Orbits 128 and 129) is from the roughly two weeks that the *IBEX* science instruments were off as we maneuvered into our new P/3 lunar synchronous orbit. The spacecraft velocity in the heliospheric reference frame (i.e., Earth's ~30 km s^{-1} orbital motion about the Sun) introduces a significant aberration in both ENA energy and velocity vector that appears as a systematic flux variation in these maps.

The Compton–Getting (C-G) effect is produced by spacecraft motion, with the measured ENA energy and angle arising from the vector sum of its velocity in the heliospheric reference frame and the spacecraft velocity. In the direction of spacecraft motion (ram direction), ENAs have a lower energy and come from lower latitudes in the heliospheric reference frame than measured. Alternately, in the opposite direction of spacecraft motion (anti-ram direction) ENAs have a higher energy and come from higher latitudes in the heliospheric reference frame than measured. Figure 4 provides the actual (heliospheric frame) nominal energy of measured ENAs in Map 1 (left column) and Map 2 (right column) for the five *IBEX-Hi* energy ranges.

Clearly the ram and anti-ram portions of the maps in the spacecraft frame are measuring very different energy ENAs. Because the flux of heliospheric ENAs decreases with increasing energy, the measured flux in the ram direction is at lower heliospheric energies than in the anti-ram direction, resulting in higher fluxes. The magnitude of this effect, of course, is energy- and spin-angle- (latitude-) dependent and impacts the lowest energies and lowest latitudes the most. These differences are evident in Figures 2 and 3, where the central region exhibits higher fluxes in the odd maps and the two outer edges show higher fluxes in the even maps.

2.4. IBEX-Hi Maps in the Inertial Frame

In order to adjust the data to represent observations in a fixed energy range over the whole sky, one needs to remove the effects of the spacecraft motion. This C-G correction uses fluxes measured at multiple energies to calculate corrections in both energy and angle of the observed ENAs. *IBEX*'s C-G correction is described in detail in the Appendix of McComas et al. (2010); since that publication, continued validation and optimization of the C-G correction algorithm has resulted in only two minor coding improvements that have been included in the automated C-G software production code for this study. Figures 5 and 6 show the odd and even maps including the C-G corrections. While the characteristic differences between the central and edge portions of the non-C-G-corrected maps have largely disappeared in these maps, it is important to remember that the C-G correction is derived from interpolation
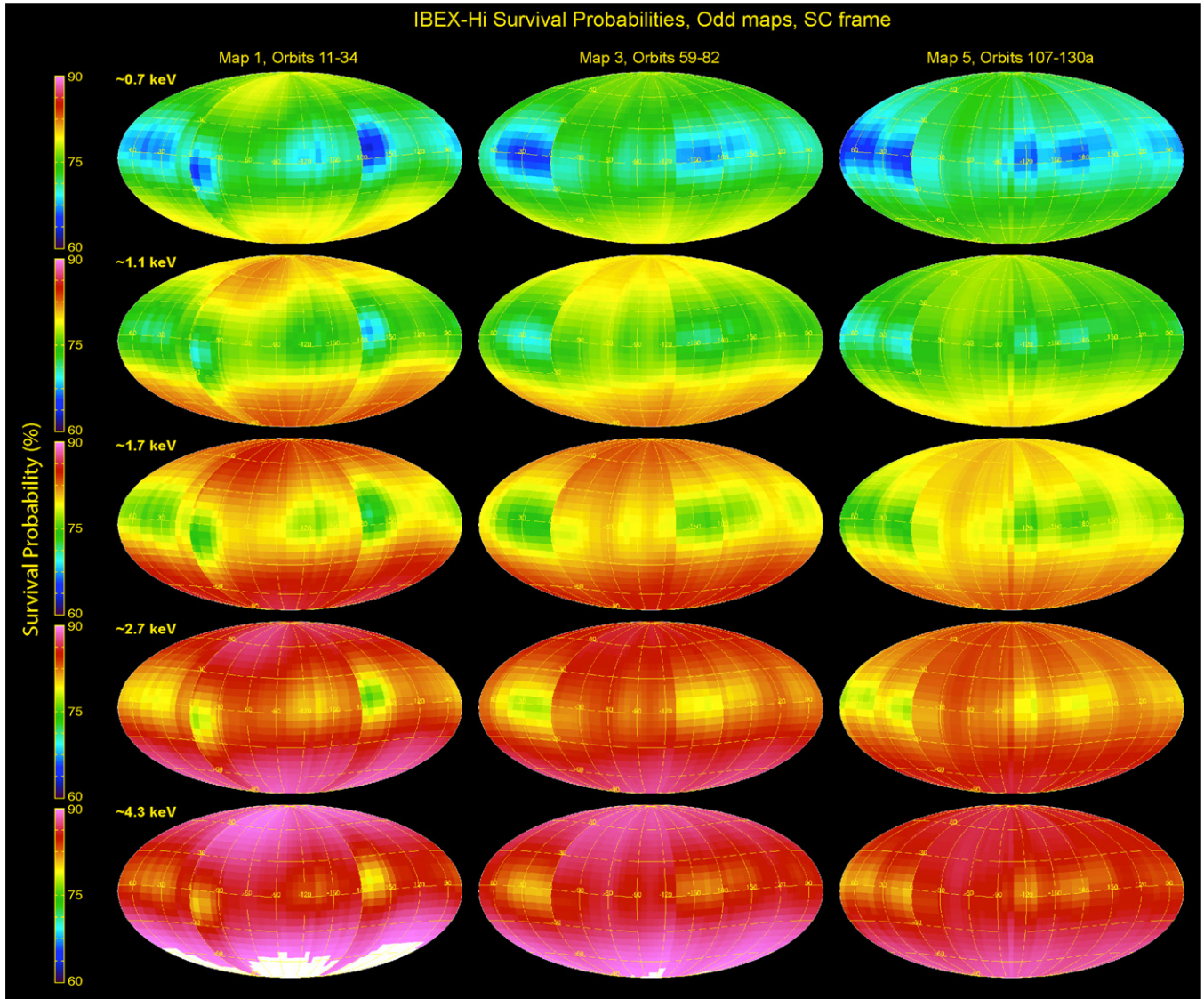
Figure 8. Mollweide projections of survival probabilities of ENAs from the outer heliosphere in to 1 AU as a function of *IBEX-Hi* energy step (rows) for odd maps (1, 3, 5).

(A color version of this figure is available in the online journal.)

of the measured energy spectrum in each viewing pixel. While considerable effort has been spent on optimizing, testing, and verifying the C-G correction and its robustness to spatially and spectrally localized anomalous data, the C-G maps represent inferred ENA flux rather than a direct observation. This fact is important when looking for relatively subtle temporal changes between the maps, as we do later in this study.

Figure 7 displays sky maps that combine observations from the full three years of *IBEX* observations. The observations have first been C-G corrected, which is required to combine odd and even maps and then averaged using their statistical uncertainties. These sky maps represent the "best" current ENA flux measurements at *IBEX* in the heliospheric reference frame with the lowest statistical uncertainties and should be used as the basis for any study that is not specifically trying to examine the temporal evolution of the heliosphere. The *IBEX* team strongly recommends that subsequent studies and comparisons with models and theories use these maps for the baseline *IBEX* observations at fixed energies at 1 AU.

2.5. ENA Survival Probability Correction of the IBEX Maps

The earlier study of possible time variations in the *IBEX* data, McComas et al. (2010), examined the effects of the survival probability of ENAs transiting in from the outer heliosphere to 1 AU. Those authors examined only Maps 1 and 2, which were collected almost entirely during 2009, in the midst of the longest and deepest solar minimum in the space age (McComas et al. 2008). They found that differences in the survival probabilities between these two maps were less than ~10% and instead of trying to explicitly correct for them, those authors used this difference as an uncertainty to be considered in the interpretation of the observed temporal changes.

In this study, for the first time we explicitly correct for the energy-dependent and time-variable survival probabilities for ENAs to reach *IBEX* from all directions in the outer heliosphere. This correction includes radiation pressure and the loss (extinction) of ENAs from photoionization and ionization via charge exchange with solar wind protons. Because both solar
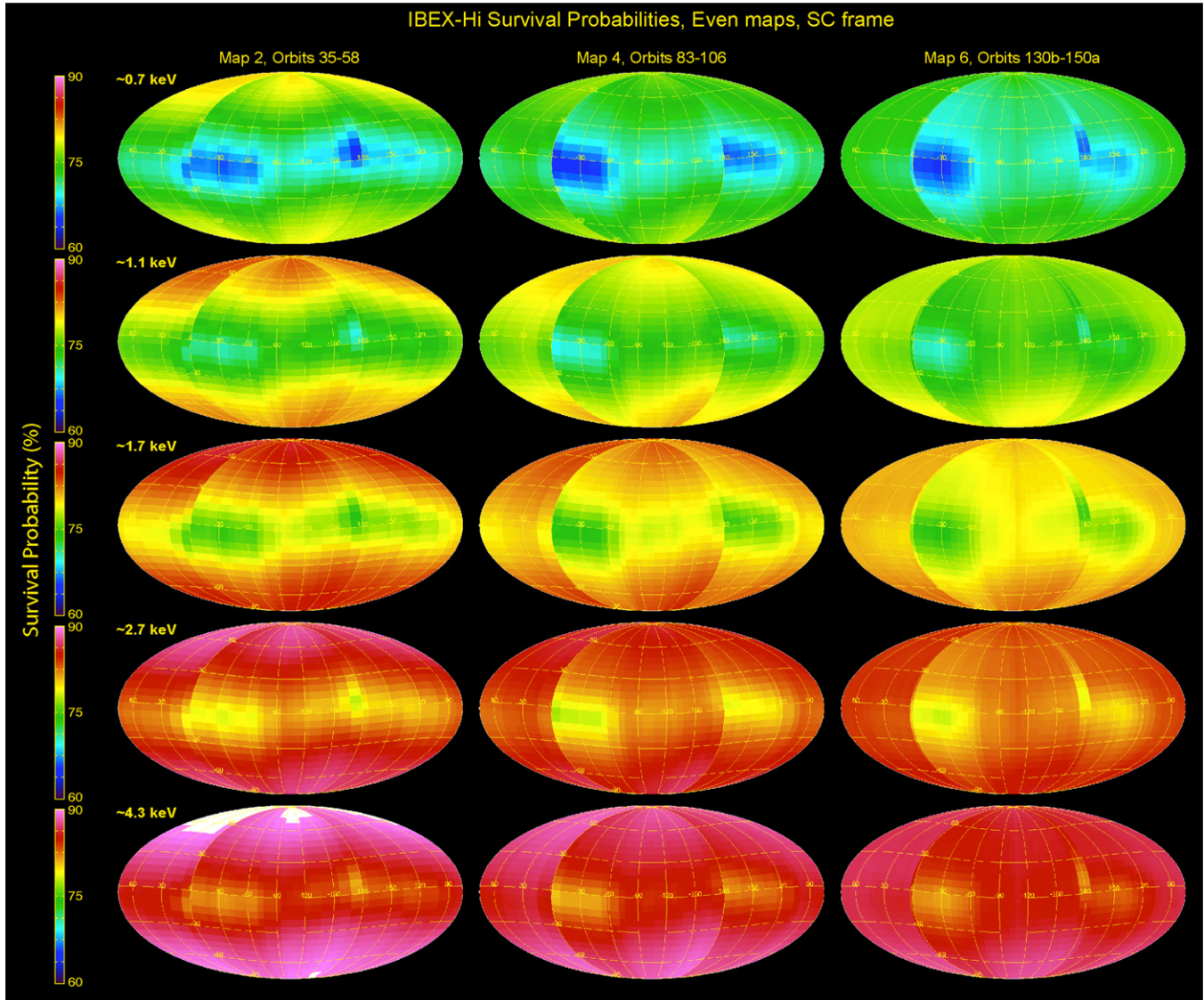
Figure 9. Same as Figure 8, but for even maps (2, 4, 6).
(A color version of this figure is available in the online journal.)

EUV and solar wind fluxes fall off roughly as the square of the radial distance from the Sun, the vast majority of the losses occur in the last few AU of travel into the inner heliosphere. In addition, because both solar EUV and solar wind can vary significantly on timescales of hours to days, and since the viewing geometry is slightly different from orbit to orbit relative to the Sun-Earth line, independent, empirical correction factors are needed for each orbit. The detailed process for calculating the orbit-by-orbit survival probabilities used in this study is documented in Appendix B.

Figures 8 and 9 show the calculated survival probabilities for each of the five *IBEX-Hi* maps, while Figures 10 and 11 show these probabilities for each of the four *IBEX-Lo* maps. It is apparent from these figures that different orbits can have significantly different survival probabilities that are related to the latitude-dependent energies observed at each instrumental energy step (see Figure 4). It is also clear that losses are greater (smaller survival probabilities) in general at lower energies, owing largely to their lower speeds and the longer times these ENAs spend in transit as well as somewhat higher charge-exchange cross

sections. As a consequence, survival probabilities partly compensate for C-G effects because the ENAs observed in the ram hemisphere have lower energies in the heliospheric frame than those observed in the anti-ram hemisphere and thus the survival probabilities of the ENAs seen in the ram hemisphere are generally lower than the survival probabilities of ENAs observed in the anti-ram hemisphere. The apparent abrupt discontinuities in survival probabilities between the centers and edges of these maps is produced where the maps jump from ram to anti-ram viewing, which are taken six months apart, as opposed to the temporally contiguous swaths at all other times.

Using the survival probabilities above, we correct each pixel in the *IBEX-Hi* C-G-corrected sky maps by dividing the ENA flux in a pixel by the calculated survival probability for that pixel (which is always <1). Figures 12–14 provide the individual and combined sky maps equivalent to Figures 5–7, corrected for ENA survival probabilities. Thus, these figures represent our best knowledge of ENA fluxes in the outer heliosphere, before some fractions are lost on their way in to 1 AU (where they are observed by *IBEX*). Again, the *IBEX* team strongly suggests
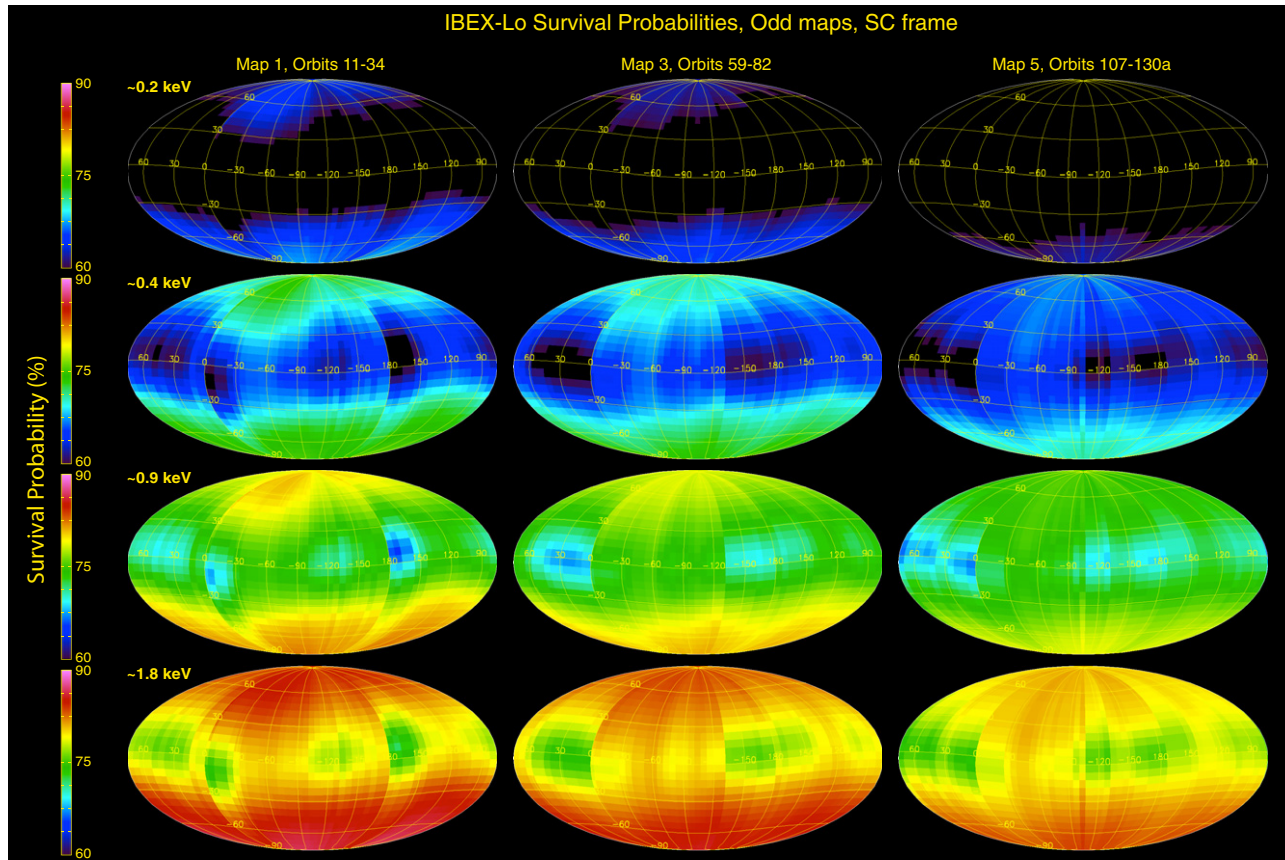
Figure 10. Same as Figure 8 (odd Maps 1, 3, 5), but for *IBEX-Lo* energy steps (rows).
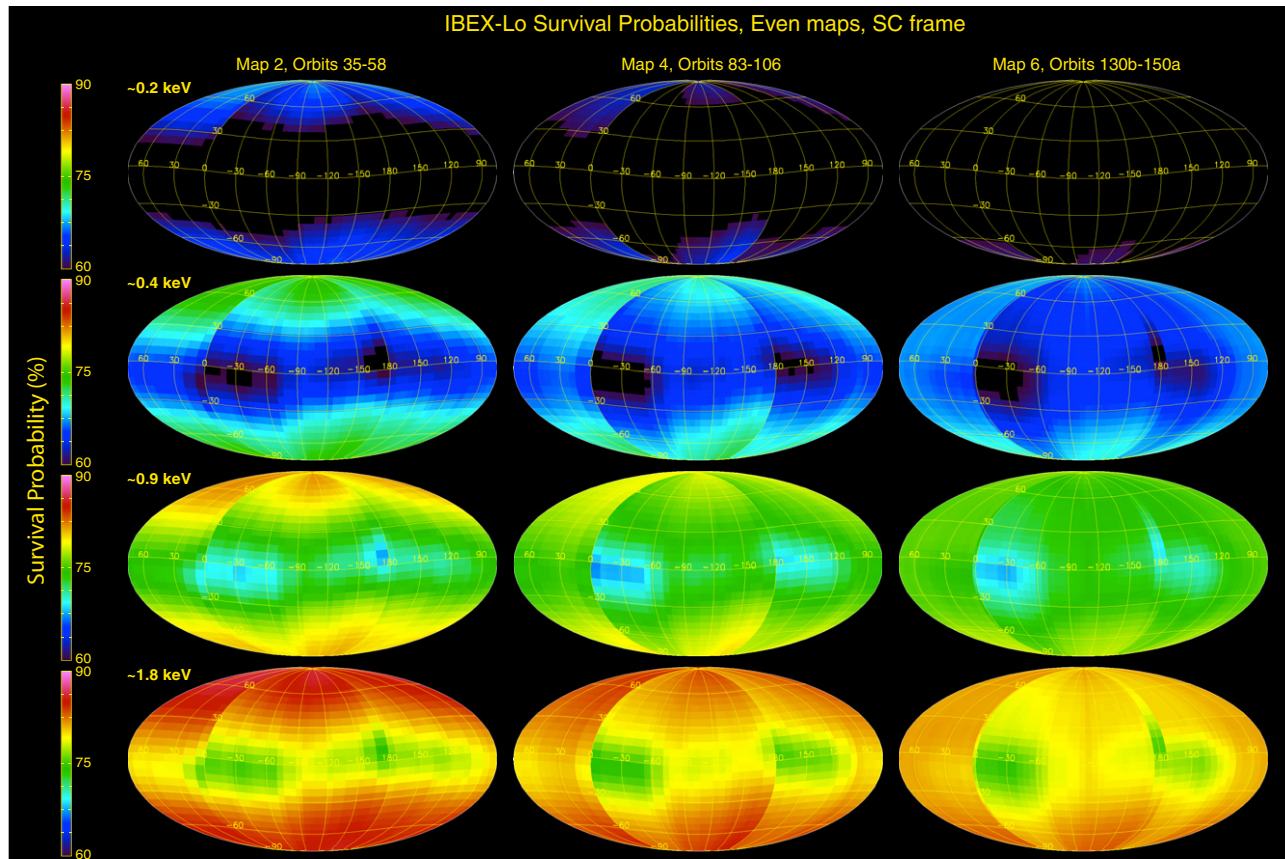(A color version of this figure is available in the online journal.)

Figure 11. Same as Figure 10, but for even maps (2, 4, 6).
(A color version of this figure is available in the online journal.)
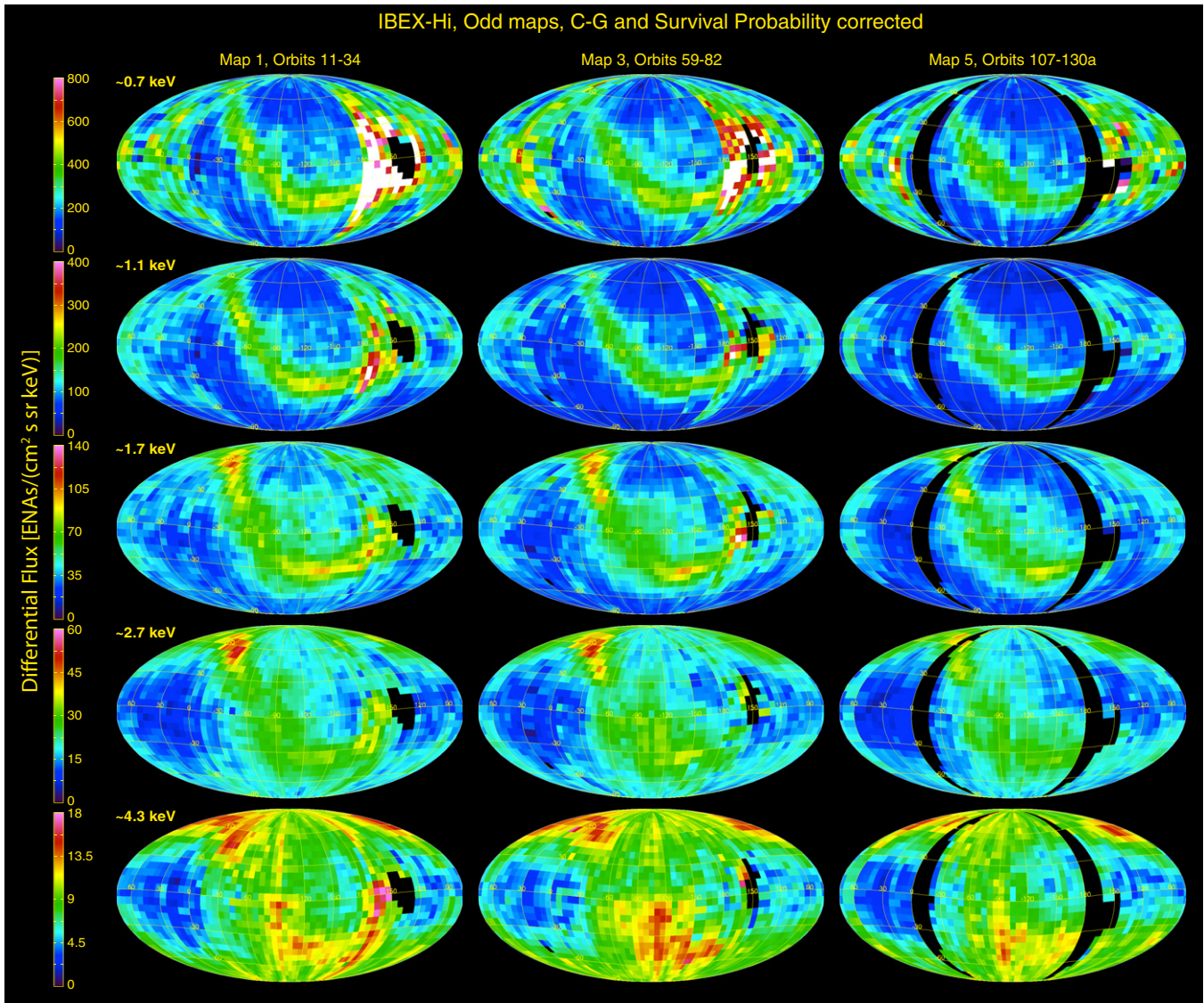
Figure 12. Survival probability corrected ENA fluxes, representative of inward-directed ENA fluxes in the outer heliosphere, before any losses. Data are C-G corrected and show the odd maps (1, 3, 5). Again, C-G correction of statistically noisy data around the "hole" on the right side (especially at the lower energies) produces unphysically high fluxes which should be ignored.

(A color version of this figure is available in the online journal.)

using the fluxes in Figure 14 as the current best representation of ENA fluxes from the outer heliosphere (but inside the region where they are generated), as viewed at 1 AU.

2.6. Ram and Anti-ram IBEX Maps

Because of the uncertainties associated with the spectral interpolations used in the C-G corrections, in this study we also introduce another entirely new type of sky map, which combines data taken over an entire year of observations in the spacecraft frame. These maps are labeled "ram" and "anti-ram" depending on whether the data are from the half of *IBEX*'s rotation facing toward (ram) or away from (anti-ram) the spacecraft's motion (prograde direction of Earth's orbital motion—see Figure 1). Figure 15 show the ram maps for years 2009–2011, while Figure 16 displays the anti-ram maps for these three years. It is important to note that ram and anti-ram maps cannot be directly compared with each other, owing to the fact that the spacecraft motion causes them to sample different energies. However, these annual maps are ideal for looking for time variations on yearly

timescales as no C-G corrections are required and each pixel in the map represents the same viewing and motion of spacecraft from one year to the next.

For completeness, Figures 17 and 18 show the ram and anti-ram maps, produced by statistically combining all data from the first three years of observations. The ram maps (15 and 17) appear significantly brighter at each energy step than the anti-ram maps (16 and 18) because the spacecraft motion causes these maps to sample lower energies, and thus higher fluxes, of ENAs at each energy step. This difference in energy is also one of the reasons that the anti-ram maps, which measure lower fluxes of higher energy particles, have larger statistical variations and appear nosier than the ram maps.

While this paper primarily focuses on *IBEX-Hi* ENA data, we also include maps for *IBEX-Lo* energies from ~0.2 to 1.8 keV. Figure 19 shows *IBEX-Lo* ram and anti-ram maps, respectively. The statistical accuracy of these maps is significantly lower than for *IBEX-Hi* owing to smaller geometric factors in the overlapping energies and additional backgrounds. For example, the
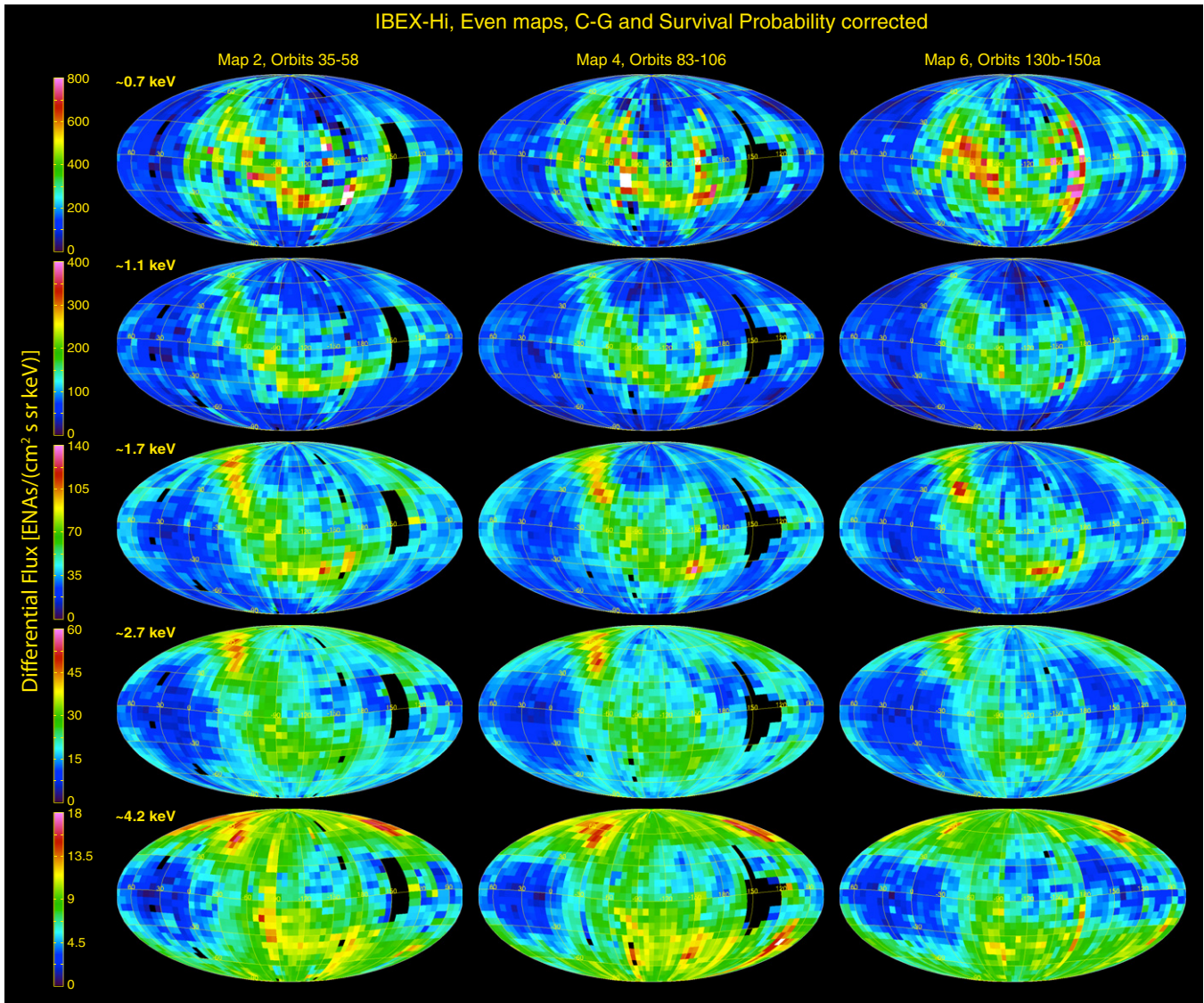
Figure 13. Similar to Figure 12, but for even maps (2, 4, 6).
(A color version of this figure is available in the online journal.)

IBEX-Lo ram maps at energies below 0.2 keV are almost completely dominated by the distributions of the interstellar neutral H and He flow at 1 AU (Möbius et al. 2009, 2012; Bzowski et al. 2012a; Saul et al. 2012). The visibility of secondary interstellar He from the outer heliosheath in the early ram orbits (Bzowski et al. 2012a) and the shift of the H flow because of solar radiation pressure to late orbits (Saul et al. 2012) obscure a large portion of the ram sky maps from December through April each year. In addition, *IBEX-Lo* has very high background when it is in the magnetosheath and magnetotail (except during relatively rare magnetotail lobe crossings). Therefore, the available data for the two sets of maps each cover only a little more than half the sky. Nonetheless, these maps are very important because they use different sensor technologies for conversion of the ENAs to ions: via transmission through thin carbon foils for *IBEX-Hi* (Funsten et al. 2009a) and by reflection from a chemical vapor deposition diamond surface for *IBEX-Lo* (Fuselier et al. 2009b). Thus, the *IBEX-Lo* maps provide truly independent verification of the most critical and surprising *IBEX-Hi* observations (McComas et al. 2009b)—the existence, location, and approximate ENA flux level of the *IBEX* Ribbon.

The *IBEX-Lo* maps extend our understanding of the heliospheric ENA fluxes to lower energies than possible with *IBEX-Hi* alone. In particular, the observations show that the low-latitude Ribbon seems not just to be narrowest at ∼1 keV, but becomes increasingly broad (and dims) at lower energies, just as it does at energies above ∼1 keV. In addition, the *IBEX-Lo* data indicate something that looks like the deflected tail in anti-ram maps (left side of anti-ram maps in Figure 19) all the way down to 0.2 keV. This feature further reinforces the conclusion that the offset heliotail is an important large-scale structure of the heliosphere.

2.7. IBEX-Hi Maps of the Spectral Index

Figure 20 again shows statistically summed data from the ram and anti-ram maps for years 1–3. However, this time, instead of fluxes, the maps display the energy spectral index (γ) calculated as a best linear fit to the five energy steps of *IBEX-Hi* data. Similarly, Figure 21 shows the same maps, but including the survival probability corrections. We have not included the full C-G correction in these maps, but do correct the energy for the
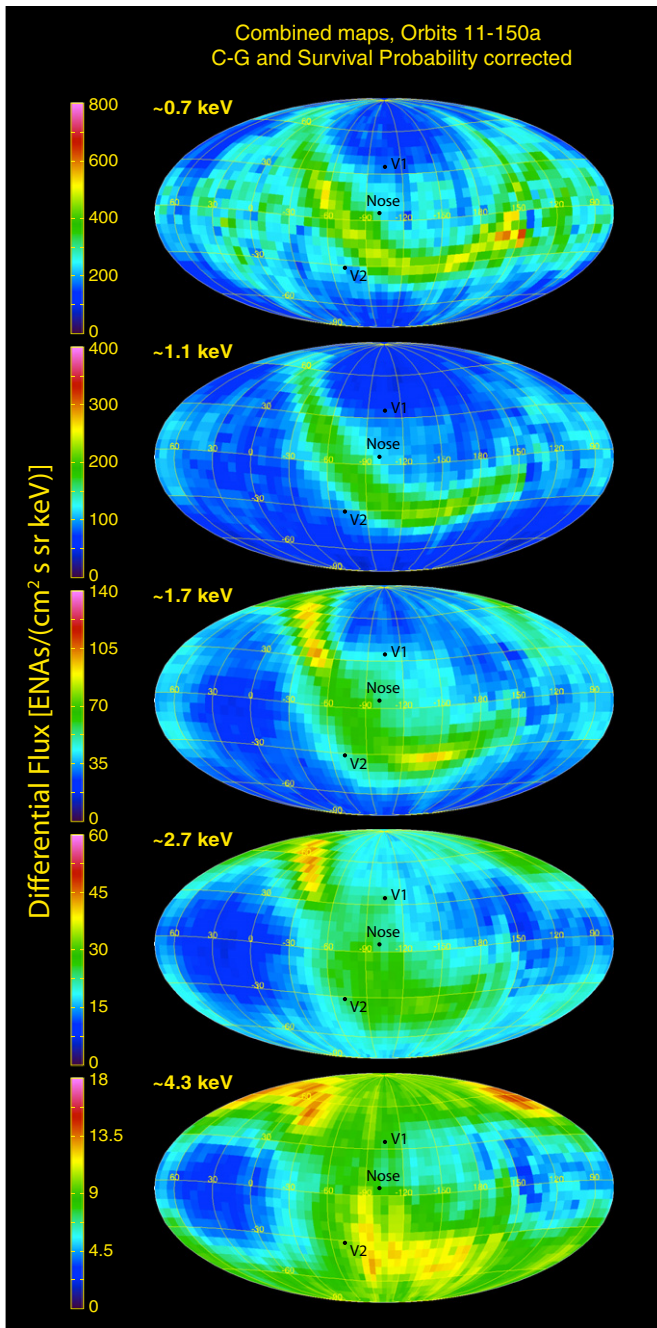
Figure 14. "Best" statically combined survival probability corrected maps, representative of inward-directed ENA fluxes in the outer heliosphere, before any losses. Data are C-G corrected and in a format similar to Figure 7. Again, C-G correction of statistically noisy data around the "hole" on the right side (especially at the lower energies) produces unphysically high fluxes which should be ignored.

(A color version of this figure is available in the online journal.)

spacecraft's motion on a pixel-by-pixel basis, effectively putting the observations in the inertial frame of the Sun, as was done in McComas et al. (2009b). However, in contrast to the spectral maps in that study, which only used a single-fit parameter, these spectral index maps allow for two free parameters, the slope and offset. While the former showed very little evidence for the Ribbon as a unique spectral feature, the latter (this study) clearly shows the Ribbon at low latitudes with significantly higher values of γ than the adjacent regions. This significant difference in the Ribbon was also previously shown by Schwadron et al.

(2011), who also explicitly separated the Ribbon ENAs from the globally distributed flux.

The spectral maps in Figures 20 and 21 show a number of interesting features in addition to the clearly visible Ribbon. In particular, at low latitudes on the interstellar upwind side (toward the nose of the heliosphere; middle region of the maps), the spectral slope is generally lower outside the Ribbon, approaching $\gamma \sim 1.5$, which corresponds to the limiting behavior of a kappa distribution ((Livadiotis & McComas 2009), indicating particle distributions as far from equilibrium as possible (Livadiotis & McComas 2010). This index is higher (>2) in the Ribbon and other localized regions toward the nose. In contrast, the entire low-latitude region on the downwind (tail) side at low latitudes has a larger spectral index, ranging from $\gamma \sim 2$ to 3. This value seems to persist not just in the offset heliotail region, but across all longitudes in the downwind hemisphere. This may simply be because the flows in this region of the inner heliosheath are directed on average at increasing large oblique angles to *IBEX*'s radial line of site as they approach the heliotail. In the frame of the Sun (and roughly *IBEX*), such flows produce fewer ENAs at higher energies and more at lower energies owing to their increasingly tailward motion.

At high latitudes, the spectral maps show: (1) no obvious Ribbon spectral feature, and (2) largely featureless spectral slopes with a value of $\gamma \sim 1.5$. Of course, the linear approximation for the spectral shape tends to break down in the polar regions, which show an inflection with enhanced fluxes at higher energies (McComas et al. 2009b). Recently, Dayeh et al. (2012) examined the polar ENA spectra from Maps 1 to 5 and showed that there is a persistent flattening of the ENA spectrum between ~1 and 2 keV. This break indicates that the polar regions have an ENA source at higher energies, most likely from pick-up ions in the fast solar wind. Nonetheless, the very narrow range of single spectral slope values at high latitudes shown here, independent of longitude, could indicate little importance of the asymmetric external dynamic pressure away from the equatorial region. It could also indicate the composite nature of the flows over the poles, where both fast high-latitude solar wind and slow low-latitude solar wind from near the nose (and their pickup ions) are both observed in these line-of-sight integrated pixels.

3. TIME VARIATIONS IN *IBEX-Hi* OBSERVATIONS

Beyond showing the full first three years of *IBEX* observations (2009–2011), a second major aspect of this study is to provide a detailed examination of time variations of these observations. While the results qualitatively agree with those shown by McComas et al. (2010) for time evolution between Maps 1 and 2, the present study provides far better statistics and includes important corrections informed by the three years of observation and analysis and in situ sensor tests and calibration. Because the McComas et al. (2010) study was done at the end of the first year of observations, these authors could only compare C-G-corrected maps, which had significant spectral interpolation uncertainties in the fluxes. In addition, while these authors showed that the survival probabilities of ENAs were very similar (less than ~10% different) for the first two maps, they did not include any correction for this effect. Here, with three full years of data, we do explicitly correct for variations in the survival probabilities on an orbit-by-orbit basis and look for time variations by comparing annual ram maps separately from anti-ram maps. In this section, we examine the global temporal variations in *IBEX-Hi* detector background and survival probability corrected ENA fluxes between 2009–2011.
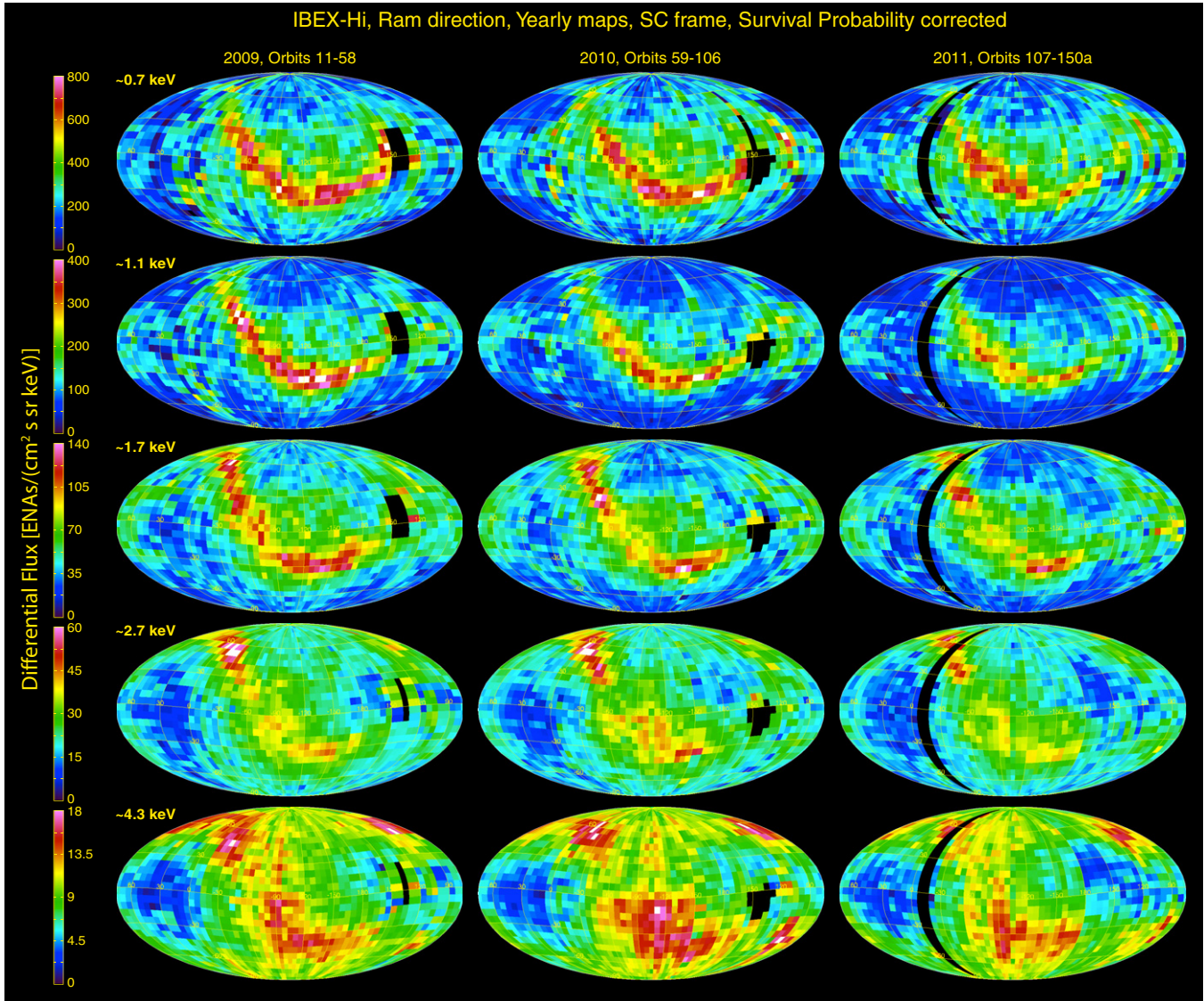
Figure 15. Annual "ram" maps for 2009–2011 (columns), produced by combining observations from times when the aperture was pointed in the hemisphere of the spacecraft's motion from each odd and even pair of maps. Fluxes are corrected for survival probabilities, but not C-G corrected.

(A color version of this figure is available in the online journal.)

Even with the enhanced statistics and various corrections included in this study, it is important to look for time variations with a critical eye. In particular, we do not try to interpret variations in individual or small groups of pixels. Instead, we insist that real features and time variations (1) be observable over significant regions, (2) be present in both survival probability corrected and uncorrected data, (3) evolve over several ENA energies, and (4) where statistically possible, be observable in both *IBEX-Hi* and *IBEX-Lo* to provide independent confirmation. In contrast, background features tend to produce large variations from orbit to orbit over a broad range of spin angles, tend to disappear with various corrections, tend to be localized in a particular energy channel (especially the lowest energy channels), and tend to be sensor specific. Finally, background features tend to appear and be enhanced in one direction (like the ram only maps), while real features such as the Ribbon have characteristic changes from ram to anti-ram that can be readily explained by the change in energy going from a ram to anti-ram map.

Careful comparison of Figures 15 and 16 shows several global differences over time. In particular, the progression from 2009 to 2011 indicates a small but consistent reduction (dimming) in the overall ENA fluxes at all energies. Figures 22 and 23 make these differences easier to see by plotting the percentage difference between the 2009 and 2010 maps (middle column) and 2009 and 2011 maps (right column). In both, an increase over time is indicated by red and a decrease by blue, with lighter (brighter) colors indicating larger differences. While there are red and blue pixels in all maps, several important systematic variations can be seen. First, there are clearly more blue pixels than red ones in essentially all maps and more blue pixels in the 2011–2009 (third column) than in the 2010–2009 (middle column) maps. This indicates progressive reductions in ENA fluxes from 2009 to 2010 and then again from 2010 to 2011 (see below for quantitative analysis). These reductions are evident at essentially all latitudes and not just, for example, the poles or the equator. The Ribbon especially, as seen most clearly in the ~1.1 and 1.7 keV ram maps, stands out as a prominent structure with significant reductions. Another interesting aspect is that while most of the sky marks reductions in ENA fluxes, the direction toward the offset heliotail (best seen near the left
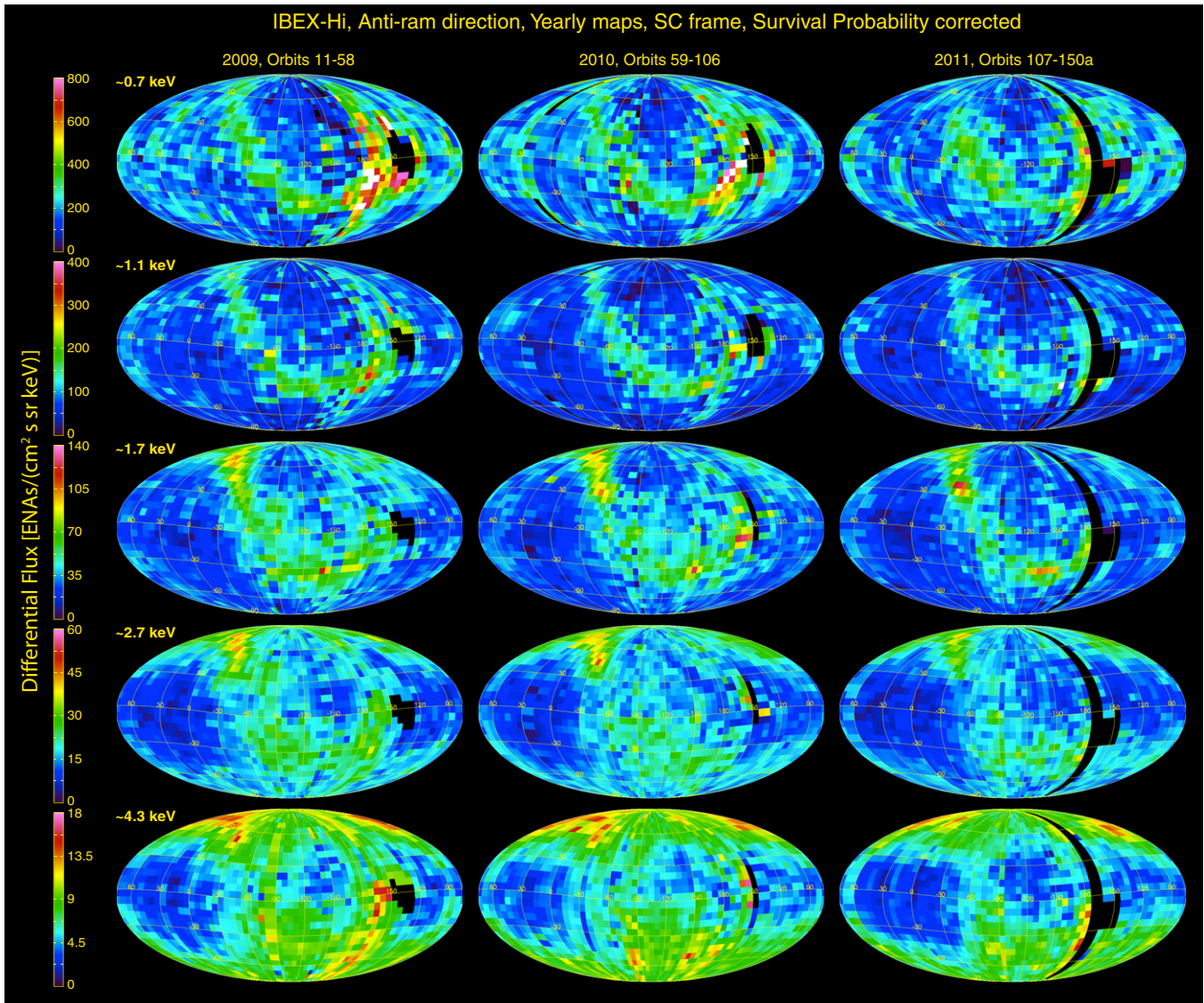
Figure 16. Similar to Figure 15, but for "anti-ram" observations.
(A color version of this figure is available in the online journal.)

sides and extending around to the far right at the two highest energies) indicate persistent increases over the three years at most energies.

We further quantify the ENA variations by summing fluxes over several large regions of the sky, similar to what was done by McComas et al. (2010), but adding in this analysis the offset heliotail region (Region 4) and explicitly including survival probability corrections. Figure 24 shows the four regions of integration and their designations.

Figure 25 shows the time variations from year to year for each region and for the full sky, separately for each of the five *IBEX-Hi* energy bands. Similarly, Table 4 provides quantitative changes from 2009 to 2011. Fluxes used to quantify the variations are all corrected by their respective survival probabilities, but because we use annual ram maps, no C-G correction is required. In addition, for this analysis only, we culled a few additional pixels from the integrations because the variance was extreme (larger than the pixel's flux value). In both Figure 25 and Table 4, error bars represent statistical errors only.

All regions of the maps except the tail show significant dimming over the 2009–2011 timeframe, with the 1.1 keV energy

channel being most reduced. Compared to the preliminary results in McComas et al. (2010), based on C-G-corrected versions of only the first two maps, this study finds a somewhat slower decrease in ENA flux, which average from less than 5% to over 10% per year, depending on the energy band and region. Much of the difference is due to (1) the removal of the time variable (decreasing) cosmic ray background and (2) correction for the generally decreasing ENA survival probabilities in this study, both of which are in the direction of reducing the real decreases in the ENA fluxes. However, with these careful corrections and the comparison of ram and anti-ram data, which avoids all of the uncertainties introduced by spectral interpolations in the C-G corrections, this study definitively establishes the statistically significant time variations for all regions of the sky over the 2009–2011 epoch.

The results for the tail are particularly interesting as they indicate an enhancement in ENA flux at energies other than 1.1 keV. Because of the expected long integration paths down the tail (hundreds of AU instead of tens of AU toward the nose) fluxes from this region should represent a combination of solar wind and pickup ions that span back many years to much earlier
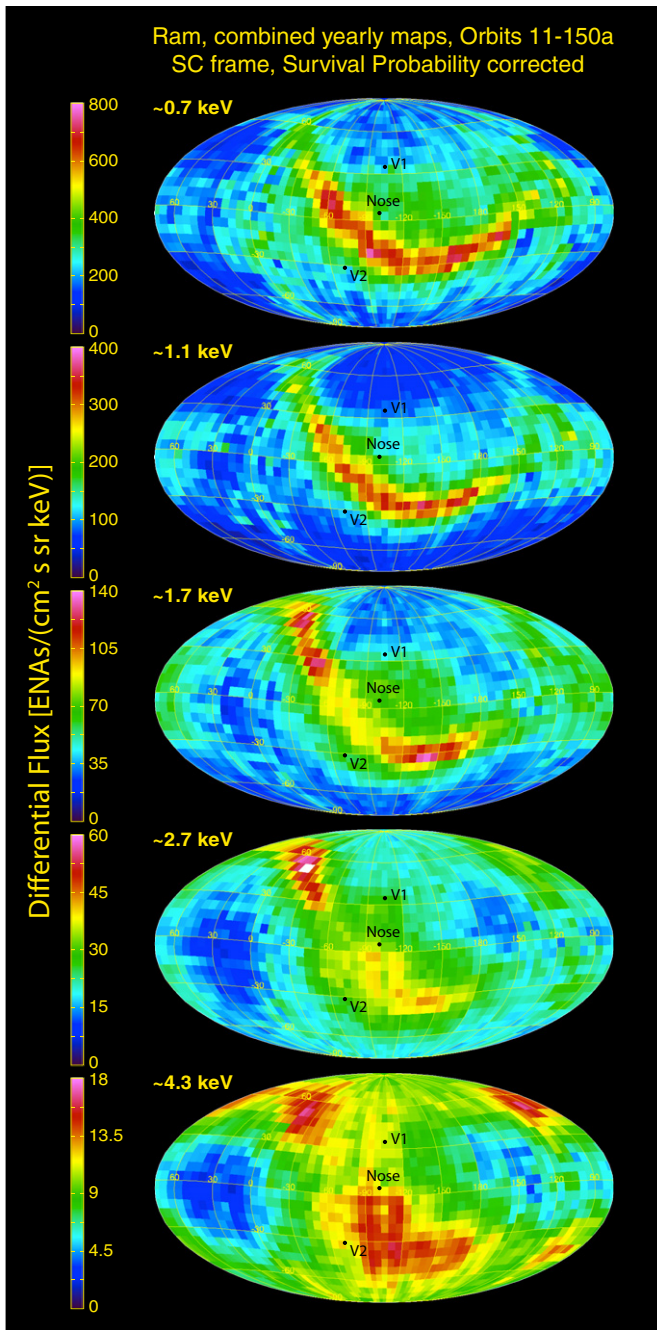
Figure 17. Ram-only maps at various energies, produced by statistically combining all three annual ram maps (Figure 15).

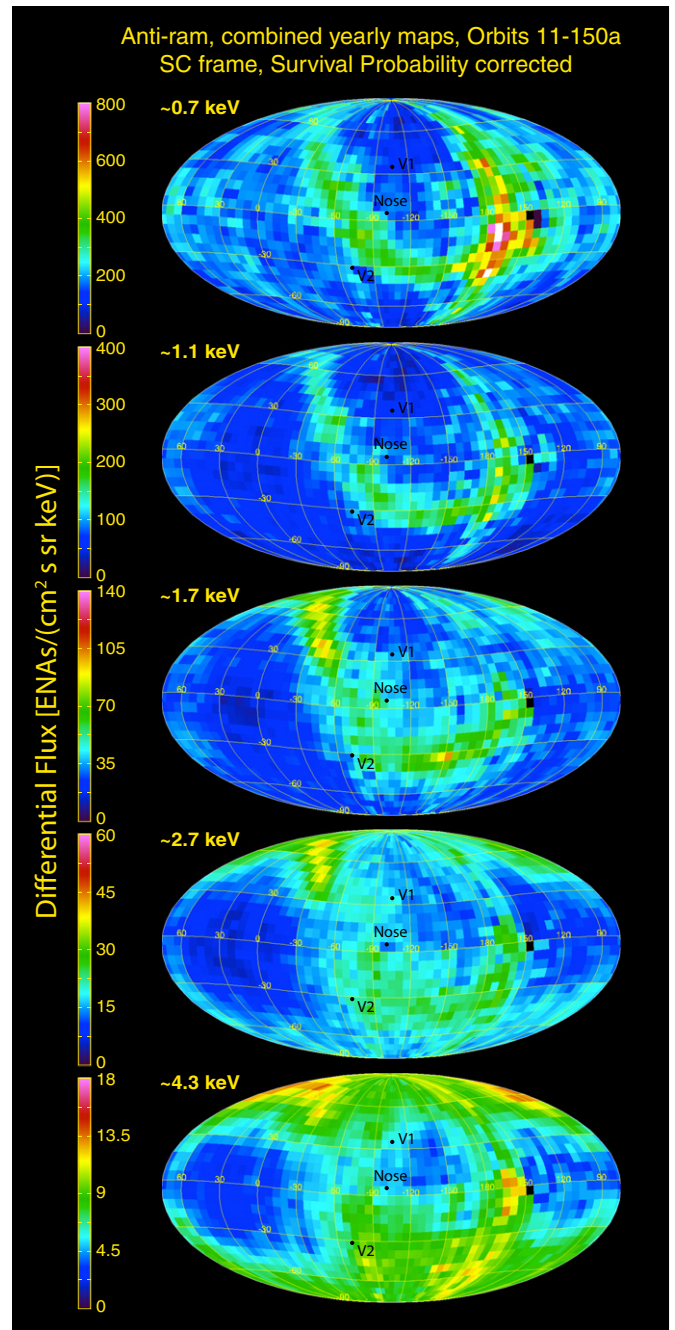(A color version of this figure is available in the online journal.)

Figure 18. Similar to Figure 17, but anti-ram only maps. Survival probability correction of statistically noisy data around the "hole" on the right side (especially at the lower energies) produces unphysically high fluxes which should be ignored.

(A color version of this figure is available in the online journal.)

times. Still, the solar wind energy has been generally decreasing for a decade or more (McComas et al. 2008), so it appears that a more complex explanation will be needed to account for ENA fluxes from the tail.

We also quantitatively examine the temporal variations of global ENA fluxes by comparing total fluxes separated by two years from Map 1 versus Map 5. We use maps in the spacecraft reference frame (not C-G corrected), but corrected for ENA survival probability. We then integrate exposure-weighted fluxes over the five *IBEX-Hi* energy ranges (0.5–6.0 keV). For this comparison, here we define polar regions as those with ecliptic latitude +48° to +90° and −48° to −90°, and a complementary ecliptic region from −48° to +48° in latitude.

The total flux (4π sr), fluxes from the ecliptic northern (2π sr) and southern (2π sr) hemispheres, and fluxes from the polar (1.3π sr) and ecliptic (2.7π sr) regions all decreased by 16%–20%, which is consistent with the earlier reported "dimming" of the heliosphere (McComas et al. 2010), and with the results in Table 4, since the majority of the ENA flux is in the lowest two energies. Over these two years, the north-to-south total flux ratios remained quite constant at 1.18 and 1.14 in Maps 1 and 5, respectively. The polar-to-ecliptic ratios are also stable at 0.37 and 0.35, respectively.
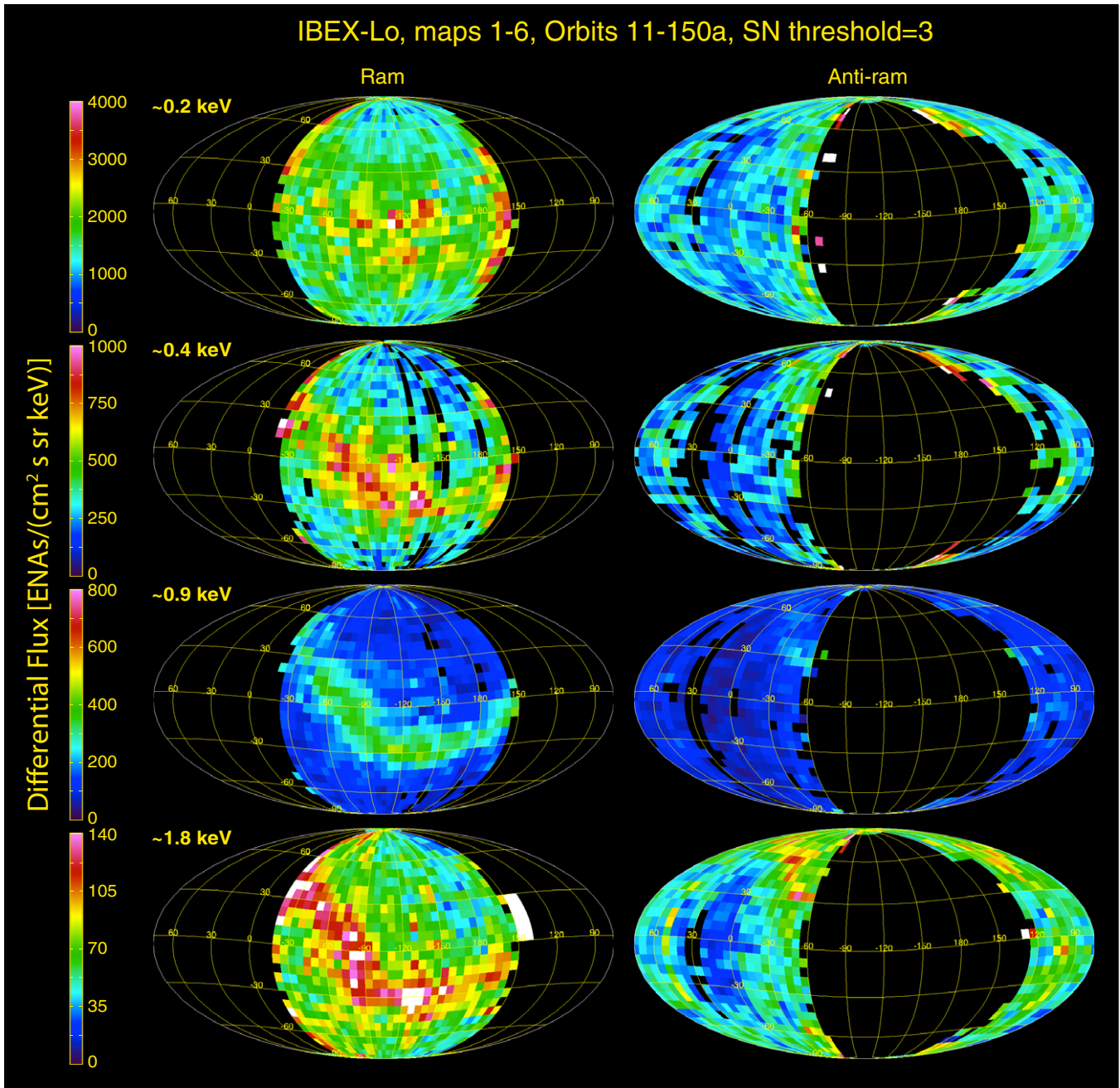
Figure 19. ENA sky maps based on *IBEX-Lo* observations for energy passbands around 0.2 keV (E5), 0.4 keV (E6), 0.8 keV (E7), and 1.8 keV (E8) for ram (left column) and anti-ram (right column) directed viewing. Data are only plotted for pixels with a signal-to-noise ratio >3. Note that color bars for the highest two energies match the similar energy bands for *IBEX-Hi*.

(A color version of this figure is available in the online journal.)

Table 4
Comparison of Survival Probability Corrected Fluxes between the 2009 and 2011 Annual Ram Sky Maps in the Spacecraft Frame

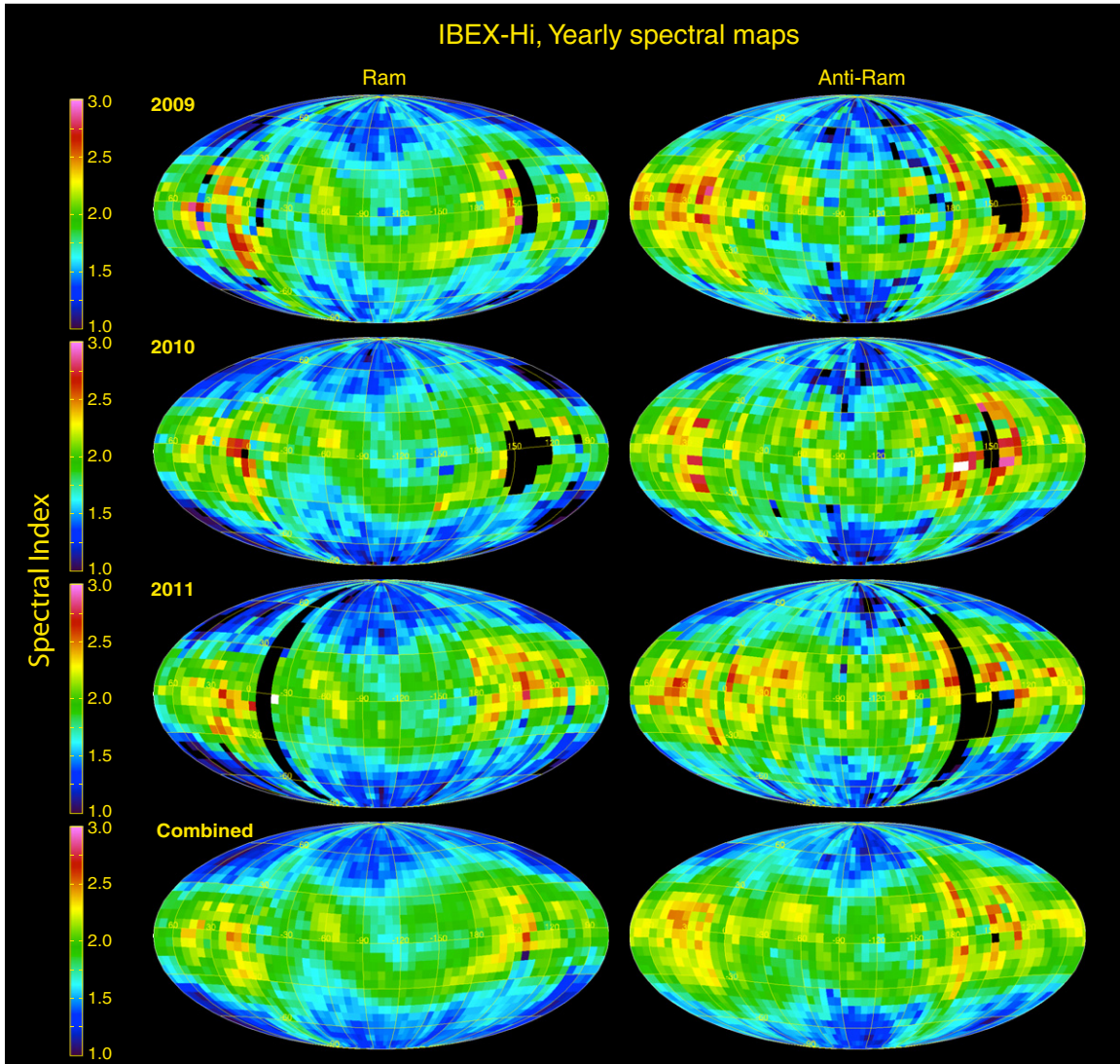| Energy	Ratio of Weighted Fluxes in Annual *IBEX* Ram Maps ($Flux_{2011}/Flux_{2009}$)				
(keV)	Region 1 Ribbon	Region 2 Nose/N Pole	Region 3 Flanks/S Pole	Region 4 Offset Tail	All Sky
~0.7	0.84 ± 0.01	0.91 ± 0.01	0.92 ± 0.01	1.19 ± 0.09	0.89 ± 0.01
~1.1	0.77 ± 0.01	0.76 ± 0.01	0.79 ± 0.01	0.84 ± 0.05	0.78 ± 0.01
~1.7	0.87 ± 0.01	0.81 ± 0.01	0.85 ± 0.01	1.01 ± 0.05	0.85 ± 0.01
~2.7	0.89 ± 0.01	0.90 ± 0.01	0.95 ± 0.01	1.06 ± 0.05	0.92 ± 0.01
~4.3	0.89 ± 0.01	0.88 ± 0.01	1.01 ± 0.01	1.13 ± 0.05	0.94 ± 0.01

Figure 20. Sky maps of energy spectral index in annual ram (left column) and anti-ram (right column) data sets, which are not corrected for survival probability. Data are corrected to the solar frame (not a full C-G correction—see the text). From top to bottom, the rows show the 2009–2011 annual maps and the statistically summed maps (bottom).

(A color version of this figure is available in the online journal.)

The properties of the interstellar wind and interstellar magnetic field are expected to be stable on timescales of at least decades. The only property that varies significantly over timescales as short as several years is the solar wind flow. A simple physical model based on ~1 keV solar wind ions and returning to the inner heliosphere as ENAs provides insight into the effect of solar wind variations on the global interaction. Let us assume that (1) it takes about one year for the solar wind to reach the ENA producing region beyond the termination shock, (2) the shocked solar wind plasma effectively produces ENAs for two years, and (3) it takes about one year for the ENAs to come back in 1 AU. The effective period of time for ENA production is constrained by shocked plasma depletion through charge exchange and by convection. Thus, this simple model assumes the solar wind properties averaged over the two year period from 2 to 4 years from the central times of the corresponding maps determine observed global ENA fluxes.

Figure 26 shows solar wind fluxes (from the combined OMNI data set) as a function of time from the central times of Maps 1, 3, 5 as well as for Maps 7 (currently being acquired) and

9 to be obtained from December 2012 to June 2013. Similar dependencies were obtained for the flux of the solar wind momentum and energy. While OMNI data correspond to the ecliptic solar wind, McComas et al. (2008) showed that the solar wind mass flux and momentum flux (energy) vary globally and the ecliptic values can be taken as good proxies for all latitudes.

Table 5 indicates decreases of the normalized (to Map 1) solar wind fluxes of mass, momentum, and energy by approximately 8% during the second year of observations (ratios of solar wind flows for Maps 1 and 3) and then about another 10% during the third year (Maps 3 and 5). The total fluxes of heliospheric ENAs (bottom line in Table 3) also drop by similar amounts. Therefore, averaged properties of the solar wind flow seem to have a simple first-order relationship in driving of the global interaction.

From our simple model, the solar wind momentum and energy fluxes should decrease significantly more than the solar wind mass flux during the corresponding time interval preceding Map 7. This difference reflects decrease of typical solar wind velocities below ~400 km s^{-1} during 2009 and the first half of
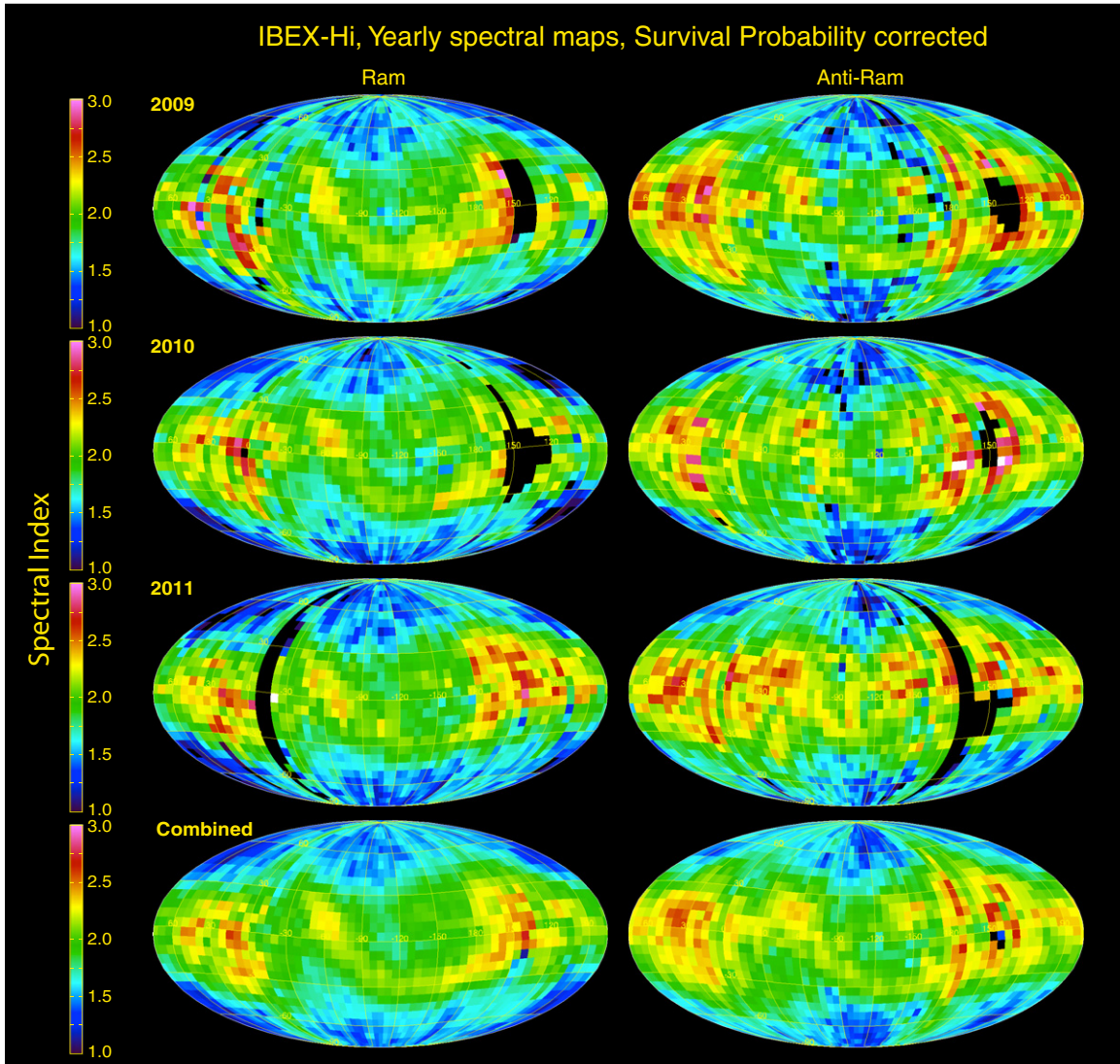
Figure 21 Same as Figure 20, but including corrections for the survival probabilities.
(A color version of this figure is available in the online journal.)

Table 5
Ratios for Averaged Ecliptic Solar Wind Properties for Time Intervals
of −4 to −2 years prior to corresponding *IBEX* Maps

ENA Maps	1	Map 3/1	Map 5/1	Map 7/1	Map 9/1
SW mass flux	1.0	0.92	0.82	0.77	0.80
SW momentum flux	1.0	0.92	0.81	0.70	0.71
SW energy flux	1.0	0.92	0.81	0.63	0.62
ENA flux (total)	1.0	0.91	0.84	(0.70)	(0.70)

Notes. The last row shows total fluxes of heliospheric ENAs and their predictions, within the simple modes of the solar wind driving the heliospheric interaction, for Maps 7 and 9. Predicted normalized ENA fluxes are in parenthesis.

2010, while the density remained relatively stable throughout 2008–2010. Consequently, if currently acquired Map 7 shows a smaller decrease in the total ENA fluxes, it could then suggest that the mass flux of the solar wind, rather than momentum or energy, is a stronger driver of the global heliospheric interaction.

If the total heliospheric flux of ENAs follows this simple dependence on the solar wind properties, then we can expect

that Map 7 would show a further drop, compared to the previous Map 5, and its total flux would be ∼70% of the flux in Map 1. The next Map 9 to be acquired in the first half of 2013 would then be similar to Map 7 with a similar total ENA flux constituting ∼70% of the flux obtained from Map 1. Of course, the simplistic approach here incorporates equally simplistic assumptions and slightly different assumptions could provide some other time delay (e.g., 3–5 years instead of 2–4 would indicate the leveling off of fluxes already in Map 7). In the end, full and detailed three-dimensional time-dependent modeling will be needed to produce accurate timing for all energies and establish quantitative causal relationships for the interaction. However, our simple model here provides some insight as well as identifies key signatures measured by *IBEX* to monitor and understand the physical processes that drive temporal change in the outer heliosphere.

Another interesting, if somewhat speculative, possible connection for the longevity of the Ribbon arises from observations reported from the Low Energy Neutral Atom (LENA) imager (Moore et al. 2000) on the IMAGE spacecraft. LENA was designed to detect magnetospheric low-energy neutrals primarily in the energy range from 10 to 300 eV, but had some response to
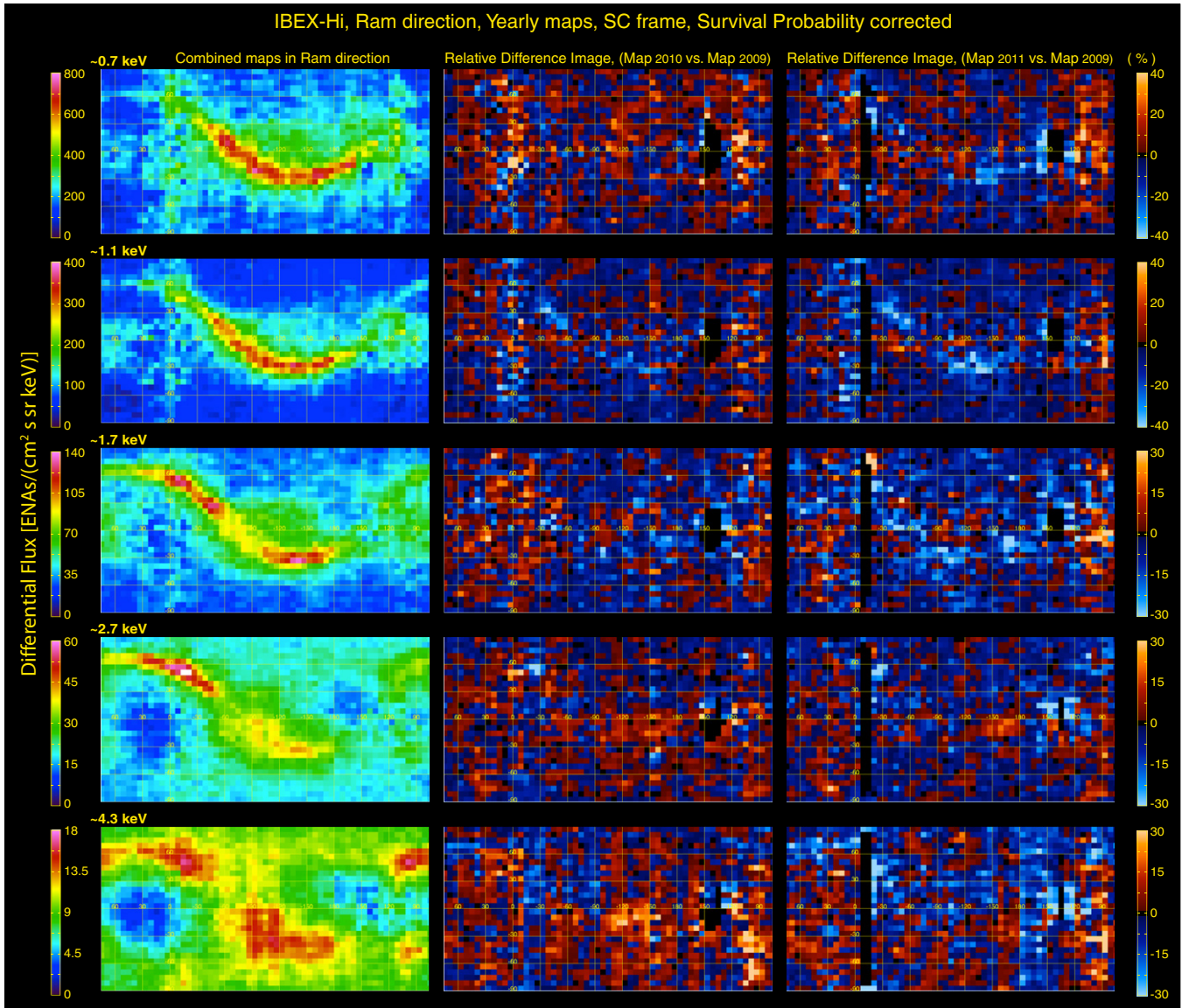
Figure 22. Time variations in the ram ENA maps including all corrections except for C-G. The left column shows the average ENA fluxes (as in Figure 17) for reference; the second and third columns give color-coded representations of the percentage increase (red) or decrease (blue) from 2009 to 2010 (middle column) and 2009 to 2011 (right column). In each of these, the percentage change is calculated on a pixel-by-pixel basis as the new value minus the old value divided by 100× the old value.

(A color version of this figure is available in the online journal.)

neutrals as high as ∼1 keV. Based on its primary energy range, LENA was expected to detect interstellar neutral helium arriving from the upstream direction of the inflowing interstellar gas. Instead, it primarily observed an inexplicable, broad enhancement of ENAs that was postulated to come from ∼30° away from the nominal interstellar neutral helium direction (i.e., at approximately 75° ecliptic longitude; Collier et al. 2004). This broad enhancement was seen in the same location in several years during the IMAGE mission lifetime (up to 2005). These observations led to speculation that there was a secondary stream of neutrals with energies of ∼1 keV arriving from −75° ecliptic longitude (Collier et al. 2004; Wurz et al. 2004). The −75° ecliptic longitude arrival direction for ∼1 keV neutrals very roughly coincides with the ecliptic plane crossing of the *IBEX* Ribbon, so these observations might indicate an equatorial crossing of the Ribbon in a similar location in 2001–2002 to where it is now. However, the LENA observations have been interpreted

in multiple ways, including the possibility that IMAGE/LENA did not see ∼1 keV neutrals from −75° ecliptic longitude because these neutrals are essentially undeflected by the Sun's gravitational field and were outside of the LENA field of view (Fuselier et al. 2009c). Thus, at this juncture, possible IMAGE/LENA observations of the ecliptic plane crossing of the Ribbon in 2001–2005 could well be an unexplained coincidence.

Finally, to complete our exploration of possible time variations in this study, we compare the separate 2009–2011 spectral maps from Figures 20 and 21. Inspection of these yearly ram and anti-ram maps of the ENA spectral slopes show some level of variability, but little clear evolution over these three years for the Ribbon or any other portion of the sky. Figures 27 and 28 quantify these spectral changes as percentage differences from 2009 as was done in Figures 22 and 23 for the fluxes. Because of the relatively small changes in fluxes, it is perhaps not surprising that the spectral slopes should be quite consistent.
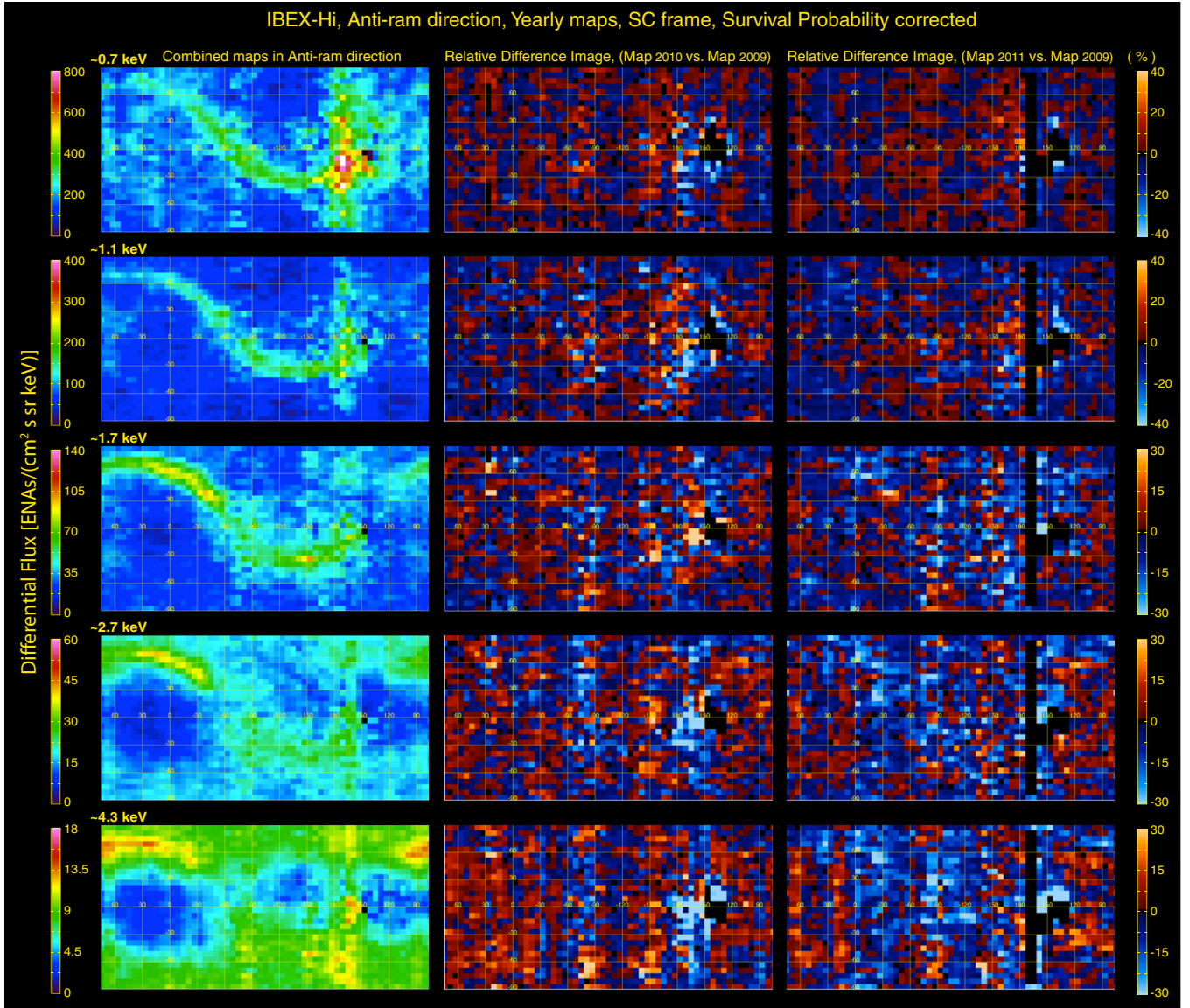
Figure 23. Similar to Figure 22, but for anti-ram maps from 2009, 2010, and 2011.
(A color version of this figure is available in the online journal.)

Thus, while there might be some small variations over 2009–2011, the spectral slopes of the ENA emissions observed by *IBEX* were generally quite stable over the three years examined here.

4. IMPLICATION FOR THE SOURCE OF THE *IBEX* RIBBON

With the combined statistics of the first three years of *IBEX* observations as well as rigorous validation of the data and processing of the data informed by these observations, a critical feature emerges: the latitude dependence of the dominant energy emissions in the Ribbon. Figure 29 shows Ribbon fluxes from the combined ram maps, but oriented with the Ribbon symmetry direction (likely external magnetic field direction) in the center of the Mollweide projection as shown first by Funsten et al. (2009a). These maps most clearly demonstrate the evolution of the Ribbon structure as a function of ENA energy: (1) at ~0.7 keV the Ribbon is brightest where it crosses closest to the nose or upwind direction and extends away from there,

dropping off in both directions, (2) at ~1.1 keV the Ribbon is narrowest, but is slightly weaker where it crosses the ecliptic equator and extends to slightly higher latitudes in the north, (3) at ~1.7 keV, the Ribbon is significantly weaker around the equator and brighter in both the southern (−30° ecliptic latitude) and northern (above +20° ecliptic latitude) regions, (4) by ~2.7 keV, bright emissions are still ordered along generally the same curve as the Ribbon at lower energies, but the bright emissions occur predominantly at high latitudes in the north, with some emission across the southern portion (the Ribbon does not go to high latitudes in the south), and finally (5) at ~4.3 keV, the Ribbon feature has been replaced by two broad regions of enhanced emissions roughly (but not precisely) aligned with the Ribbon. The northern region appears to still be basically Ribbon-like and now extends all the way around the pole; however, the region south of the nose is broader and may well be largely associated with some other source of higher energy ENAs from near the nose.

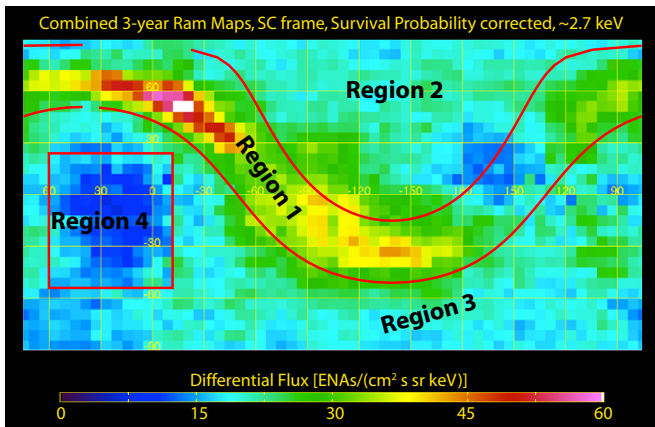The Ribbon appears most obviously at ~0.7 and 1.1 keV energies predominantly at low latitudes. In contrast, the higher

Figure 24. Combined three-year ram map at 2.7 keV overlaid with lines identifying four regions in the sky maps: (1) the Ribbon, (2) nose and north pole on the upwind side, (3) flanks and south pole, and (4) offset heliotail, intermediate between the downwind flow and field directions (Schwadron et al. 2011).

(A color version of this figure is available in the online journal.)

combined Maps 1 and 2 set after separation of the Ribbon from the globally distributed flux. Here we show and expand upon this effect with the much better statistics of three years of combined observations. While dimmer away from the peak energy, the low-latitude region of the Ribbon also appears to broaden in the bottom step of *IBEX-Hi* data and in the lower energy *IBEX-Lo* data, all the way down to ∼0.2 keV. The broadening at higher energies may also be consistent with a broader "belt" of ENA emissions at higher ENA energies (10s keV) reported by Krimigis et al. (2009); however, it is important to note that the published direction of symmetry for the belt is offset by ∼30° from the Ribbon (as identified in the 1 keV maps). Thus, another observational aspect of the data that the correct model of the Ribbon needs to explain is a broadening of the ENA emission regions at both higher and lower energies than the main emissions.

While all six explanations for the Ribbon first proposed by McComas et al. (2009b) and further explored by McComas et al. (2010) and Schwadron et al. (2011) rely on the solar wind as the ultimate source of the Ribbon ENAs, most of them require significant processing of the solar wind plasma and pickup ions through the termination shock and heliosheath. Since the initial publication of the *IBEX* results and first six possible Ribbon explanations, other ideas have been proposed to explain the Ribbon. Several of these build on the initial ideas, but expand on the processing of solar wind, pickup ions, and cosmic rays at the termination shock or heliopause (Fahr et al. 2011; Siewert et al. 2012). Others propose a vastly different solution with a source in the very local interstellar medium, outside the heliosphere (Grzedzielski et al. 2010). While such a source is conceivable, the combination of the short timescale variations in ENA flux and the latitude dependence of Ribbon energy suggest a heliospheric rather than extra-heliospheric source for the Ribbon.

The explanation that provides much more direct coupling to the pre-termination shock solar wind is some sort of secondary ENA source, where solar wind (and inner heliosheath) ions
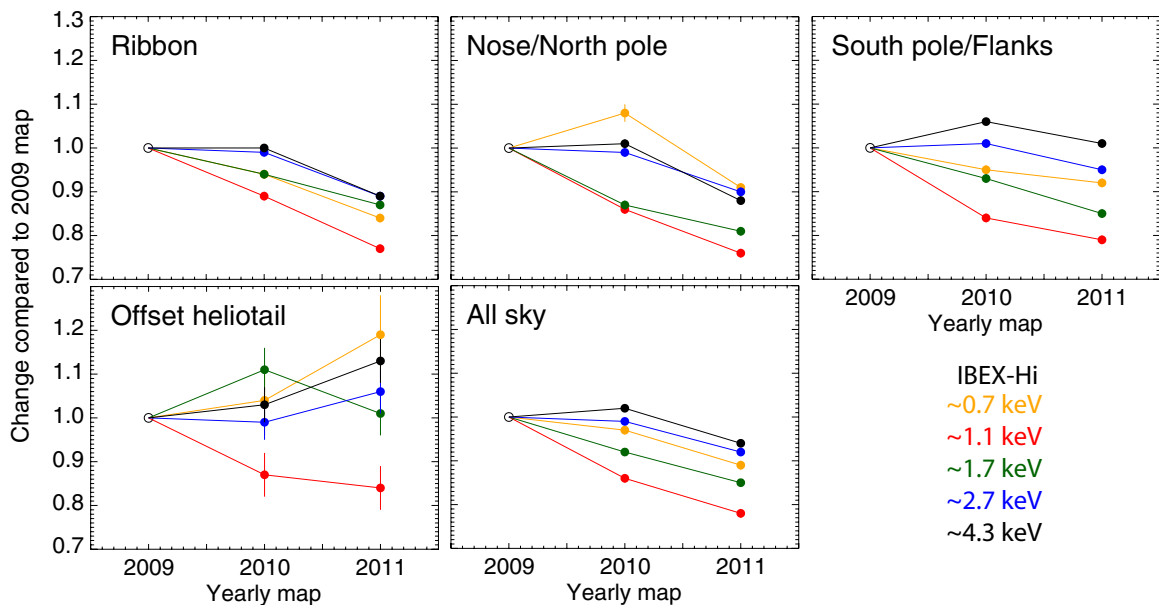
energy extension of the Ribbon (at ∼2.7 and ∼4.3 keV) appears primarily at high latitudes. This is particularly significant because, for the solar minimum conditions that apply for these observations, the low-latitude solar wind protons average ∼400 km s^{-1} (∼0.8 keV for protons), while at high latitudes, the solar wind is less variable and averages ∼760 km s^{-1} (∼3 keV protons; see Sokół et al. 2012). Clearly this connection between latitude and energy of the Ribbon emissions suggests a fairly direct solar wind source of the Ribbon ENAs.

A second element that becomes clearer in the three-year combined maps is an apparent broadening of the low-latitude portions of the Ribbon at higher and lower energies away from its prime energy (∼1 keV at these latitudes). Broadening at energies above this for the low-latitude parts of the Ribbon was documented by Schwadron et al. (2011) using C-G corrected,

Figure 25. Time variation of ENA fluxes between the 2009, 2010, and 2011 maps summed over the five regions identified in Figure 24. The colors represent ENA energy bands of ∼0.7 keV (orange), ∼1.1 keV (red), ∼1.7 keV (green), ∼2.7 keV (blue), and ∼4.3 keV (black)—see Table 1. Statistical error bars are included, although they are very small for all regions other than the tail.

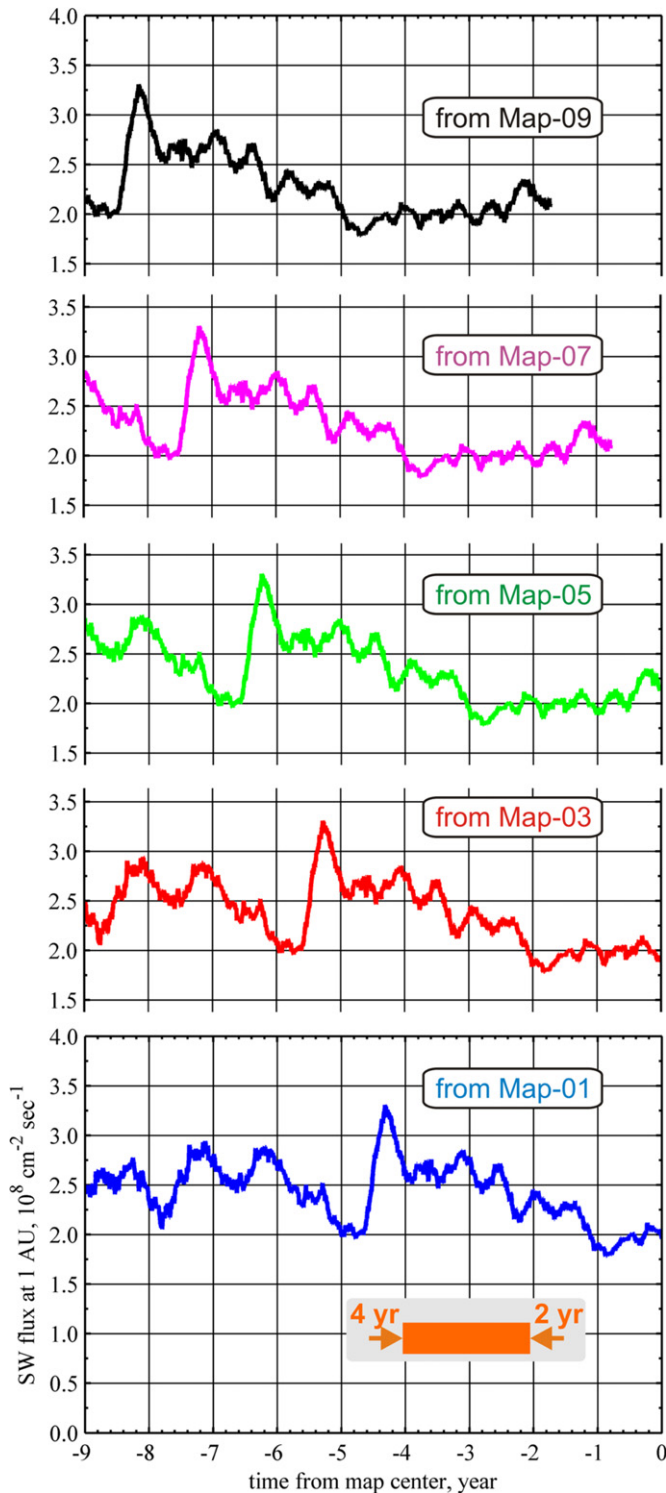(A color version of this figure is available in the online journal.)

Figure 26. Solar wind flux from the OMNI data set averaged over 108 days as a function of time from the centers of *IBEX* Maps 1, 3, 5, 7, and 9. For each map we consider solar wind during time intervals extending from 2 to 4 years prior to the center of the corresponding map.

(A color version of this figure is available in the online journal.)

Two subsequent studies (Heerikhuisen et al. 2010; Chalov et al. 2010) used global MHD models to quantitatively reproduce a Ribbon with realistic fluxes and width at 1 keV by assuming that the solar wind ions picked up in the outer heliosheath retain a partial ring distribution (a free parameter in their models) for the ~2 years required for a typical ion-to-charge exchange again and become a secondary ENA.

Unfortunately, for this simple version of a secondary ENA source for the Ribbon, the time scale to re-neutralize ionized ENAs to produce secondary ENAs is about two years—several decades longer than generally expected pitch angle scattering timescales in the outer heliosheath (McComas et al. 2009b). In support of this statement, Florinski et al. (2010) combined linear kinetic theory and hybrid simulations to assess the stability of the pickup ion ring distribution. These authors found that instability-generated waves in the outer heliosphere efficiently scatter the ions and break down the ring distribution on timescales several orders of magnitude shorter than the time required for re-neutralization. Gamayunov et al. (2010) suggested one possible solution to this breakdown. These authors suggested that a combination of large-scale interstellar turbulence and small-scale (~10^{-5} to 10^{-4} AU) turbulence generated by the unstable pitch angle distributions of the pickup ions may be able to make these distributions marginally stable and produce a narrow Ribbon from a small part of the proton phase-space distribution function that can resonate with the locally generated ion cyclotron turbulence. While possible, this explanation invokes a highly speculative plasma process in the outer heliosphere to effectively quench the pitch angle scattering; such scattering is highly efficient essentially everywhere else pickup ion distributions are directly observed in the heliosphere.

If pickup ion partial ring distributions can somehow survive long enough in the outer heliosheath or if there is (1) some other process to enhance the ion density where the magnetic field is perpendicular to *IBEX*'s (radial) line of sight or (2) to push isotropic pitch angles toward being more perpendicular, then a secondary ENA process very naturally would produce dominant Ribbon fluxes at the latitude-dependent solar wind energy, i.e., ~0.8 keV at low latitudes and ~3 keV at high latitudes around solar minimum. Such a source also naturally accounts for decreasing fluxes of ENAs in the Ribbon owing to the generally decreasing solar wind density and pressure of the last decade (McComas et al. 2008). In addition, it is interesting that the small increase in solar wind speed in the fast high-latitude solar wind of ~1 km s^{-1} deg^{-1} of increasing heliolatitude (McComas et al. 2000) may even appear in the *IBEX* ENAs with the highest energy band showing a more complete Ribbon at the highest latitudes around the north pole compared to the next lower energy.

Figure 30 provides a visual summary of this process and its latitude dependence around solar minimum (see Section 5 for a prediction at solar maximum). While the jury is still out on the viability of a secondary ENA Ribbon source, several lines of observational evidence, shown in this study, point to some sort of (possibly modified) secondary ENA source from the neutral solar wind as the most likely explanation. The *IBEX* observations provide the global understanding of the heliosphere's interstellar interaction, but cannot directly observe the local microphysics underlying the detailed plasma distributions and dynamics that effect the ENA emissions. If secondary ENAs are the source of the Ribbon, there must be some "missing physics" in our current understanding that will naturally explain the ribbon structure.

become neutralized, travel outward past the heliopause into the outer heliosheath, become ionized and picked up on the draped interstellar magnetic field in the outer heliosheath, and after some time, some become re-neutralized and emitted as ENAs back in toward the inner heliosphere (McComas et al. 2009b).
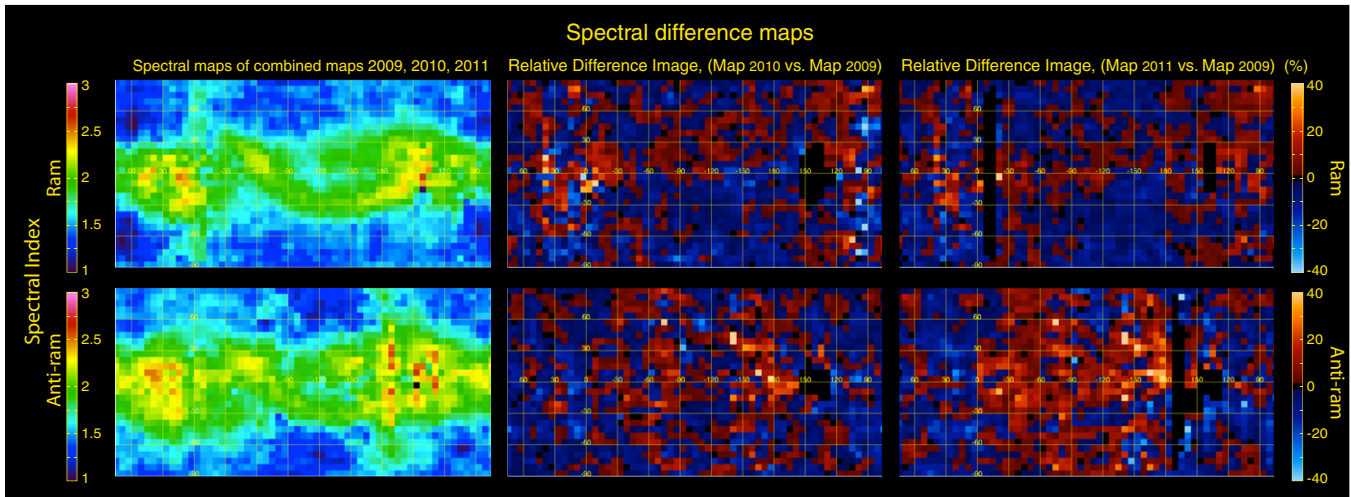
Figure 27. Spectral indices for the combined ram (top) and anti-ram (bottom) maps (left column) and percentage change in these indices from 2009 to 2010 (middle) and 2009 to 2011 (right).

(A color version of this figure is available in the online journal.)
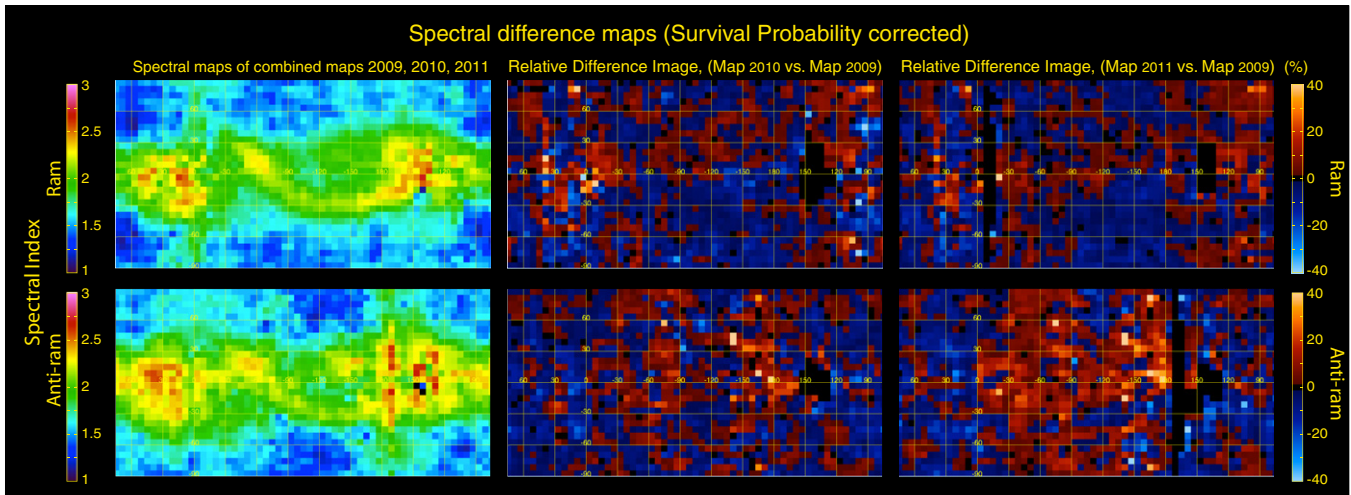

Figure 28. Similar to Figure 27, but including survival probabilities.

(A color version of this figure is available in the online journal.)

5. PREDICTION AND POSTSCRIPT

If correct, a secondary ENA Ribbon source provides a clear prediction for solar maximum, where the solar wind speed is no longer well organized by heliolatitude (e.g., McComas et al. 2003). That is, the Ribbon should be seen dominantly at low-to-intermediate energy at all heliolatitudes (and may well be broader in energy) as both fast and slow solar wind flows are mixed at all heliolatitudes around solar maximum. We are still likely ∼2 years from solar maximum and as mentioned above, it takes several years for ENAs produced in the solar wind to be "processed" as secondary ENAs. Thus, we are still many years from the peak of observing ENA signatures for solar maximum conditions. Observations from half to a full decade from now will only be possible if *IBEX* continues to be healthy in a very long extended mission and/or if there is a follow-on mission, such as the Interstellar Mapping mission suggested by McComas et al. (2011b). Such a mission would both provide these critical observations at significantly higher resolution and sensitivity as well as deliver on a much broader

range of inner and outer heliospheric science. Prior to that, continued observations of variations in the Ribbon fluxes should continue to foretell aspects of the evolving outer heliosphere and give tantalizing glimpses of the real source of the *IBEX* Ribbon and its underlying physics.
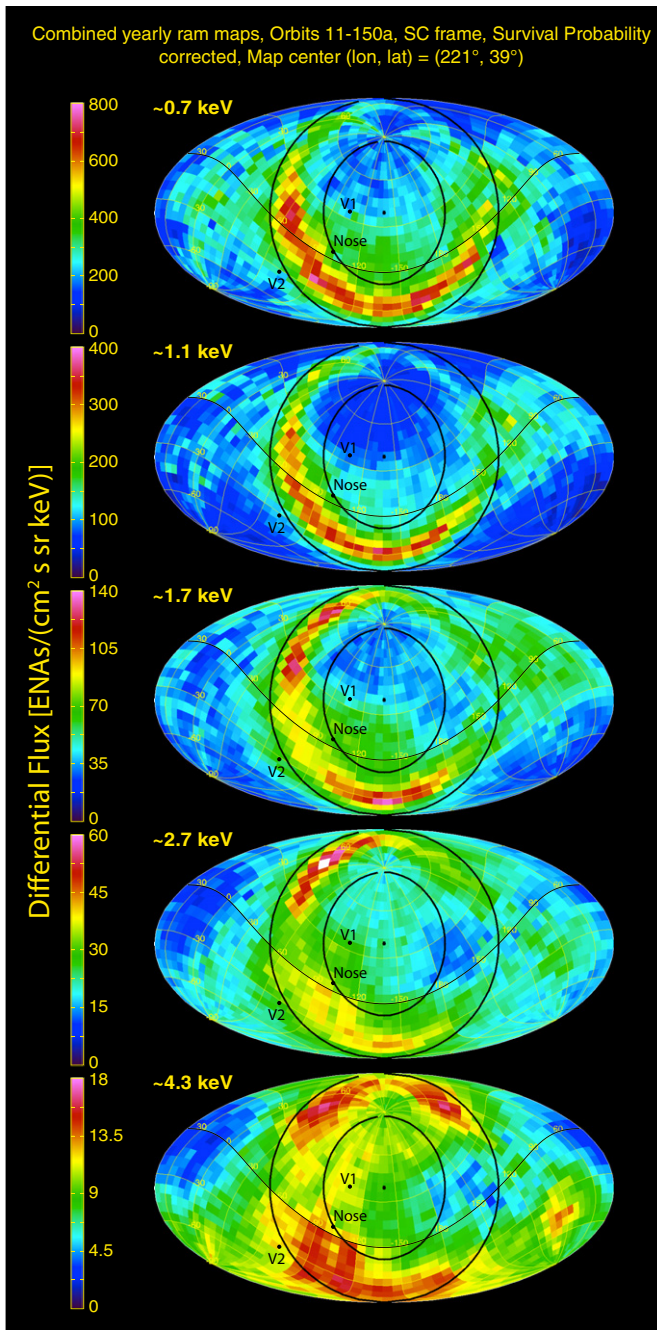
Figure 29. Survival probability corrected ram maps in a Mollweide projection centered on the symmetry direction. The ecliptic is identified by the black line, while circles bracket the Ribbon to help guide the eye.

(A color version of this figure is available in the online journal.)

APPENDIX A

COSMIC RAY BACKGROUND AND STABILITY
OF THE *IBEX-Hi* DETECTOR OVER TIME

Accurate removal of backgrounds and accurate characterization of any trends over time in *IBEX-Hi*'s detection efficiency are both vital to analysis of time evolution of the heliospheric ENA signal. The chief background, always present, is from penetrating radiation. During times of "clean" heliospheric viewing, cosmic rays provide the only penetrating background. By using coincidence and qualification event information inherent in the detailed *IBEX-Hi* measurements, we are able to quantify and

remove the absolute contribution of penetrating radiation over time. In addition, coincidence information provided by the detector section allows precise trending of the detection efficiency of ENAs over time.

The *IBEX-Hi* detector section consists of three consecutive channel electron multipliers (CEMs) (A, B, and C) collecting electrons from three sequential detector volumes that are separated by ultrathin carbon foils (Funsten et al. 2009b). An ENA which has been ionized on the entrance conversion foil and transited the ESA will then pass through the foils, producing electrons, which are collected by the CEMs. A triple coincidence event is one in which electrons are detected in all three CEMs within a 96 ns ("long") window; a qualified triple coincidence event, or qABC, is a triple coincidence where electrons are not detected in CEM C—that is to say, the back of the detector—until at least 3 ns after they are first detected in CEM A or B, at the front of the detector. Unqualified triples, or unqABC events, are triple coincidences, where CEM C triggers before or within 3 ns (the "short" window) of the first of CEMs A and B.

Cosmic rays produce electrons essentially simultaneously throughout the various surfaces of the detector, on the walls, and on the nickel grids, which support the carbon foils. Ideally, any triple event produced by cosmic rays would be classified as a unqABC event, due to the subnanosecond transit time of cosmic rays. However, variation in the electron transit times from various parts of the detector foils and walls to the CEMs is not short compared to the short qualification window, and many of these events appear as qABC.

The enhancement in the qABC rate due to gamma radiation was measured prior to launch, during *IBEX-Hi* testing and calibration, and the appropriate removal technique is outlined in Wurz et al. (2009). The ratio of unqABC/qABC is different for ENAs ($\eta \sim 1$:99, depending on the velocity of the incident ENA) than for cosmic radiation ($\xi \sim 9$:10 as measured during on-orbit testing). Consequently, by comparing qABC and unqABC rates, the qABC count rate due to ENAs can be separated from the qABC count rate due to penetrating radiation. In particular, if over some interval of time N_q qABC counts and N_u unqABC counts are observed, the number of qABC counts attributable to cosmic radiation rather than to ENAs is $(N_u - \eta N_q)/(\xi - \eta)$.

The unqABC/qABC ratio for cosmic radiation was determined by on-orbit tests in Orbits 13 and 77, during which the voltages of the ESA were set to prevent any charged particles, either from the space environment or generated by ENAs, from getting to the detector. The uncertainty in the ratio comes from the counting statistics of the tests and is about 3%. The unqABC/qABC ratio for ENAs is different for each energy setting of *IBEX-Hi*, and depends weakly on the energy spectrum of incoming ENAs. This is true because slower-moving ENAs produce relatively more qualified and fewer unqualified triples. The ratios for each of the six ESA settings were determined by requiring the calculated penetrating background rate for all moderately quiet intervals of Orbits 16–122 be independent of ENA flux. The ratios obtained this way for ENAs are consistent with those determined during calibration, but are considerably more precise.

The penetrating background rates determined this way, which do not include solar energetic particle (SEP) event intervals, corresponds extremely well with cosmic ray monitors. The top panel of Figure 31 shows an orbit-by-orbit comparison of *IBEX-Hi* penetrating background rate to CRaTER/LRO dose (Spence et al. 2010), with intervals of enhanced solar particles removed. Similarly, the bottom panel of Figure 31 shows a
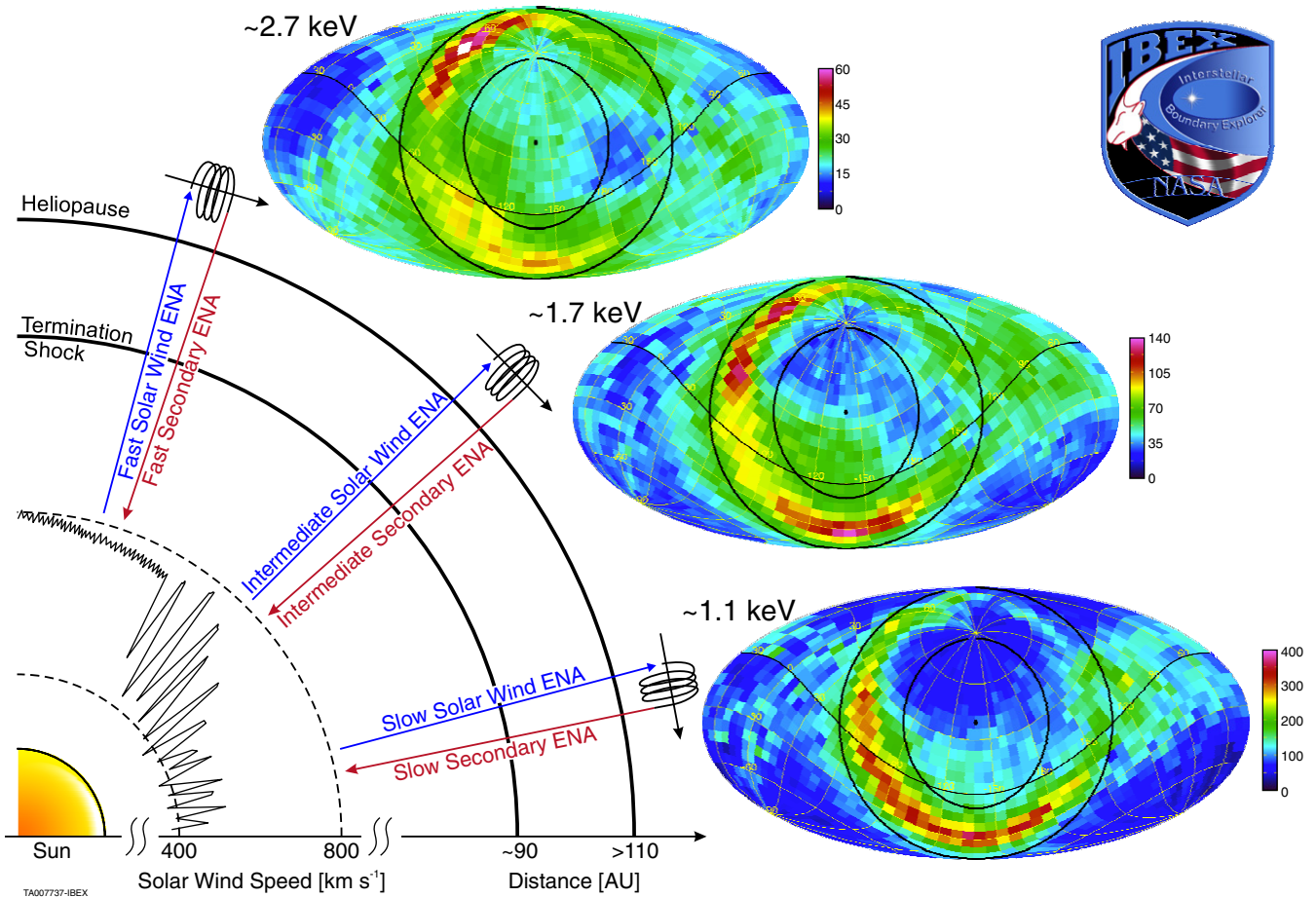
Figure 30. Schematic diagram of (1) typical solar wind speeds as a function of heliolatitude around solar minimum as observed by *Ulysses* (McComas et al. 1998, 2000) and (2) the secondary ENA generation mechanism as depicted in McComas et al. (2010). Because of the tilt of the global solar magnetic field, fast and slow solar wind parcels interact at mid-latitudes in the inner heliosphere and produce intermediate-speed solar wind. The three Mollweide projections show *IBEX* ENA data from Figure 29 in differential flux units (cm^2 s sr keV)$^{-1}$. Together these elements show how slow solar wind ($\sim$400 km s^{-1}) generates low-energy ($\sim$0.8 keV) secondary ENAs observed primarily at low latitudes, intermediate-speed solar wind generates intermediate-energy secondary ENAs observed most strongly at mid-latitudes, and high-speed solar wind ($\sim$760 km s^{-1}) generates high-energy ($\sim$3 keV) secondary ENA observed primarily at high latitudes.
(A color version of this figure is available in the online journal.)

comparison to McMurdo neutron monitor data; note that in this case, in order to achieve agreement, the neutron monitor data had to be offset in addition to being scaled, due to the atmospheric cutoff around 700 MeV. In both cases the error bars shown for *IBEX* include both statistical and systematic uncertainties arising from the uncertainty in the unqABC/qABC ratios for ENAs and for penetrating background.

In summary, *IBEX-Hi* measures a background due to cosmic rays, which is accurately characterized by coincidence ratios in the detector section. After the correction is made to remove this background from the *IBEX-Hi* ENA signal, the heliospheric ENA flux is more accurately determined.

A second critical area for providing accurate ENA fluxes and determining if they have changed over time is the overall *IBEX-Hi* detection efficiency. We monitor the *IBEX-Hi*'s ENA detection efficiency over time in two ways. First, periodic gain tests, roughly every six months, find no apparent difference in behavior between the three CEMs. Overall, there has been a minor shift of only $\sim$60 V on the location of the edge of the gain plateau relative to operating voltage, which has been held constant. Since the total count rates in the *IBEX-Hi* detector tend to be below 10 s^{-1} per CEM, and negligible charge has been extracted from them so far in the mission, all

three CEMs remain in saturation and well up on their gain cure plateaus.

A more precise check of the entire detector section is made possible by comparing coincidence rates supplied by the spacecraft (Funsten et al. 2005). If the detection efficiency of sections A, B, and C of the *IBEX-Hi* detector are ε_A, ε_B, and ε_C respectively, then N incident ENAs will produce $N_{ABC} = N \varepsilon_A \varepsilon_B \varepsilon_C$ triple counts, qualified or unqualified. Similarly, the number of times both CEM B and CEM C will register an event, regardless of whether or not CEM A does, is $N_{BC} = N \varepsilon_B \varepsilon_C$. The efficiency of the first section of the detector is then simply $\varepsilon_A = N_{ABC}/N_{BC}$. Similar derivations supply ε_B and ε_C. These three efficiencies can thus be calculated per orbit and tracked over time. ε_A, ε_B, and ε_C constitute monitors not just of the three CEMs but of the entire detector section, including, for instance, the secondary electron emission properties of the ultrathin carbon foils.

The derivation of efficiencies is exact in the absence of signals other than that produced by a spatially uniform H ENA flux with a time-independent energy spectrum entering *IBEX-Hi*. In practice, we limit data used to trend efficiency to the cleanest data with the lowest backgrounds, selected for heliospheric analysis in energy steps 2–6, and subtract the penetrating
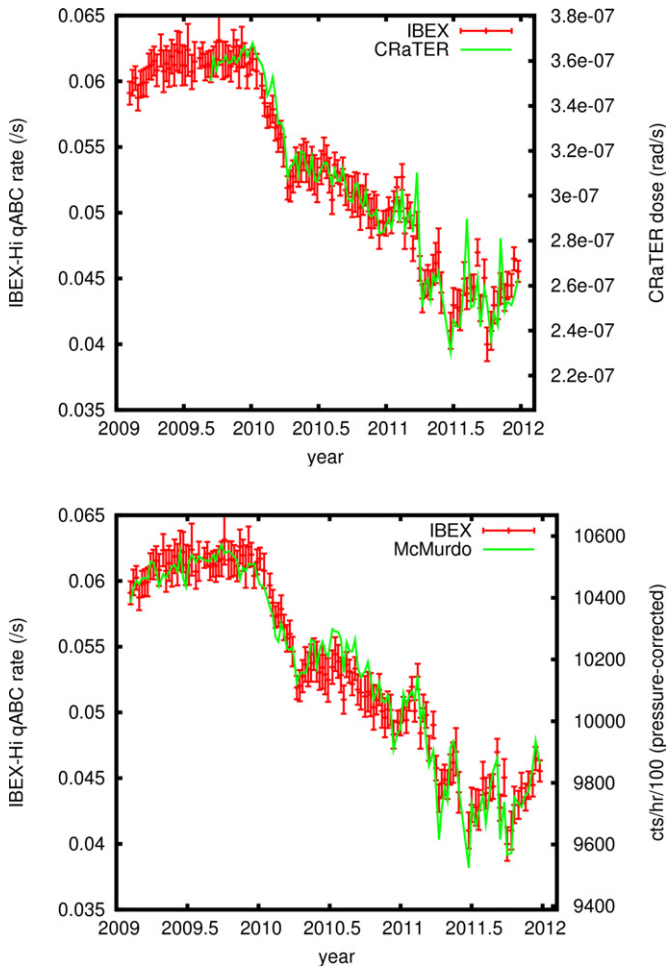
Figure 31. Penetrating background rate for qualified triples, calculated orbit-by-orbit excluding SEP events, compared to (top) CRaTER/LRO radiation dose and (bottom) McMurdo neutron monitor rates.

(A color version of this figure is available in the online journal.)

background contribution to the doubles rates (N_{AB}, N_{AC}, and N_{BC}) and triples rate (N_{ABC}), using the previous calculation of triples background rates and scaling by the ratios of coincidence events observed in the background tests of Orbits 13 and 77 (see above).

Penetrating radiation along trajectories not possible by real ENA-produced particles generate additional single and double coincidence events beyond those that can produce triple co-incidences. Thus, the fraction of observed double coincidence events due to cosmic radiation is considerably higher compared to their triples than for ENAs. Uncertainty in the penetrating background ratios N_{AB}, N_{AC}, N_{BC}/N_{ABC}, resulting in uncertainty in the background subtraction of the doubles, is the limiting factor in determining the absolute value of ε_A, ε_B, and ε_C. However, this systematic uncertainty does not prevent quite precise trending of any changes in efficiency, as long as the penetrating background ratios do not change over time. If there were any indication of this, we would need to run another on-orbit background test.

A complication arises with AB coincidences. Heavy species, such as oxygen, generate measurable AB coincidences, but rarely generate triples (or any other count involving CEM C), owing to their difficulty in penetrating even ultrathin carbon foils (e.g., McComas et al. 2004, and references therein). One source of oxygen is water in the *IBEX-Hi* collimator, which can ionize and become accelerated into the conversion foil at the entrance of the ESA, where it dissociates (Wurz et al 2009). Currently, we do not correct for heavy ion contamination from AB counts, and so the efficiency of CEM C, $\varepsilon_C = N_{ABC}/N_{AB}$, cannot be calculated nearly as accurately as ε_A and ε_B. One motivation behind examining the three detector sections individually and not simply monitoring the overall triples detector section efficiency, $\varepsilon = \varepsilon_A \varepsilon_B \varepsilon_C$, is that ε_A and ε_B are unaffected by this issue.

IBEX-Hi detection efficiency depends slightly on the initial energy of the ENA; thus, the efficiency reported depends weakly on the energy spectrum of the ENA signal. Figure 32 shows the orbit-by-orbit calculated detection efficiencies of the three sections of the *IBEX-Hi* detector, along with the linear trend. ε_C shows clear seasonal variation due to contamination in the AB coincidences, which reduce ε_C from its true value. Ground calibration could not directly produce values of ε_A, ε_B, and ε_C to correspond to the not-yet-observed heliospheric ENA energy spectrum, but the closest values are approximately 0.30, 0.78, and 0.49 respectively. Least-squares fits indicate ε_B and ε_C are consistent with no change from 2009 to 2012 at 1σ: the possible changes are 0.005 ± 0.005 and -0.004 ± 0.02, respectively. ε_A has increased, according to this analysis, by approximately
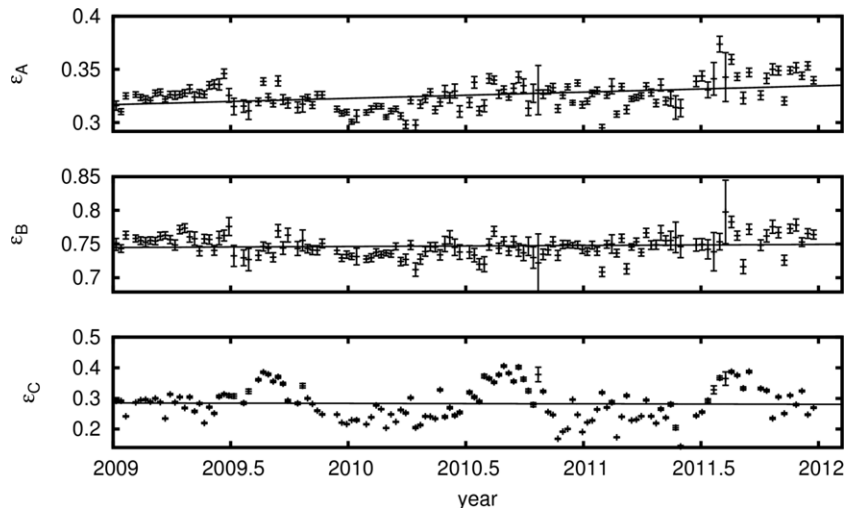

Figure 32. Detection efficiency of the three sections of the *IBEX-Hi* detector, as determined for each orbit from double and triple coincidence count ratios. Error bars shown are from counting statistics only. ε_C shows yearly variation due to contamination in the AB coincidences. Lines shown are from a linear regression of the data.

0.02 ± 0.004 over this time. Altogether, there has been essentially no change in efficiency in *IBEX-Hi* on orbit and the general observed temporal variations reported in this study are real.

APPENDIX B

SURVIVAL PROBABILITIES OF H ENAs IN THE SUPERSONIC SOLAR WIND REGION

B.1. Calculation of Survival Probabilities of Individual ENAs

Theoretical aspects of the survival probabilities of ENAs in the heliosphere, both in general and in the context of *IBEX* observations, were extensively discussed by Bzowski (2008) and Bzowski & Tarnopolski (2006).

The survival probability of an ENA is calculated by integrating the ionization rate $\beta(t)$ (i.e., the ionization probability per unit time) over the duration of the ENA exposure to ionizing factors during its travel from the origin at a time t_{start} down to the detector at a time t_{stop}:

$$ w_{\text{sur}} = \exp\left[-\int_{t_{\text{start}}}^{t_{\text{stop}}} \beta(t)\,dt \right] \qquad (B1) $$

The total ionization rate is calculated as a sum of the ionization rates due to all relevant ionization processes. These were recently reviewed by Bzowski et al. (2012b). The ionization processes of *IBEX* H ENAs include charge exchange between the H ENA and solar wind ions (mostly protons), and photoionization by solar EUV radiation. Another potential process is ionization by impact of solar wind electrons, but, as shown by Bzowski et al. (2012b), its intensity outside 1 AU is on the order of the uncertainty of the total ionization rate. Thus, to calculate the survival probabilities of *IBEX* ENAs we adopt the total ionization rate as a sum of the charge-exchange and photoionization rates:

$$ \beta(t) = \beta_{\text{cx}}(t) + \beta_{\text{ph}}(t) \qquad (B2) $$

Equation (B.1) says that the survival probability of each atom depends on the history of its exposure to ionization processes during its travel. Therefore, the calculation of survival probability of an ENA requires solving the equation of motion.

The trajectories of *IBEX* H ENA are governed by the joint action of solar gravity and solar resonant radiation pressure from the solar Lyα photons. Since the inner heliosphere can be regarded as optically thin for solar photons, the flux of solar photons at all wavelengths decreases with the square of heliocentric distance, just as solar gravity force does. Thus, the solar radiation force is conveniently expressed as a ratio μ of the force of radiation pressure divided by solar gravity and the equation of motion takes the form:

$$ \frac{d^2\mathbf{r}}{dt^2} = -\frac{(1-\mu)GM}{r^2}\frac{\mathbf{r}}{r}, \qquad (B3) $$

where $\mathbf{r}(t)$ is the radius vector of the ENA at a time t, M is the solar mass, G is the gravitational constant, and $r = |\mathbf{r}|$ is heliocentric distance.

If the solar flux in the Lyα line could be regarded as invariant in time and independent of the wavelength, Equation (B3) would yield a purely Keplerian hyperbolic trajectory. In reality, however, none of these prerequisites is fulfilled. As measured by Lemaire et al. (2005), the spectral profile of the solar Lyα line is self-reversed, with a central trough and two horns (see the left-hand panel in Figure 33). Hence, due to the Doppler effect, the

radiation pressure force acting on a H ENA is a function of radial velocity v_r of this atom relative to the Sun: $\mu = \mu(v_r)$, where $v_r = (d\mathbf{r}/dt) \cdot (\mathbf{r}/r)$. In addition, the total flux in the solar Lyα line varies in time (see the right-hand panel in Figure 33), so the radiation pressure force is also a function of time: $\mu = \mu(t, v_r)$. Consequently, Equation (B3) must be solved numerically.

The complex dynamics is especially important in the case of lower-energy ENAs, i.e., those that travel at $\sim$150 km s^{-1} (115 eV for H) and less. Their radial velocities are always within the spectral range of the solar Lyα line and radiation pressure affects their trajectories at all times. On the other hand, the highest-energy ENAs are Doppler-shifted outside the spectral range of the solar Lyα line and during most of their travel they are only sensitive to solar gravity. Radiation pressure switches on for them only during their approach to the detector, which at *IBEX* is always near the perihelion. Even though the absolute velocities of these ENAs remain high, the radial component rapidly decreases, moving into the spectral range of the Lyα line. Nevertheless, such atoms move so fast that the Sun does not significantly modify their motions and their trajectories are close to straight lines.

The instantaneous ionization rate in Equation (B1) is in fact a function of both $\mathbf{r}(t)$ and t. Since the photoionization rate decreases with the square of heliocentric distance and is practically independent of heliolatitude (see Bzowski 2008 for a discussion of small deviations), it can be expressed as

$$ \beta_{\text{ph}} = \beta_{\text{ph}}(t)\left(\frac{r_E}{r(t)}\right)^2, \qquad (B4) $$

where $r_E = 1$ AU.

The charge-exchange rate is, however, a more complex function. It depends on the local density of solar wind ions, n_{p}, and on the magnitude of relative velocity v_{rel} between the ENA, traveling at a velocity $\mathbf{v}_{\text{ENA}} = d\mathbf{r}/dt$, and solar wind, radially expanding at $\mathbf{v}_{\text{sw}}$:

$$ v_{\text{rel}}(\mathbf{r}, t) = |\mathbf{v}_{\text{rel}}| = |\mathbf{v}_{\text{sw}}(\mathbf{r}, t) - \mathbf{v}_{\text{ENA}}(\mathbf{r})|, \qquad (B5) $$

where the magnitude of solar wind speed is a function of both time and heliolatitude. For ENAs in the supersonic solar wind (i.e., inside the termination shock) the local charge-exchange rate is then given by the formula:

$$ \beta_{\text{cx}}(\mathbf{r}, t) = n_p(\mathbf{r}, t) v_{\text{rel}}(\mathbf{r}, t) \sigma_{\text{cx}}(v_{\text{rel}}), \qquad (B6) $$

where σ_{cx} is the charge-exchange cross section (Lindsay & Stebbings 2005) for the collision speed $v_{\text{rel}} = |\mathbf{v}_{\text{sw}} - \mathbf{v}_{\text{ENA}}|$ and the density of solar wind protons is, similar to solar wind velocity, a function of time and heliolatitude and on average, unlike solar wind speed, quadratically decreases with heliocentric distance. Thus, the instantaneous charge-exchange rate is a fairly complex function of the solar wind conditions and of the trajectory of a given ENA. To a first approximation, however, it can be regarded as decreasing with the square of heliocentric distance because $n_{\text{p}} = n_{p,E}(\varphi, t)(r_E/r)^2$, where $n_{p,E}$ is the density at $r_E = 1$ AU and φ is heliolatitude. The quality of this approximation was shown by Bzowski et al. (2012b) to be valid to approximately 5%. A schematic illustration of the charge-exchange geometry is presented in Figure 34.

To calculate the survival probability of a single H ENA, one has to specify the time t_{stop} and location $\mathbf{r}_{\text{stop}}$ of the detection at *IBEX* and to select its velocity $\mathbf{v}_{\text{stop}}$ (magnitude and direction) as it approaches the detector. Both $\mathbf{r}_{\text{stop}}$ and $\mathbf{v}_{\text{stop}}$ must be taken
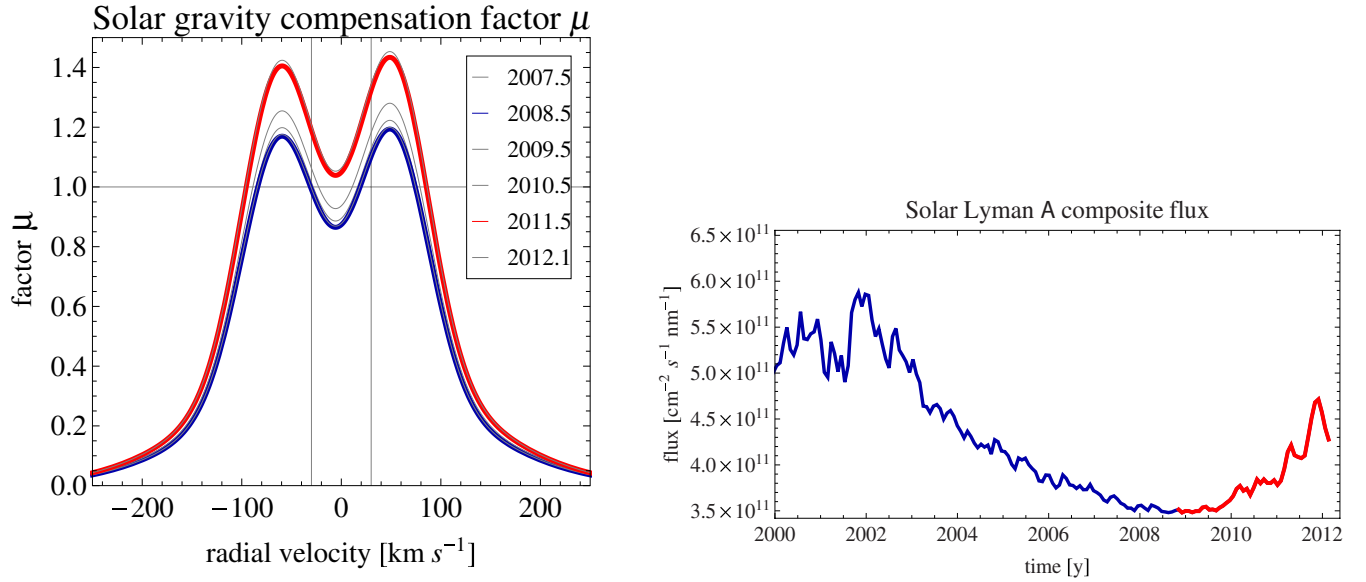
Figure 33. Solar gravity compensation factor μ shown as a function of the radial velocity v_r for selected epochs relevant for *IBEX* ENAs (left-hand panel) and Carrington period-averaged total flux in the solar Lyα line (right-hand panel). Red in the right-hand panel marks the time interval after *IBEX* launch. The horizontal line in the left-hand panel marks the level of perfect compensation of solar gravity by the resonance Lyα radiation pressure. The vertical bars mark ± 30 km s^{-1} of the Doppler shift.

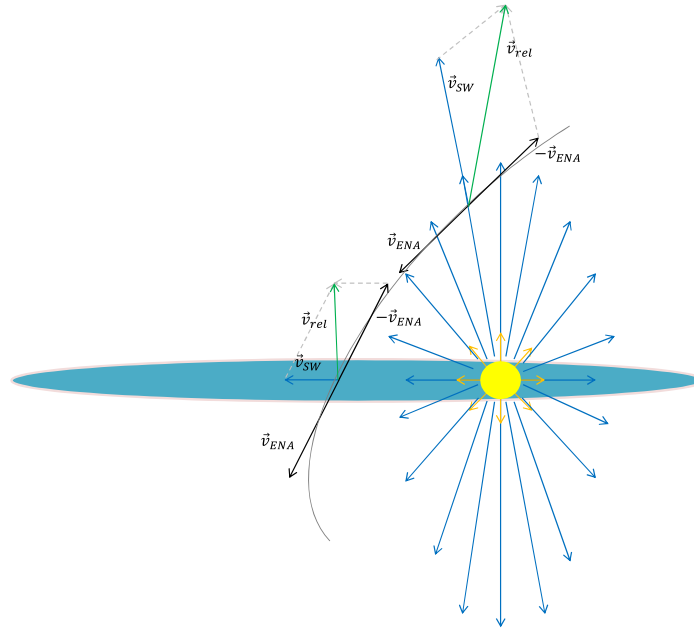(A color version of this figure is available in the online journal.)

Figure 34. Schematic diagram of the variation of relative velocity $\mathbf{v}_{\mathrm{rel}}$ between an ENA that is traveling at a velocity $\mathbf{v}_{\mathrm{ENA}}$ along the curved trajectory in the solar neighborhood, and the solar wind, whose radial expansion velocity $\mathbf{v}_{\mathrm{sw}}$ is a function of heliolatitude. The yellow circle is the Sun and the blue plane (seen almost edge-on) is the solar equator.

(A color version of this figure is available in the online journal.)

relative to the Sun. Then one must choose one of the following two schemes to calculate survival probabilities: either (1) the calculation is for the detection velocity $\mathbf{v}'_{\mathrm{stop}}$ in the *IBEX* inertial reference frame, which is defined by the instantaneous *IBEX* velocity relative to the Sun $\mathbf{v}_{\mathrm{IBEX}}(t_{\mathrm{stop}})$ or (2) in the solar-inertial reference frame. In the first of these two cases, $\mathbf{v}_{\mathrm{stop}} = \mathbf{v}'_{\mathrm{stop}} - \mathbf{v}_{\mathrm{IBEX}}(t_{\mathrm{stop}})$, in the second case $\mathbf{v}'_{\mathrm{stop}} = \mathbf{v}_{\mathrm{stop}}$. Here, we select option (2).

To calculate the survival probability, with the parameters $\mathbf{r}_{\mathrm{stop}}$, $\mathbf{v}_{\mathrm{stop}}$, t_{stop} selected, one solves the equation of motion (B3), simultaneously integrating the survival probability using

Equations (B1), (B2), and (B4)–(B6), as extensively discussed by Tarnopolski & Bzowski (2009, see also their Equation (3)). To carry out this calculation, one needs to know the evolution in time and heliolatitude of the solar wind speed and density as well as the evolution in time of the H photoionization rate and of the total flux of the solar Lyα radiation. The solution of the equation of motion is performed in the heliographic inertial reference system, proposed by Burlaga (1984) and modified by Fränz & Harper (2002) for the J2000 epoch (HCI).

The radiation pressure term μ in Equation (B3) is calculated using the model of the solar Lyα line profile defined in Equation

30

(5) in Tarnopolski & Bzowski (2009), with the numerical values of the parameters defined therein. Plots of the model profiles for the years since *IBEX* launch are presented in Figure 33. For the total Lyα flux, needed in Tarnopolski & Bzowski's model, we use the Carrington-period-averaged daily composite flux (Woods et al. 2000), as calculated by Bzowski et al. (2012b) and shown in the right-hand panel of Figure 33. The total Lyα flux is almost spherically symmetric. The small deviations from perfect symmetry (Auchère 2005; Pryor et al. 1992) are adopted from Bzowski (2008, see Equation (3) therein).

The solar wind parameter evolution was determined by Sokół et al. (2012) based on the OMNI-2 in-ecliptic solar wind data collection (King & Papitashvili 2005), *Ulysses* SWOOPS in situ measurements (Bame et al. 1992; McComas 2000; McComas et al. 2002, 2006, 2008) and interplanetary scintillation observations (Tokumaru et al. 2010). The in-ecliptic density and velocity of solar wind, obtained for 1 AU from the OMNI-2 collection as hourly averages and averaged by Carrington rotation period, are presented in Figure 35, with the interval after *IBEX* launch marked with a vertical line. It is worth noting that the solar wind flux in the ecliptic after *IBEX* launch was rather stable, but before that it featured a distinct drop that started in the first half of 1990s, which was also likely present at all heliolatitudes (McComas et al. 2008).

The yearly averages of the solar wind velocity and density heliolatitudinal profiles used in the construction of the model are shown in Figures 14 and 19, respectively, in Sokół et al. (2012). The heliolatitude versus time maps of interpolated solar wind speed and density actually used in the calculations are presented in Figure 20 in Sokół et al. (2012). The values from these maps, bilinearly interpolated in time and heliolatitude, are fed into Equations (B5) and (B6) to yield the local instantaneous charge-exchange rate $\beta_{cx}(\mathbf{r}, t)$. To better illustrate the evolution of the latitudinal structure of solar wind during the time interval of *IBEX* observations reported in this paper, in Figure 36 we replot the heliolatitude versus time contour map from the Sokół et al. (2012) model, cut precisely to the time intervals corresponding to *IBEX* Maps 1–6.

The photoionization rate of H ENAs at 1 AU is adopted from Bzowski et al. (2012b, see their Figure 2.9). Those authors obtained a Carrington period-averaged time series based on direct measurements of solar spectrum by TIMED/SEE (Woods et al. 2005) and a system of proxies detailed in their Equations (2.20)–(2.22). The proxies are based on well-defined and routinely measured quantities: the CELIAS/SEM double-channel EUV flux time series (Hovestadt et al. 1995; Judge et al. 1998), the $F_{10.7}$ solar radio flux (Covington 1969; Tapping 1987), and MgII$_{cw}$ index (Viereck & Puga 1999; Viereck et al. 2004).

The solar wind and solar EUV radiation parameters used in the calculations make a synchronized system based on actual measurements (Bzowski et al. 2012b). The system is based on a uniform time grid centered at halves of Carrington rotations and on a fixed grid of $10°$ heliolatitudinal bins. The parameters are normalized to 1 AU. All quantities used in this system are assumed to follow the $1/r^2$ dependence on heliocentric distance r except solar wind speed, which is assumed to be solar-distance-independent. The numerical tracking of the atoms is carried out until a given test atom exceeds a preselected limiting distance from the Sun, typically 90 AU. When this is accomplished, the exposure of the ENA to the ionizing factors, calculated from the integral under the exponent in Equation (B1), is registered and the survival probability w_{sur} for this given atom is obtained from Equation (B1).
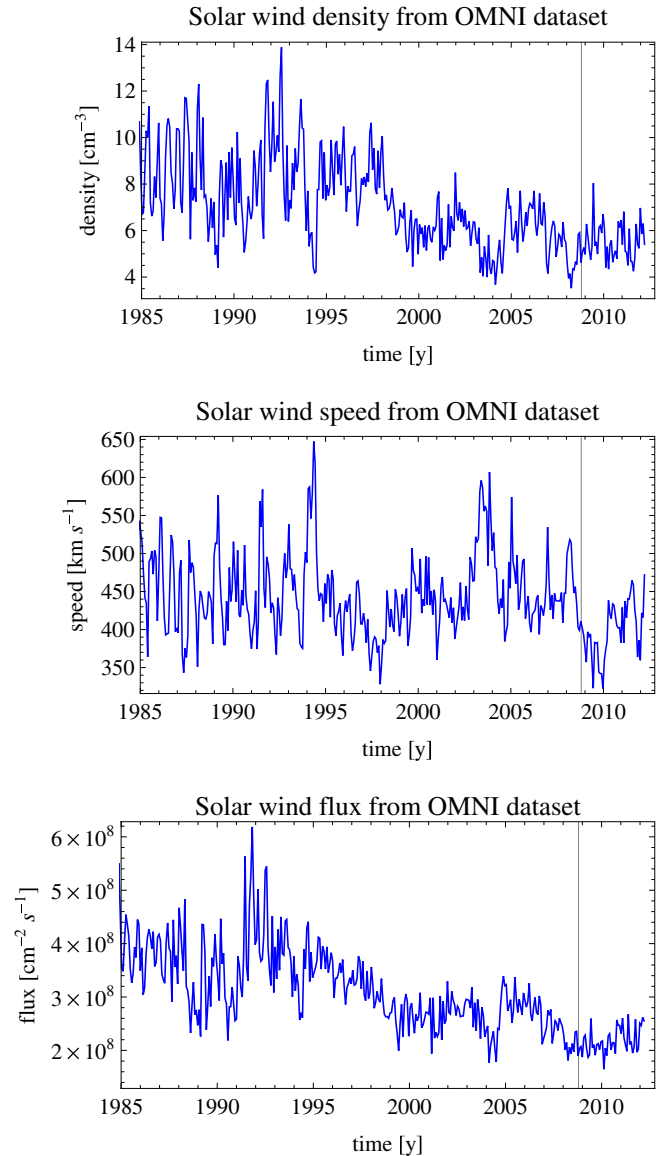

Figure 35. Carrington-period-averaged solar wind density (upper panel), speed (middle panel), and flux (lower panel), calculated based on the OMNI-2 hourly data collection (King & Papitashvili 2005). The density and flux are scaled to 1 AU by the square of heliocentric distance. The vertical bar marks the time of *IBEX* launch. The data stop at the end of *IBEX* Map 6.

(A color version of this figure is available in the online journal.)

B.2. Survival Probability for a Given Orbit and Energy

The baseline survival probability product is a series of survival probabilities of H ENAs observed at a given *IBEX* orbit at a selected energy as a function of spin angle. The calculation is performed for the middle of the observation time interval for a given *IBEX* orbit or orbital arc. We have verified that the small changes in the probabilities during the time interval corresponding to the orbit are almost linear in time and thus taking the middle point of the time interval is equivalent to averaging over time.

The calculation starts with the selection of the strip on the sky from which the ENAs come into the detector. The strip is defined by the pointing of the *IBEX* spin axis, which changes from orbit to orbit (and now per orbit arc), and by the field of view of the collimator.
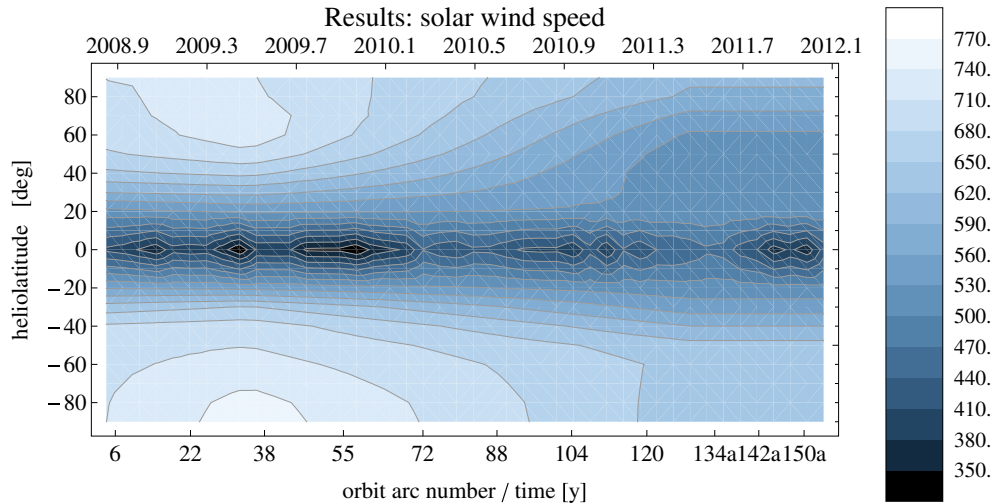
Figure 36. Solar wind speed as a function of time and heliolatitude for the time interval of *IBEX* observations, obtained from the model by Sokół et al. (2012). Note the north–south asymmetry in the speed structure, with the onset of the expansion of the slow wind region in the north hemisphere preceding the expansion in the south hemisphere. The equatorial band is composed of Carrington period averages of the OMNI-2 hourly solar wind speed, while latitudes outside the $\pm20°$ band are bilinearly interpolated between the yearly averaged solar wind speed profiles obtained from interplanetary scintillation observations. Also note that the structure after $\sim$2011.5 outside the equatorial band taken from the OMNI-2 collection is a simple extrapolation because the scintillation observations needed to extend the model into this time interval are still being collected. For details see Sokół et al. (2012).

(A color version of this figure is available in the online journal.)

The visibility strip defined for a given orbit is first covered with survival probabilities of individual ENAs calculated on a uniform grid (the HEALPix tessellation; Górski et al. 2005), which is defined in the heliographic reference system and for each orbit transformed into the *IBEX* coordinates (ψ, ϕ), where spin phase ψ runs along the visibility strip from 0 to 2π. The angle ϕ is in the perpendicular direction to the spin phase line and spans $(\pm\rho_{\mathrm{lim}})$, where ρ_{lim} is the outer radius of the collimator field of view equal to $\sim8°$. Then, a virtual collimator is stepped along this strip with the boresight sliding along the centerline. For each step along the visibility strip, the survival probabilities are integrated over the collimator field of view, multiplied with the transmission function of the collimator $T(\rho, \theta)$. This procedure returns an effective survival probability $w_{\mathrm{eff}}(t, E, \psi)$ for a given moment of time t, energy E, and spin phase ψ:

$$w_{\mathrm{eff}}(t, E, \psi) = \int_0^{2\pi\rho} \int_0^{\mathrm{lim}} w_{\mathrm{sur}}(t, E, \psi'(\psi, \rho, \theta),$$
$$\times\ \phi'(\psi, \rho, \theta))T(\rho, \theta)\sin\rho\, d\rho\, d\theta. \quad \text{(B7)}$$

The coordinates $\psi'(\psi, \rho, \theta)$, $\phi'(\psi, \rho, \theta)$, for which the integrand function w_{sur} is evaluated, are calculated separately for each value of spin phase ψ. Thus, the members of the set of individual survival probabilities w_{sur} pre-calculated for the visibility strip for each orbit can be used in the calculation of the effective survival probability for each given spin phase value ψ, which means they can be efficiently re-used for different values of ψ. An illustration of the visibility strip and an orientation of the collimator field of view is sketched in Figure 3 and the transmission function in Figure 2 in Bzowski et al. (2012a). The calibration of the transmission functions for the collimators of the *IBEX-Hi* and *IBEX-Lo* instruments were presented in Funsten et al. (2009b) and Fuselier et al. (2009b), respectively.

For this study, we scanned the visibility strips for each of the *IBEX* orbits and orbit arcs with a $1°$ cadence and calculated average probabilities for $6°$ bins in spin phase. In this way, the effective survival probabilities correspond to the *IBEX* $6°$ pixels available for each orbit and for each spin phase we have

a time series of the effective survival probabilities for the entire duration of *IBEX* observations.

The values of effective survival probabilities are sensitive to solar wind and solar EUV radiation conditions and in addition, they show some sensitivity to a number of second-order effects, including (1) the mean inclination of the visibility strip to the Earth–Sun line, (2) the distance and velocity of the Earth relative to the Sun, (3) the distance and velocity of the *IBEX* spacecraft relative to the Earth, and (4) Earth's heliolatitude. An illustration of the scale of these effects is best seen in a time series of effective survival probabilities for selected pixels. Such an illustration is presented in Figure 37, which shows time series of survival probabilities in the solar-inertial frame for two selected energies for the north and south ecliptic pole lines of sight (upper panel) and for the ecliptic ram and anti-ram lines of sight.

The magnitude of survival probabilities in the ecliptic plane changes very little on a multi-year timescale because during the *IBEX* operation such long-term changes were practically absent in the equatorial solar wind (cf. Figure 35). This is illustrated in the lower panel of Figure 37, where the survival probabilities vary on both monthly and yearly scales but do not show a clear trend. This is not the case for the polar lines of sight, which show a systematic decrease in time. This decrease, seen for all energies, is related to the change in the global solar wind structure, related to the increasing solar activity. The solar activity began to increase in the second half of 2009, which resulted in an expansion of the slow and variable equatorial solar wind to higher heliolatitudes. The expansion of the slow wind band was north–south asymmetric, being faster in the north hemisphere than in the south.

For ENAs approaching the detector from the direction of the ecliptic poles, the expansion of the slow wind band in heliolatitude results in increasing the portions of their trajectories immersed in the slow/variable wind, where the ionization rate is greater and consequently the survival probabilities of such atoms are lower. The change in the solar wind structure shown by Sokół et al. (2012) is visible in the ENA survival
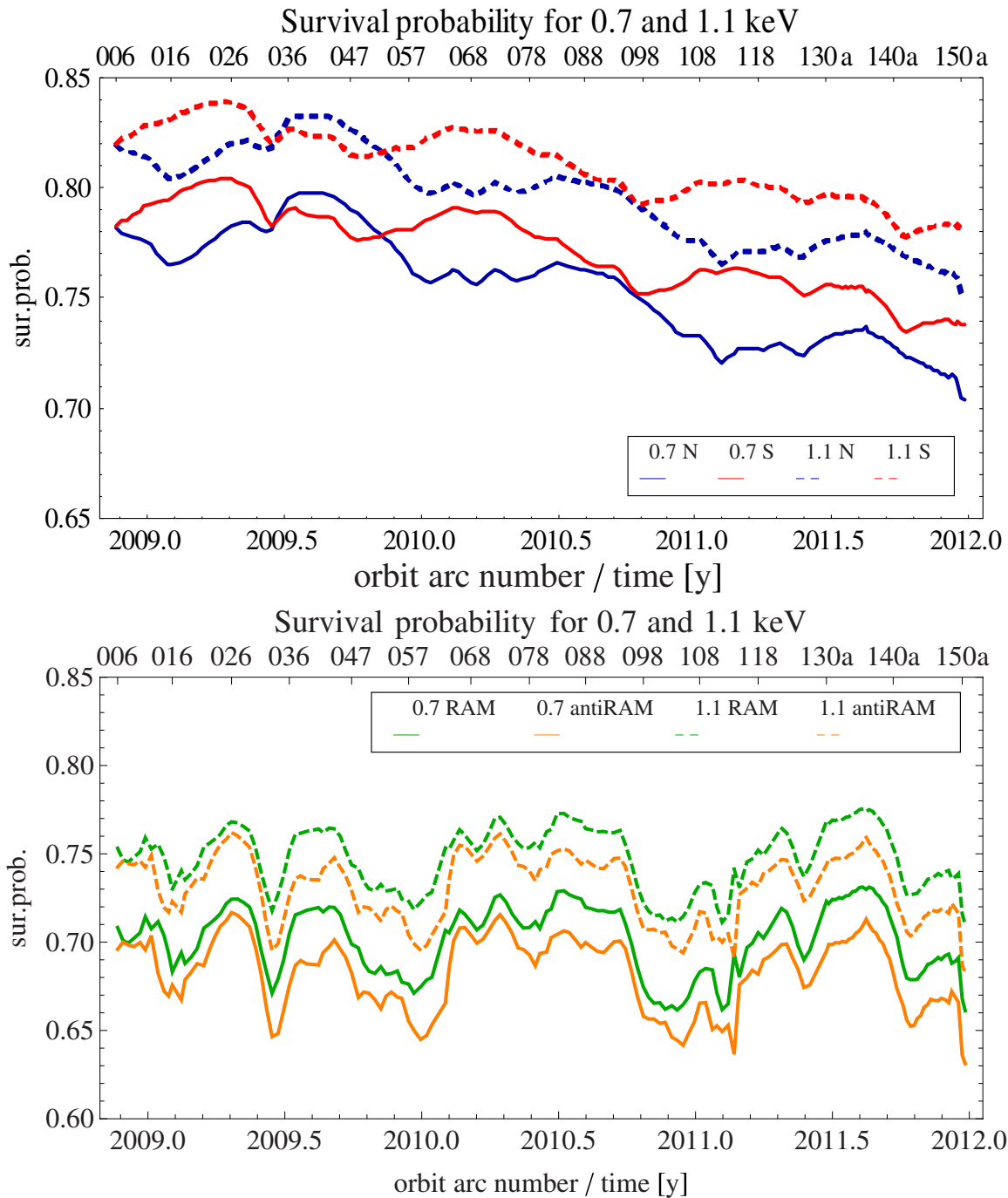
Survival probability for 0.7 and 1.1 keV

Survival probability for 0.7 and 1.1 keV

Figure 37. Effective survival probabilities for the north and south ecliptic pole pixels (upper panel) and the ram and anti-ram in-ecliptic pixels (lower panel) for two selected ENA energies in the solar-inertial frame: 0.7 keV and 1.1 keV, shown as a time series from the start of science operations until the end of Map 6.

(A color version of this figure is available in the online journal.)

probabilities almost immediately (i.e., almost without a time lag) because of the viewing geometry. The atoms cover the last few AU of their flight at trajectories inclined at almost right angle to the radius vector of the detector relative to the Sun, and thus most of the losses due to ionization occur within the last few weeks or months before the detection.

Since the heliographic latitude of the Earth varies periodically during the year (see Figure 38) and thus the thickness of the layer of enhanced ionization rate also varies in sync, the north and south time series of survival probabilities show a yearly anti-phase modulation. This effect exists for ENAs at all *IBEX*

energies; however, the magnitude of the modulation decreases with an increase in energy.

The survival probabilities in the pixels close to the ecliptic plane do not show the modulation due to the periodic changes in *IBEX*'s heliolatitude because the atoms observed near the ecliptic spend their whole time traveling close to the ecliptic plane, where the ionization rate is higher than in the polar regions. Hence, the values of survival probabilities in the ecliptic are lower, but almost do not systematically vary with time. On the other hand, the yearly modulation of the survival probabilities has an even slightly larger amplitude than that of
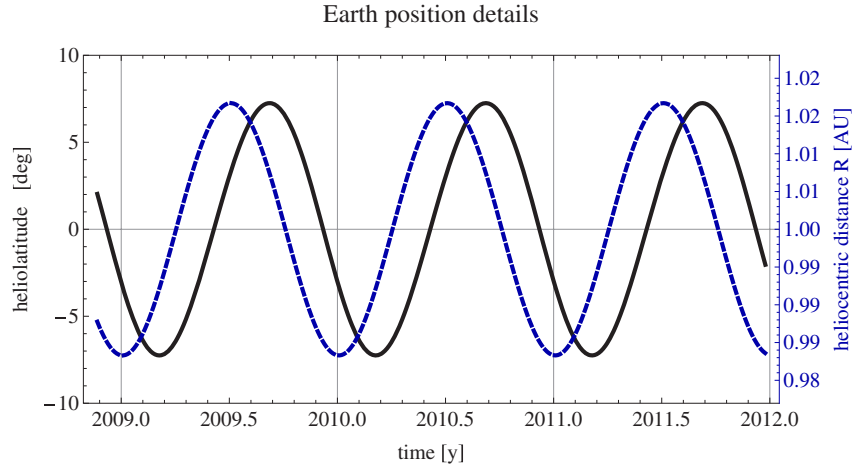
Earth position details

Figure 38. Yearly variations of Earth's (and *IBEX*'s) heliolatitude (black line, left-hand scale) and solar distance (blue line, right-hand scale) show only a small phase shift.

(A color version of this figure is available in the online journal.)

polar lines of sight. This modulation is due to the variations of the Earth distance from the Sun during the year (see Figure 38). This effect is similar in magnitude for the ram and anti-ram lines of sight. Of course, this also affects the polar lines of sight, but because of the small phase shift between the distance and heliolatitude it only seems to reduce the scale of the heliolatitude-related variation of the polar probabilities.

The survival probabilities presented in Figure 37 were calculated in the solar-inertial frame and thus, to a first approximation, one does not expect any ram versus anti-ram direction effects. However, inspection of the lower panel of Figure 37 shows that such an asymmetry does in fact exist. This is because the mean angle between the Earth–Sun line and the scan plane of *IBEX* is not exactly 90°. Due to this small deviation the atoms approaching the detector from the ram direction have not passed the perihelia of their orbits, while those approaching from the anti-ram direction have already passed them. This results in a small but noticeable difference between their survival probabilities. The magnitude of the differences decreases with the increase of ENA energy.

Additional short-scale "jitter" in the survival probabilities is caused by the monthly variation in the solar wind. Since the solar wind model used in the calculations has a resolution of one Carrington rotation close to the ecliptic plane, but only one year out of the ecliptic plane, the effect of the short-scale fluctuations of solar wind on the survival probabilities is most pronounced for the in-ecliptic pixels. On the other hand, during low solar activity solar wind at high ecliptic latitudes is generally much less variable than in the equatorial band, so less "jitter" in survival probabilities for high-latitude ENAs during a low solar activity interval should be expected.

B.3. Survival Probability Maps

To examine systematic effects and the evolution of survival probabilities with time, we first average the probabilities over the time intervals corresponding to the times of acquisition of *IBEX* yearly maps (the "ram" and "anti-ram" maps). By doing so we eliminate all effects related to the Earth's motion around the Sun and to Earth's travel in heliolatitude and are better able to study the time variation of global effective survival probability spectra.

The survival probabilities increase with the increasing H ENA energy in the solar inertial frame, as illustrated in Figure 39, which presents spectra of the effective survival probabilities
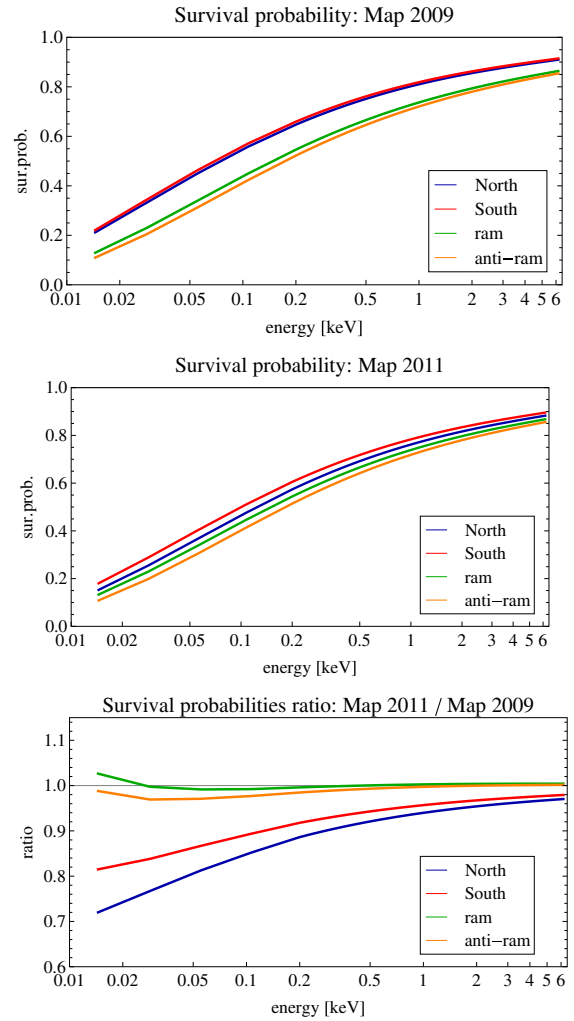

Figure 39. Spectra of effective survival probabilities of H ENAs for the north and south ecliptic pole pixels and for the ram and anti-ram pixels in the ecliptic plane, calculated in the solar-inertial frame and averaged over the time interval corresponding to *IBEX* Map 2009 (upper panel) and 2011 (middle panel). The lower panel presents a relative change in the spectra (the ratios of the corresponding spectra from 2011 to the spectra from 2009).

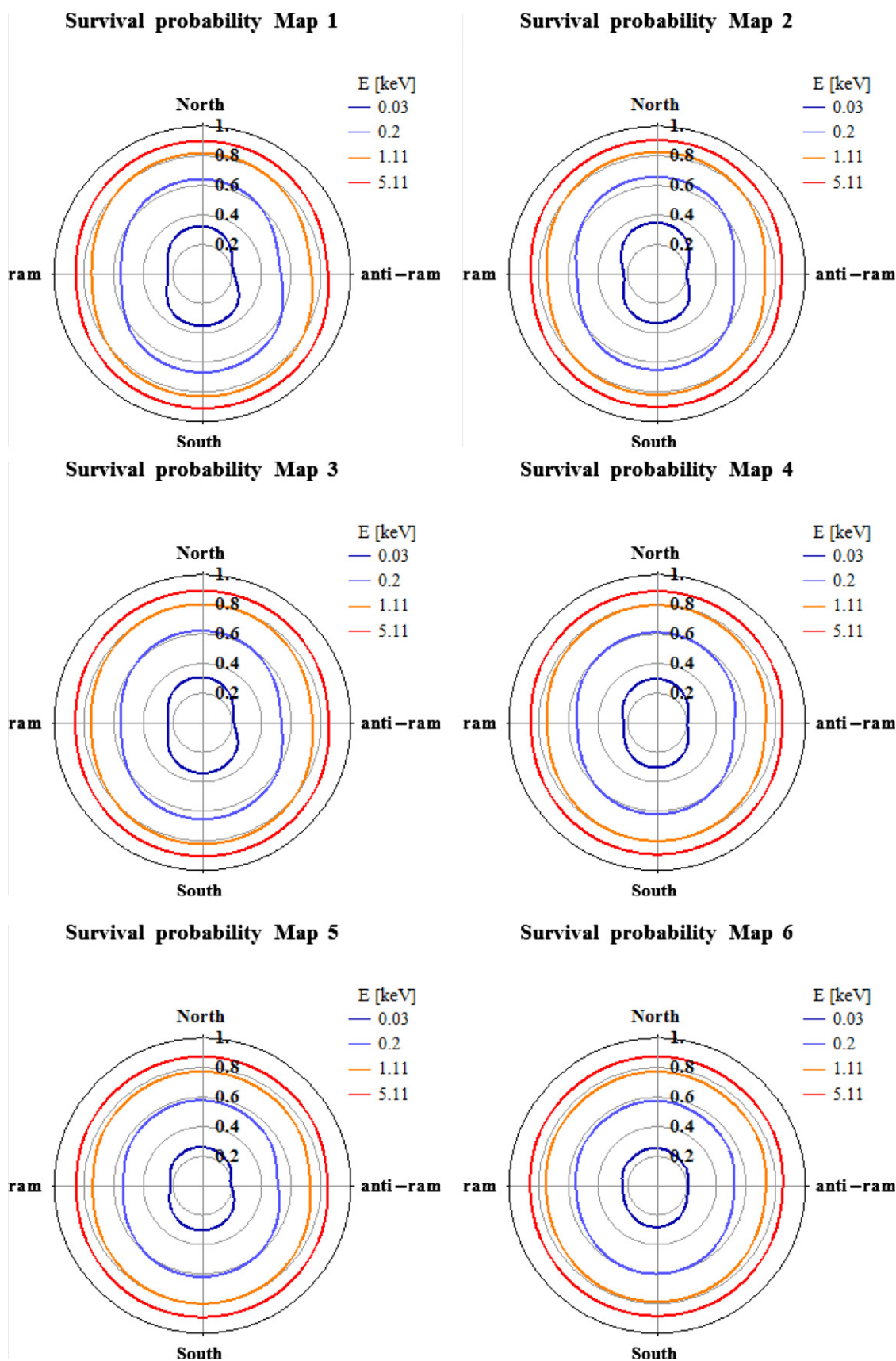(A color version of this figure is available in the online journal.)

Figure 40. Polar plots of the effective survival probabilities of H ENA, calculated in the solar-inertial frame for the whole range of the *IBEX* spin phase for selected H ENA energies, averaged over the time interval of *IBEX* Maps 1–6 for each spin phase. The magnitude of probability is indicated at the vertical axes of the plots. Spin phase increases counterclockwise from 0 at the north pole through 90° in the in-ecliptic ram direction, south pole at 180° and anti-ram at 270°. Note the symmetry between the odd and even maps.

(A color version of this figure is available in the online journal.)

of H ENA for the lines of sight toward the north and south ecliptic poles and in the ram and anti-ram directions for the time interval of *IBEX* Maps 2009 and 2011, as well as the ratios of these spectra.

The ecliptic spectra vary very little with time, which is understandable given their weak dependence on radiation pressure and the relatively small change in the overall ionization rate in the equatorial band of heliolatitudes. The differences between the 2009 and 2011 polar spectra are much more pronounced. They are related to the expansion of the slow wind region into higher heliolatitudes, which is somewhat asymmetric, with the north hemisphere preceding south.

Survival probabilities show some small but noticeable systematic differences between the odd- and even-numbered half-year maps. Plots of the effective survival probabilities averaged over the time intervals of *IBEX* Maps 1–6 are shown in Figure 40. These differences are related to the orientation of the spacecraft relative to the solar equator plane. Generally, *IBEX* is below the solar equator plane during the first half of each year (cf. Figure 38) and above it during the second half. This, together with the north–south asymmetry of solar wind, results in some small systematic differences between the effective survival probabilities.

To correct the *IBEX*-inertial maps of H ENA flux for survival probabilities, we start from survival probabilities calculated on a grid of energies and spin angles in the solar-inertial frame separately for each orbit, as detailed in the preceding section. These probabilities are applied to the calculated fluxes during the construction of the full sky ENA flux images.

As part of the standard processing of the *IBEX* data, fluxes are first calculated for each orbit as a function of angle and energy step in the spacecraft frame. A mapping procedure considers each angular element from each energy step and orbit separately for placement on the full sky maps. The fluxes from each element are then transformed into the solar-inertial frame. This transform results in a shift in the apparent ENA energy and a slight change in the apparent direction. Next, we interpolate the appropriate survival probability for the element using the survival probability grid (in energy and direction) for the orbit being considered. This is a two-dimensional interpolation that is linear in spin angle and logarithmic in energy. The flux in the element is finally corrected for this probability and placed on the map via the standard algorithms.

REFERENCES

Allegrini, F., Bzowski, M., Dayeh, M. A., et al. 2012, ApJ, 749, L41
Allegrini, F., Crew, G. B., Demkee, D., et al. 2009, Space Sci. Rev., 146, 105
Auchère, F. 2005, ApJ, 622, 737
Bame, S. J., McComas, D. J., Barraclough, B. L., et al. 1992, A&AS, 92, 237
Burlaga, L. F. 1984, Space Sci. Rev., 39, 255
Bzowski, M. 2008, A&A, 488, 1057
Bzowski, M., Kubiak, M. A., Möbius, E., et al. 2012a, ApJS, 198, 12
Bzowski, M., Sokół, J. M., Tokumaru, M., et al. 2012b, in Cross-Calibration of Past and Present Far UV Spectra of Solar Objects and the Heliosphere, Solar Parameters for Modeling Interplanetary Background, ed. R. M. Bonnet, E. Quémerais, & M. Snow (ISSI Scientific Report No. 12; Springer), chap. 2, in press (arXiv:1112.2967)
Bzowski, M., & Tarnopolski, S. 2006, in Proc. Fifth Annu. IGPP Astrophys. Conf., Physics of the Inner Heliosheath: Voyager Observations, Theory, and Future Prospects, ed. J. Heerikhuisen, V. Florinski, G. P. Zank, & N. V. Pogorelov (AIP CP-858; Melville, NY: AIP), 251
Chalov, S. V., Alexashov, D. B., McComas, D., et al. 2010, ApJ, 716, L99
Collier, M. R., Moore, T. E., Simpson, D., et al. 2004, Adv. Space Res., 34, 166
Covington, A. E. 1969, J. R. Soc. Canada, 63, 125
Dayeh, M. A., McComas, D. J., Allegrini, F., et al. 2012, ApJ, 749, 50
Fahr, H.-J., Siewert, M., McComas, D. J., & Schwadron, N. A. 2011, A&A, 531, 77

Florinski, V., Zank, G. P., Heerikhuisen, J., Hu, Q., & Khazanov, I. 2010, ApJ, 719, 1097
Fränz, M., & Harper, D. 2002, Planet. Space Sci., 50, 217
Funsten, H. O., Allegrini, F., Bochsler, P., et al. 2009a, Space Sci. Rev., 146, 75
Funsten, H. O., Allegrini, F., Crew, G. B., et al. 2009b, Science, 326, 964
Funsten, H. O., Harper, R. W., & McComas, D. J. 2005, Rev. Sci. Instrum., 76, 053301
Fuselier, S. A., Allegrini, F., Bzowski, M., et al. 2012, ApJ, 754, 14
Fuselier, S. A., Allegrini, F., Funsten, H. O., et al. 2009a, Science, 326, 962
Fuselier, S. A., Bochsler, P., Chornay, D., et al. 2009b, Space Sci. Rev., 146, 117
Fuselier, S. A., Ghielmetti, A. G., & Wurz, P. 2009c, ApJ, 698, 1117
Gamayunov, K., Zhang, M., & Rassoul, H. 2010, ApJ, 725, 2251
Górski, K. M., Hivon, E., Banday, A. J., et al. 2005, ApJ, 622, 759
Grzedzielski, S., Bzowski, M., Czechowski, A., et al. 2010, ApJ, 715, L84
Heerikhuisen, J., Pogorelov, N. V., Zank, G. P., et al. 2010, ApJ, 708, L126
Hovestadt, D., Hilchenbach, M., Burgi, A., et al. 1995, Sol. Phys., 162, 441
Judge, D. L., McMullin, D. R., Ogawa, H. S., et al. 1998, Sol. Phys., 177, 161
King, J. H., & Papitashvili, N. E. 2005, J. Geophys. Res., 110, A02104
Krimigis, S. M., Mitchell, D. G., Roelof, E. C., Hsieh, K. C., & McComas, D. J. 2009, Science, 326, 971
Lemaire, P., Emerich, C., Vial, J.-C., et al. 2005, Adv. Space Res., 35, 384
Lindsay, B. G., & Stebbings, R. F. 2005, J. Geophys. Res., 110, A12213
Livadiotis, G., & McComas, D. J. 2009, J. Geophys. Res., 114, A11105
Livadiotis, G., & McComas, D. J. 2010, ApJ, 714, 971
McComas, D. J., Alexashov, D., Bzowski, M., et al. 2012, Science, 336, 1291
McComas, D. J., Allegrini, F., Bochsler, P., et al. 2009a, Space Sci. Rev., 146, 11
McComas, D. J., Allegrini, F., Bochsler, P., et al. 2009b, Science, 326, 959
McComas, D. J., Allegrini, F., Pollock, C. J., et al. 2004, Rev. Sci. Instrum., 75, 4863
McComas, D. J., Bame, S. J., Barraclough, B. L., et al. 1998, Geophys. Res. Lett., 25, 1
McComas, D. J., Barraclough, B. L., Funsten, H. O., et al. 2000, J. Geophys. Res., 105, A5, 10419
McComas, D. J., Bzowski, M., Frisch, P., et al. 2010, J. Geophys. Res., 115, A09113
McComas, D. J., Carrico, J. P., Hautamaki, B., et al. 2011a, Space Weather, 9, S11002
McComas, D. J., Ebert, R. W., Elliott, H. A., et al. 2008, Geophys. Res. Lett., 35, L18103
McComas, D. J., Elliot, H. A., Gosling, J. T., & Skoug, R. M. 2006, Geophys. Res. Lett., 33, L09102
McComas, D. J., Elliot, H. A., Gosling, J. T., et al. 2002, Geophys. Res. Lett., 29, 1290
McComas, D. J., Elliott, H. A., Schwadron, N. A., et al. 2003, Geophys. Res. Lett., 30, 1517
McComas, D. J., Funsten, H. O., Fuselier, S. A., et al. 2011b, Geophys. Res. Lett., 38, L18101
Möbius, E., Bochsler, P., Bzowski, M., et al. 2009, Science, 326, 969
Möbius, E., Bochsler, P., Bzowski, M., et al. 2012, ApJS, 198, 11
Moore, T. E., Chornay, D. J., Collier, M. R., et al. 2000, Space Sci. Rev., 91, 155
Pryor, W. R., Ajello, J. M., Barth, C. A., et al. 1992, ApJ, 394, 363
Reisenfeld, D. B., Allegrini, F., Bzowski, M., et al. 2012, ApJ, 747, 110
Saul, L., Wurz, P., Rodriguez, D., et al. 2012, ApJS, 198, 14
Schwadron, N. A., Beccari, G., De Marchi, G., et al. 2011, ApJ, 731, 1
Schwadron, N. A., Bzowski, M., Crew, G. B., et al. 2009, Science, 326, 966
Siewert, M., Fahr, H.-J., McComas, D. J., Schwadron, N. A., et al. 2012, A&A, 539, A75
Sokół, J. M., Bzowski, M., Tokumaru, M., et al. 2012, Sol. Phys.,
Spence, H. E., Case, A. W., Golightly, M. J., et al. 2010, Space Sci. Rev., 150, 243
Tapping, K. F. 1987, J. Geophys. Res., 92, 829
Tarnopolski, S., & Bzowski, M. 2009, A&A, 493, 207
Tokumaru, M., Kojima, M., & Fujiki, K. 2010, J. Geophys. Res., 115, A04102
Viereck, R., & Puga, L. C. 1999, J. Geophys. Res., 104, 9995
Viereck, R. A., Floyd, L. E., Crane, P. C., et al. 2004, Space Weather, 2, S10005
Woods, T. N., Eparvier, F. G., Bailey, S. M., et al. 2005, J. Geophys. Res., 110, A01312
Woods, T. N., Tobiska, W. K., Rottman, G. J., & Worden, J. R. 2000, J. Geophys. Res., 105, 27195
Wurz, P., Collier, M. R., Moore, T. E., et al. 2004, in AIP Conf. Proc. 719, Physics of the Outer Heliosphere, ed. V. Florinski, N. V. Pogorelov, & G. P. Zank (Melville, NY: AIP), 195
Wurz, P., Fuselier, S. A., Möbius, E., et al. 2009, Space Sci. Rev., 146, 173